Titre: Title:	Evaluating Flow-Added Damping via Linear Stability Analysis
Auteur: Author:	Clément Tony Pierre Audefroy
Date:	2024
Type:	Mémoire ou thèse / Dissertation or Thesis
Référence: Citation:	Audefroy, C. T. P. (2024). Evaluating Flow-Added Damping via Linear Stability Analysis [Mémoire de maîtrise, Polytechnique Montréal]. PolyPublie. https://publications.polymtl.ca/59176/

URL de PolyPublie: PolyPublie URL:	https://publications.polymtl.ca/59176/
Directeurs de recherche: Advisors:	Frederick Gosselin, Sébastien Houde, & Mathieu Olivier
Programme: Program:	Génie mécanique

POLYTECHNIQUE MONTRÉAL
affiliée à l'Université de Montréal

Evaluating Flow-Added Damping via Linear Stability Analysis

CLÉMENT TONY PIERRE AUDEFROY
Département de génie mécanique

Mémoire présenté en vue de l'obtention du diplôme de *Maîtrise ès sciences appliquées*
Génie mécanique

Juillet 2024

POLYTECHNIQUE MONTRÉAL
affiliée à l'Université de Montréal

Ce mémoire intitulé :

Evaluating Flow-Added Damping via Linear Stability Analysis

présenté par **Clément Tony Pierre AUDEFROY**
en vue de l'obtention du diplôme de *Maîtrise ès sciences appliquées*
a été dûment accepté par le jury d'examen constitué de :

Bruno BLAIS, président
Frédérick GOSSELIN, membre et directeur de recherche
Sébastien HOUDE, membre et codirecteur de recherche
Mathieu OLIVIER, membre et codirecteur de recherche
Stéphane ÉTIENNE, membre

DEDICATION

À mes acolytes du midi,
Florent, Matthias et Thibaut…

ACKNOWLEDGEMENTS

I would like to express my deepest gratitude to my supervisor, Frédérick, for his unwavering support and guidance throughout my project. His scientific expertise, insightful feedback, and encouragement have been invaluable in shaping this project. Frédérick's dedication and commitment to my academic growth have inspired me to strive for excellence. I am truly grateful for his mentorship and for the opportunities he provided me to learn and develop as a researcher. Thank you, Frédérick, for your patience, encouragement, and for believing in my potential.

I would like to thank my co-supervisor, Sébastien, for his experience and knowledge in hydraulic turbines and fluid mechanics. His guidance and support were crucial to the completion of my research. I am grateful for his insightful feedback and dedication throughout this project. Observing the work conducted in his lab at Laval University was truly inspiring.

I would like to express my gratitude to Mathieu for his exceptional guidance and expertise on numerical methods applied to fluid mechanics. His insights and support were pivotal to the advancement of my research. I am thankful for his valuable contributions and encouragement throughout this project.

I would like to express my gratitude to Danick, who helped me become familiar with the project he developed at the beginning of my master's program. I also wish to thank Alexandre Couture, whose work greatly inspired my thesis.

I sincerely acknowledge the financial support provided by the Institut de l'énergie Trottier and the industrial partners of the Tr-FRANCIS project. Participating in the Tr-FRANCIS project was an incredible opportunity that brought me closer to industrial research and exposed me to highly inspiring work.

I would also like to extend my acknowledgments to the LM2 research group for their support and collaboration throughout my research.

RÉSUMÉ

Les concepteurs de turbines hydraulique ont besoin de connaître le coefficient d'amortissement d'une pale de turbine pour évaluer sa durabilité sous des charges cycliques. Dans le cas des turbines hydrauliques, l'amortissement ajouté par l'écoulement est dominant. L'évaluation numérique de cet amortissement ajouté par l'écoulement est difficile avec les méthodes actuelles, qui impliquent des simulations complexes et coûteuses en termes de calcul, nécessitant des maillages mobiles comme les simulations d'interaction fluide-structure à couplage unidirectionnel ou bidirectionnel. Nous présentons une nouvelle approche efficace et rapide pour évaluer le coefficient d'amortissement ajouté en utilisant plusieurs modules de NASTRAN. En utilisant les fréquences naturelles dans le vide et dans un fluide au repos, une matrice de proportionnalité est intégrée dans la solution de flottement de NASTRAN via le facteur AVMI (Added Virtual Mass Incremental), garantissant ainsi l'évaluation de l'amortissement ajouté par l'écoulement. La validité de la méthodologie est confirmée par des comparaisons avec des données expérimentales et numériques issues de la littérature, montrant une forte concordance avec les résultats existants. Ces cas tests concernent des hydrofoils droits de différents profils géométriques, matériaux et conditions aux limites. La validité de la méthode est également démontrée pour une cascade d'hydrofoils. Cependant, cette méthode ne peut pas être utilisée pour des géométries plus complexes. Par conséquent, nous introduisons une autre approche rapide pour évaluer l'amortissement ajouté par l'écoulement, basée sur une formulation par éléments finis utilisant le solveur FreeFEM++. Cette méthode sera alors pertinente pour toute géométrie. Elle utilise un modèle hybride pour le champ d'écoulement. L'écoulement de base est un fluide parfait, tandis que l'écoulement de petites perturbations incorpore des effets visqueux. Cette approche simplifie le traitement des conditions aux limites et fait apparaître un terme déstabilisant dans la continuité de la vitesse à l'interface fluide-structure, en raison de la condition de glissement parfait à l'interface pour l'écoulement de base. La prise en compte des effets visqueux dans l'écoulement perturbé est cruciale pour capturer la circulation fluctuante autour de la plaque et dans le sillage, ce qui impacte significativement la stabilité du système et l'amortissement ajouté par l'écoulement. La formulation faible du problème est implémentée dans le solveur et l'amortissement ajouté par l'écoulement est évalué par une analyse de stabilité linéaire. La méthode est rapide à mettre en place car le maillage est fixe. Le temps de calcul est de quelques minutes comparé à plusieurs heures pour les méthodes existantes. La validité de cette méthode est confirmée par des comparaisons avec des données numériques de la littérature pour une plaque avec différentes conditions aux limites. Cette méthode nous permettra finalement de considérer

des géométries complexes, afin de se rapprocher d'une conception réaliste de turbine. Notre objectif ultime est d'utiliser une solution d'écoulement CFD existante sur une aube directrice ou une pale de rotor et de réaliser l'analyse de stabilité linéaire à partir de celle-ci, pour évaluer l'amortissement ajouté par l'écoulement.

ABSTRACT

Hydroelectric turbine designers require knowledge of the damping coefficient of a turbine blade to assess its durability under cyclic loading. In the case of hydraulic turbine, the flow-added damping is dominant. Numerical evaluation of the flow added damping is challenging with current methods that involve complex and computationally expensive simulations that require moving meshes like one-way or two-way coupling fluid structure interaction simulations. We introduce a new, efficient, and fast approach for assessing the added damping coefficient of a cascade of straight hydrofoils using NASTRAN's multiple modules. By using the vacuum and resting fluid natural frequencies, a proportionality matrix is incorporated into NASTRAN's flutter solution through the Added Virtual Mass Incremental factor (AVMI), ensuring the evaluation of the flow-added damping. The methodology's validity is confirmed through comparisons with experimental and numerical data from previously published articles, demonstrating strong agreement with existing results. Those test cases are straight hydrofoils of different geometry profiles, materials and boundary conditions. The validity of the method is also shown for a cascade of hydrofoils. However, this method cannot be used for more complex geometries. Therefore, we introduce another fast approach for assessing the flow-added damping, based on a finite element formulation using the FreeFEM ++ solver. This method will then be relevant for any geometry. This method uses a hybrid model for the flow field. The base flow is inviscid, while the small perturbation flow incorporates viscous effects. This approach simplifies the treatment of boundary conditions and recovers a destabilizing term in the velocity continuity at the fluid-structure interface, because of the free-slip boundary condition at the interface for the base flow. Accounting for viscous effects in the perturbation flow is crucial for capturing the fluctuating circulation around the plate and in the wake, which significantly impact the system's stability and the flow-added damping. The weak formulation of the problem is implemented in the solver and the flow-added damping is evaluated through linear stability analysis. The method is quick to setup as the mesh is fixed. The computation time is a few minutes compared to several hours for existing methods. The validity of this method is confirmed through comparisons with numerical data from the literature for a cantilever plate with different boundary conditions. This method will eventually allow us to consider complex geometries, to get closer to a realistic turbine design. Our ultimate objective is to use an existing CFD flow solution on a guide vane or a runner blade and perform the linear stability analysis about it.

TABLE OF CONTENTS

LIST OF TABLES

LIST OF FIGURES

LIST OF SYMBOLS AND ACRONYMS

List of acronyms:

AVMI	Added Virtual Mass Incremental
CFD	Computational Fluid Dynamics
FSI	Fluid-Structure Interaction
VIV	Vortex-Induced Vibrations
RANS	Reynolds-Averaged Navier–Stokes
URANS	Unsteady Reynolds-Averaged Navier–Stokes
FFT	Fast Fourier Transform
ROM	Reduced Order Models
CPU	Central Processing Unit
ALE	Arbitrary Lagrangian-Eulerian
MAC	Modal Assurance Criterion

List of symbols:

$[M_s]$	Structural mass matrix
$[C_s]$	Structural damping matrix
$[K_s]$	Structural stiffness matrix
$[M_f]$	Added mass matrix
$[C_f]$	Added damping matrix
$[K_f]$	Added stiffness matrix
$\boldsymbol{u_s}$	Displacement field
$\boldsymbol{F}$	External load
$\tilde{\boldsymbol{F}}$	Excitation force
ω	Complex eigenvalue
$\boldsymbol{\phi_i}$	Eigenvector
$[\Phi]$	Modal basis matrix
$\boldsymbol{u_h}$	Modal coordinates
$[M_{hh,s}]$	Structural modal mass matrix
$[C_{hh,s}]$	Structural modal damping matrix
$[K_{hh,s}]$	Structural modal stiffness matrix
$[M_{hh,f}]$	Added mass modal matrix
$[C_{hh,f}]$	Added damping modal matrix

$[K_{hh,f}]$	Added stiffness modal matrix
ζ	Damping ratio
f	Natural frequency
ρ_f	Fluid density
c	Reference length
k	Reduced frequency
U	Fluid velocity
$[Q_{hh}]$	Modal aerodynamic influence matrix
ω_{vac}	Angular frequency in vacuum
ω_f	Angular frequency in resting fluid
β	AVMI factor
$[P]$	Passage matrix of the AVMI factors
$\boldsymbol{W}$	Solid displacement vector
ρ_s	Solid density
$\boldsymbol{\sigma(W)}$	Cauchy stress tensor
Ω_s	Solid domain
$\boldsymbol{U_f}$	Fluid velocity vector
P	Pressure
$\boldsymbol{\tau(U_f)}$	Viscosity tensor
$\boldsymbol{\sigma_f(u_f, p)}$	Fluid stress tensor
η	Viscosity
Ω_f	Fluid domain
$\boldsymbol{w_b}$	Base solid displacement vector
$\boldsymbol{w}$	Perturbation solid displacement vector
p_b	Base pressure
p	Perturbation pressure
$\boldsymbol{u_{f,b}}$	Base flow velocity vector
$\boldsymbol{u_f}$	Perturbation flow velocity vector
λ	First Lamé coefficient
μ	Second Lamé coefficient
$\boldsymbol{\epsilon(w)}$	Infinitesimal strain tensor
E	Young's modulus
ν_s	Poisson coefficient
ϕ_b	Velocity potential
U_x	Horizontal component of the base flow velocity
U_y	Vertical component of the base flow velocity

$\hat{\boldsymbol{w}}$	Waveform of the solid displacement
$\hat{\boldsymbol{u}}_{\boldsymbol{f}}$	Waveform of the flow velocity
$\hat{p}$	Waveform of the pressure
Γ_{fs}	Fluid-structure interface
$\boldsymbol{u}_{\boldsymbol{s}}$	Perturbation solid displacement velocity
$\mathcal{V}_f$	Sobolev Space for the velocity potential
$\mathcal{U}_s$	Sobolev Space for the solid displacement and velocity
$\mathcal{U}_f$	Sobolev Space for the flow velocity
$\mathcal{P}_f$	Sobolev Space for the pressure
$\mathcal{L}_f$	Sobolev Space for the kinematic boundary condition
$\boldsymbol{\lambda}_{\boldsymbol{f}}$	Lagrangian Multiplier for the kinematic boundary condition
$\boldsymbol{n}_{\boldsymbol{f}}$	Normal vector defined in the fluid domain
$\boldsymbol{n}_{\boldsymbol{s}}$	Normal vector defined in the solid domain
$\tilde{\boldsymbol{u}}_{\boldsymbol{f}}$	Discretized fluid velocity
$\tilde{\boldsymbol{w}}$	Discretized solid displacement
$\tilde{p}$	Discretized pressure
$\tilde{\boldsymbol{u}}_{\boldsymbol{s}}$	Discretized solid displacement velocity
$\tilde{\boldsymbol{\lambda}}_{\boldsymbol{f}}$	Discretized Lagrangian multiplier
L	Length of the plate
h_p	Thickness of the plate
h	Channel semi-height
Re	Reynolds number
U_R	Reduced velocity
μ	Mass ratio
c	Geometric ratio
$\bar{\omega}$	Dimensionless complex eigenvalue
V_z	Vorticity
U_{cr}	Critical reduced velocity

CHAPTER 1 INTRODUCTION

Electricity demand varies considerably throughout the day. It presents two peaks, one in the morning when people wake up and the second one in the evening when people are back from work (Pitra and Musti, 2021). Those variations of the electricity demand put stresses on the electricity suppliers. Indeed, the electricity production must match the electricity demand at all time. Electricity production therefore varies throughout the day. In Quebec, 94 % of electricity production came from hydraulic turbines in 2019 (Government of Canada, 2023). The integration of other renewable sources of energy like wind turbines or solar power also add stresses to the electricity grid, because those two sources of energy are intermittent. The integration of those sources of energy coupled with the variations of electricity demand throughout the day have a significant impact on the number of starts and stops hydraulic turbines have to undergo to regulate the grid. Those phases of exploitation are the ones putting the most strain on the fatigue life of turbine components.

For hydro-power operators, the challenge is maintaining turbines operational for as long as possible, to reduce down time, because it represents significant financial and energy losses (Kumar and Saini, 2022). The increasing frequency of start and stop operations necessitates to compute the fatigue loading of the hydraulic turbines, to determine whether the device will last long enough. Rotor-stator interaction is identified as the primary factor contributing to early cracks in hydraulic turbines, as discussed by Coutu et al. (2012). In order to assess the vibration response for fatigue loading calculations, damping becomes a critical factor.

In the context of hydraulic turbines, structural damping is negligible compared to flow-added damping. The flow-added damping corresponds to the exchange of energy between the fluid and the structure and the larger the flow-added damping, the more the fluid attenuates the vibrations of the structure. To be able to assess accurately the vibration amplitude of the device to compute the fatigue life estimation, both the rotor-stator interaction and the flow-added damping needs to be studied.

Nowadays, the evaluation of flow-added damping relies mainly on empirical guidelines based on existing designs. There are a few existing numerical methods, primarily based on Computational Fluid Dynamics (CFD) with one-way or two-way coupled Fluid-Structure Interaction (FSI) methods, but they require important setup time, notably to program moving meshes and are computationally expensive (Monette et al., 2014; Gauthier et al., 2017; Liaghat et al., 2014). These methods can require up up to several days of computation time making it challenging to simulate a broad range of designs and test various parameters. As a consequence, new designs tend to closely resemble existing ones. Having a quick and precise method would open the door to unconventional designs by enabling the testing of numerous parameters and studies in a more efficient manner.

This work aims to develop a new numerical method for evaluating flow-added damping using a lightweight approach, making the method fast to compute. We will begin by conducting a literature review on numerical methods for assessing flow-added damping on flexible structures, hydrofoils and hydraulic turbines, with an emphasis on approaches focused toward reducing computational time. Afterwards, we will develop two different methods with two different formulations : the first one using a doublet-lattice panel method in order to compute the flow-added damping on hydrofoils and hydrofoils cascades and the second one being a finite element method to compute the stability of a cantilever plate.

CHAPTER 2 LITERATURE REVIEW

This chapter aims to present a literature review on numerical methods for assessing flow-added damping on hydrofoils, hydrofoil cascades, and hydraulic turbines. The emphasis is made on approaches focused towards reducing computational time. Specifically, the review considers techniques such as reduced order models, flutter analysis, and linear stability analysis, seeking to enhance computational efficiency in the evaluation of flow-induced damping.

2.1 Physical phenomena involved in hydraulic turbines

The main challenge in fluid-structure interaction numerical simulations is dealing with the coupling between the non-linear fluid flow and the solid material. Hydraulic turbines, in particular, pose additional challenges due to their intricate geometry, rotation, oscillations and turbulent high Reynolds number flows.

Rotor-stator interaction is identified as the primary factor contributing to early cracks in hydraulic turbines, as discussed by Coutu et al. (2012). The continuous vibrations of the turbine eventually result in the formation of cracks. To prevent such incidents, understanding the turbine's characteristics is crucial.

The general equation of motion of an immersed structure for one degree of freedom is

$$m_s \ddot{u}_s(t) + c_s \dot{u}_s(t) + k_s u_s(t) = F(t), \tag{2.1}$$

with m_s the structural mass, c_s the structural damping, k_s the structural stiffness, u_s the displacement field and $F(t)$ the external fluid load.

In Paidoussis (1998)'s book, the effect of the fluid flow on an immersed structure is expressed in parts as fluid-added effects and a fluid excitation force, instead of simply an external fluid force. This defines four quantities: the added mass m_f, the flow-added damping c_f, the added stiffness k_f, and the flow excitation force $\tilde{F}(t)$.

Equation 2.1 is then written with the added effects as follow

$$(m_s + m_f)\ddot{u}_s(t) + (c_s + c_f)\dot{u}_s(t) + (k_s + k_f)u_s(t) = \tilde{F}(t). \tag{2.2}$$

with m_f the added mass, c_f the flow-added damping and k_f the added stiffness.

Those factors constitute the main turbine's characteristics. Added mass represents the mass of the fluid surrounding the solid structure, moving with the solid's motion. This results in a virtual mass of the solid that exceeds its actual mass, and the disparity is known as added mass. In the case of a dense fluid like water, the added-mass is more important than for a lighter fluid like air. This will result in a reduction of the natural frequency of the structure.

Flow-added damping is more significant than structural damping in hydraulic turbines. Therefore, accurately determining this quantity is paramount. Flow-added damping plays a crucial role in diminishing vibration amplitudes. The flow-added damping can be related to the work done by the fluid on the structure over a vibration cycle (Monette et al., 2014).

Several parameters significantly affect damping, including fluid density, mode shapes, and the phase difference between the structure's response and the exciting force (Kammerer and Abhari, 2009; Dehkharqani et al., 2018). Additionally, factors such as flow velocity, viscosity, proximity to other structures, and vortex shedding also influence the flow added damping (Trivedi, 2017; Dehkharqani et al., 2018).

In the field of hydraulic turbines, various fluid-structure interaction phenomena can lead to flow-induced vibrations like vortex-induced vibrations (VIVs). VIVs occur when fluid flowing past a bluff body generates alternating vortices that trigger the motion of the structure. These alternating vortices create fluctuating pressure forces on the body possibly leading to vibration of large amplitude of the structure (Gabbai and Benaroya, 2005). They form a Von Kármán vortex street. When the vortices are shed at the same frequency as the natural frequency of the structure, we are in the lock-in region. Under those conditions, the vibration amplitudes can significantly increase due to the resonance. Those oscillations can induce damages on the structure. Tazi Labzour (2023) conducted a detailed literature review on the effects of VIVs in the case of hydraulic turbines.

2.2 Existing numerical methods

In their review, Dehkharqani et al. (2018) explore different numerical methods focusing on evaluating added mass, damping, and stiffness, especially in the context of hydraulic turbines. They cathegoriwe three distinct numerical methods:

1. modal analysis
2. fluid-structure coupled methods, one-way or two-way
3. CFD simulations integrated with a motion equation.

Table 2.1 summarizes the method used by each article presented in the literature review.

Assessing added mass is relatively straightforward, as it remains largely constant over the flow speed range found in hydraulic turbines. Numerical simulations, using elastic equations for the structure and acoustic equations for the fluid is an efficient approach for its evaluation, as demonstrated by Liang et al. (2007).

Table 2.1 Summary of numerical and experimental studies of the flow-added damping and added mass.

Source	Method type
Liang et al. (2007)	modal analysis
Karlsson et al. (2009)	CFD method
Monette et al. (2014) Gauthier et al. (2017)	one-way coupled method
Zeng et al. (2018) Liaghat et al. (2014) Zeng et al. (2018) Tengs et al. (2019a)	two-way coupled method
Seeley et al. (2012) Roth et al. (2009) Bergan et al. (2019a)	Experimental results

Monette et al. (2014) and Gauthier et al. (2017) have developed a one way coupled method that calculates flow-added damping by assessing the work exerted on the structure by the fluid. This involves employing a forced harmonic modal motion on the structure through an unsteady RANS simulation. Notably, this method focuses on one mode at a time.

On the other hand, Zeng et al. (2018) and Liaghat et al. (2014) have developed two-way coupled methods. They derive the vibration response by monitoring the mesh deformation of the flow field, allowing them to compute the natural frequency and hydrodynamic damping ratio using fast Fourier transform (FFT) and logarithmic decay methods, respectively. A primary objective of the two-way coupled method is to capture the influence of Vortex-Induced Vibration (VIV) on the flow field, a phenomenon that cannot usually be captured by one-way coupling methods.

Karlsson et al. (2009) developed a CFD method based on URANS simulations coupled with the vibration equation of the structure to estimate the torsional added inertia and damping of the Hölleforsen Kaplan runner.

2.3 Further studies on parameters influencing the flow-added damping

Zeng et al. (2019) introduce a two-way coupled Fluid-Structure Interaction (FSI) method investigating the flow-added damping of two NACA0009 hydrofoils with distinct trailing edges. The paper delves into the impact of the trailing edge on flow-added damping, revealing that the Donaldson trailing edge notably amplifies flow-added damping, particularly with increasing flow velocity. This result is attributed primarily to the position of the boundary layer separation point and the behavior of vortices in the wake. The geometry of the two trailing edges and the position of the boundary layer points are shown on Figure 2.1. In these figures, the flow goes from left to right.

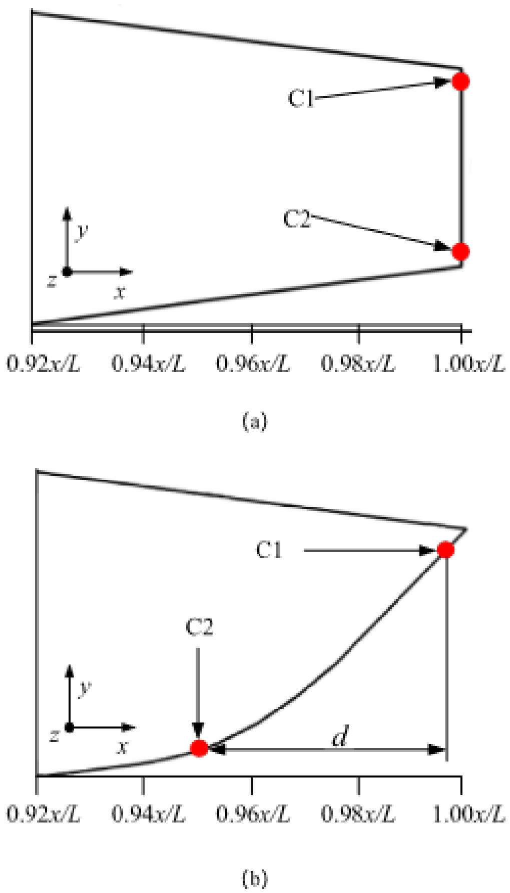

Figure 2.1 Schematic diagram of boundary layer separation points: the blunt trailing edge hydrofoil (a), the Donaldson trailing edge hydrofoil (b), from Zeng et al. (2019).

Tengs et al. (2019a) present a two-way FSI coupled approach, concentrating on studying the lock-in region and its effects on eigenfrequency and damping. Tengs et al. (2019a) observe that before entering the lock-in region, hydrodynamic damping remains approximately constant, while post-lock-in, it exhibits a linear increase with flow velocity.

Seeley et al. (2012) present an experimental exploration of damping using macrofiber composite actuators applied to specially designed hydrofoils. The study finds that eigenfrequencies are minimally affected by flow velocity, but flow-added damping exhibits a linear increase with flow velocity. Bergan (2019) and Roth et al. (2009) present experimental results from different geometries of hydrofoils, providing valuable data for the validation of numerical methods. They both observe experimentally that the flow-added damping increases with the reduced flow velocity for the first mode as shown on Figure 2.2. Roth et al. (2009) observe that the flow-added damping is almost constant and null for the first torsion mode, as shown on Figure 2.2.

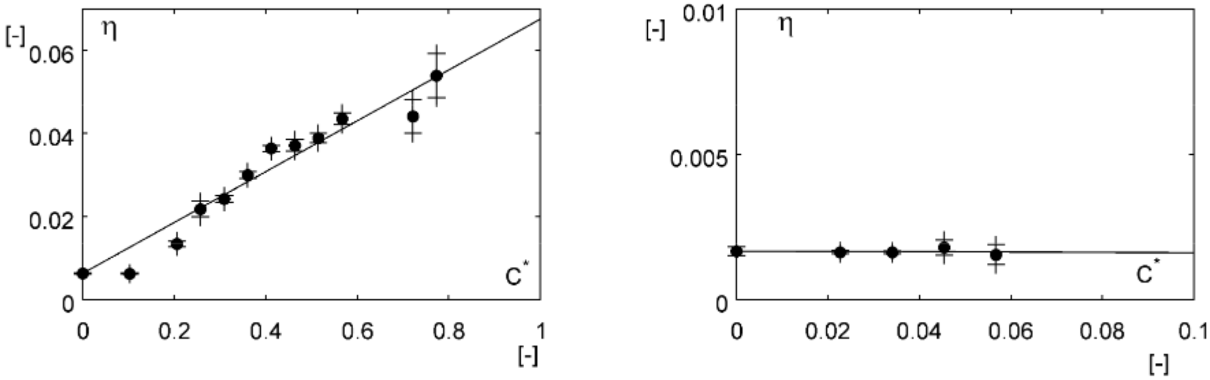

Figure 2.2 Total damping η against reduced flow velocity C^* for the 1st bending mode (left) and the 1st torsion mode (right) for the NACA0009 blunt trailing edge hydrofoil, from Roth et al. (2009).

2.4 Reduced order model

The previously mentioned methods involve the use of Computational Fluid Dynamics (CFD), or coupled Fluid-Structure Interaction (FSI) methods, with a moving mesh. However, these approaches often come with a substantial cost in terms of simulation time and computational resources. To strike a balance between precision and computational efficiency, an effective strategy is to leverage Reduced Order Models (ROMs). Using modal analysis techniques, these models represent fluid and structural displacement using mode shapes, allowing for the simplification of equations governing both fluid and structural dynamics.

Nicolle et al. (2023) explored the development of a digital twin for hydraulic turbines by incorporating ROMs. They combine finite-element analysis with fast CFD simulations on coarse grids to model the structure based on a limited number of natural modes. The predicted stresses from their method are then compared with experimental results on a hydraulic turbine and show good agreement in the operating regime and for the transient events.

2.5 Association of flow-added damping and wing flutter

The problem of aircraft wing flutter, extensively studied in aeroelasticity by Theodorsen (1949), shares similarities with the flow-added damping problem (Fung, 1955; Dowell, 1995). The primary distinction is that the fluid, water surrounding hydraulic turbine runners and vanes is dense, introducing added mass effects. In typical aircraft wing flutter scenarios, the fluid is assumed to be inviscid and irrotational, described using potential flow equations. In this thesis, we develop an innovative method for assessing flow-added damping based on the aircraft wing flutter problem. The approach relies on NASTRAN's flutter analysis module SOL 145. The *p-k* method, introduced by Hassig (1971) and implemented in NASTRAN's SOL 145 (Siemens, 2014), tackles the aeroelastic stability issue by incorporating stiffness and damping terms dependent on the structure's frequency and flow velocity. These terms are integrated into the eigenvalue problem within the modal basis, capitalizing on the computational advantages associated with this reduced order model. NASTRAN's SOL 145 is particularly effective to determine the flow-added damping coefficient in lighter fluids such as air, providing the means to extract damping coefficients and natural frequencies based on the flow velocity. Figure 2.3 shows a typical result obtained with SOL 145 for an airfoil flutter problem (Università degli Studi di Napoli Federico II, 2020). It represents the frequency and the damping as a function of velocity for several modes.

The *p-k* method is based on the doublet lattice method, a panel method where the fluid is inviscid. The instantaneous Kutta condition and non-penetration conditions are enforced on the aerodynamic panels of the structure. As noted earlier, these methods were initially developed for aeroelasticity, and thus, added mass effects were not initially considered. Modifying fluid density is insufficient to capture these effects. The key aspect of the method involves incorporating added mass into the software using the AVMI (Added Virtual Mass Incremental) factor proposed by Kwak and Kim (1991) and Louyot et al. (2020). This factor recreates added mass using the ratio of the structure's eigenfrequency in vacuum and in water, assuming that the mode shapes are similar in water and vacuum.

2.6 Linear stability analysis of a flexible cantilever

The second method introduced in this thesis adopts a very different approach, solving the problem with a finite-element method instead of a panel method. The objective is still to solve the problem in the frequency domain and assess flow-added damping through linear

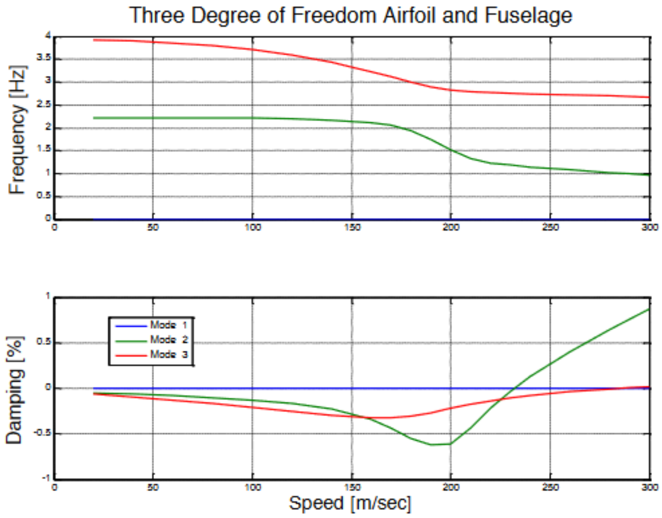

Figure 2.3 Example of SOL 145 results for a airfoil flutter problem, from Università degli Studi di Napoli Federico II (2020).

stability analysis. We therefore use exponential solutions for the fluid and solid variables proportional to $e^{i\omega t}$. The development of the linearized Navier-Stokes equations for the fluid domain and the linear elastic equations for the structure will give us an eigenvalue problem in ω from which it is possible to extract the damping from the imaginary part of the eigenvalue found and the frequency from the real part of this eigenvalue.

The study of flutter instability in a cantilever plate is a fundamental fluid-structure interaction problem with applications across various engineering fields (Cisonni et al., 2017). In our research, examining a flexible cantilever plate serves as an initial step toward a hydraulic turbine design. Due to the high velocities and large reference lengths involved, most studies in the literature typically neglect viscosity, using ideal flow models such as potential flow theory (Guo and Païdoussis, 2000; Howell et al., 2009). Guo and Païdoussis (2000) used a linear beam equation for the structure and a potential flow formulation for the fluid, with an imposed Kutta condition at the trailing edge of the plate. The imposed Kutta condition is a way to implicitly model the effect of viscosity. They found that the cantilever plate loses stability with a single-mode flutter (of the second mode) with a critical velocity dependent of the solid and fluid mass ratio as shown on Figure 2.4, which represents the complex eigenvalue real part and imaginary part as a function of the reduced velocity. The imaginary part of the second mode eigenvalue becomes negative at the single-mode flutter for a reduced velocity around $\bar{U} = 5$. The reduced velocity is the ratio between the flow velocity and the natural frequency of the structure times a characteristic length. They found that the first mode remains stable for all values of reduced velocity tested, as its imaginary part is positive and increases with the reduced velocity. Howell et al. (2009) developed a similar method using a boundary-element panel method. The Kutta condition was also enforced at the trailing edge with a zero pressure difference. This was achieved through the boundary conditions consisting of applying continuity of vortex strength at each panel end points and a zero vorticity condition at the trailing edge.

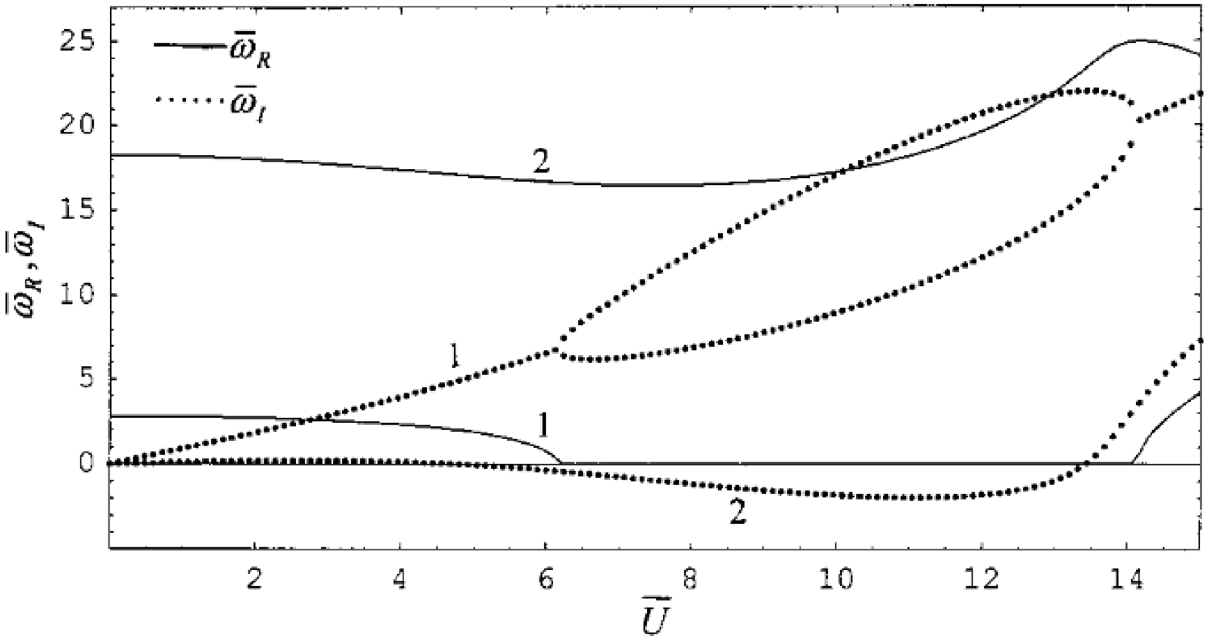

Figure 2.4 Dimensionless complex eigenfrequencies versus flow velocity for a clamped-free plate; $c = 1$ and $\mu = 1$. The single-mode fluter occurs when the imaginary part of the complex eigenvalue becomes negative around $\bar{U} = 5$, from Guo and Païdoussis (2000).

Because of a higher computational cost, relatively few studies have developed viscous models for the same problem, solving the Navier-Stokes equations that explicitly take into account viscosity (Cisonni et al., 2017). Those studies would be particularly interesting to study the flow field with more precision and the vortices in the wake of the plate. Cisonni et al. (2017) developed a numerical model using one-dimensional elastic Kirchhoff-Love beam model for the cantilever coupled with a viscous fluid model. Their numerical method uses a time-marching algorithm to couple the fluid and solid domain. They showed that a decrease in the Reynolds number would make the fluid-structure interaction system more stable, as the viscosity increases. They made a parametric study to extract stability curves as a function of geometric parameters as well as Reynolds number or solid and fluid mass ratio. Their method required about 150,000 CPU hours to run 120,000 simulations, developing a quicker method is therefore crucial to be able to analyze the stability of more complex structures.

With the intention of developing a quicker method of the same problem as Cisonni et al. (2017), Couture (2020) presented two numerical methods in his work — one employing potential theory to simulate the fluid and the other one using a linearized Navier Stokes formulation. Couture (2020)'s formulation was initially inspired by the work of Fernández and Le Tallec (2003) who propose a linearization of the Arbitrary Lagrangian-Eulerian (ALE) equations for fluid-structure interaction into an Eulerian formulation. This formulation also served as inspiration for Pfister et al. (2019), who developed a numerical method similar to Couture's but with a different coupling approach. To couple the fluid and solid domains, they introduced an extension displacement field defined within the fluid domain. In Couture (2020)'s formulation, the coupling terms at the fluid-structure interface were defined with the transpiration method, developed by Lighthill (1958), to implement the kinematic boundary condition. For the dynamic boundary condition, the continuity of the boundary stress tensors of the two domains was enforced.

Couture (2020)'s work was promising, having two fast methods to evaluate the stability of the flexible cantilever respectively immersed in a potential or viscous flow. However, he showed that the circulation could not be well implicitly imposed in the potential method, leading to inaccurate results in some cases, while the viscous method resulted in non-negligible deformation of the structure due to the shear induced by the viscous base flow.

Gosselin (2006) showed that in the case of a viscous flow, the destabilizing term in the boundary condition at the fluid-structure interface is not taken into account. This occurs because the no-slip boundary condition on the structure renders the transverse velocity of the fluid null at the interface. That is a consequence of applying the boundary conditions at the reference mean position of the structure instead of its instantaneous deformed position. Accurately determining the deformed position of the structure necessitates a large amplitude analysis and, consequently, a non-linear model. One of the solutions presented by Gosselin (2006) is to use a free-slip boundary condition on the structure for the base flow while keeping the small perturbation flow viscous. Although this hybrid method has limited realism, it was shown to predict accurately the dynamic of the system studied. Furthermore, at large Reynolds number, a plug flow profile better represents the flow than a Poiseuille profile, yet viscous effects can have an important role in a perturbation flow. Another solution developed was to apply the boundary conditions at an assumed position just off the mean position of the structure, similarly to what Dowell (1971) and El Chebair et al. (1990) did. The second method presented in this thesis is inspired by the hybrid method of Gosselin (2006), having a different treatment for the base flow and the small perturbation flow. This is motivated to have on one hand a correct implementation of the kinematic boundary condition at the interface with the free-slip boundary condition of the base flow, and on the other hand to model accurately the fluctuating circulation in the wake thanks to a viscous perturbation flow.

CHAPTER 3 SYNTHESIS OF THE LITERATURE REVIEW AND OBJECTIVES OF THE PROJECT

3.1 Synthesis of the literature review

Rotor-stator interaction is an important source of excitation in hydraulic turbines and it cannot be completely avoided (Coutu et al., 2012). In order to accurately compute the vibration amplitude to determine the fatigue life estimation of the turbine, the flow-added damping is crucial. Nowadays, several methods were developed to estimate this quantity. Most of these methods rely on CFD simulations or either one-way or two-way fluid-structure interactions (Dehkharqani et al., 2018). Not only are these methods computationally expensive, but they also introduce challenges related to dynamic mesh strategies required to properly capture the structure motion. In order to reduce computational time, ROMs have been studied. Flow-added damping is closely linked to the phenomena of flutter and circulation fluctuations in the flow (Cisonni et al., 2017).

Doublet-lattice panel methods could provide a reliable method to assess the flow-added damping. Those methods were initially developed for flutter analysis of aircraft wings in light fluids like air (Siemens, 2014), but if one could adapt them to denser fluids like water, with the challenge of taking into account the added mass effect, they could be an alternative method. This can be achieved with the AVMI factor (Louyot et al., 2020; Kwak and Kim, 1991), which recreate virtually the added mass for a specific mode. The flow-added damping is evaluated via a linear stability analysis, corresponding to the imaginary part of the eigenfrequency solution of the problem.

However, the generalization to complex structures with internal flow can be challenging. That is the case of hydraulic turbines where the panels would have to present curvatures and the flow field will need to be able to take into account rotational effects.

In order to have a generalizable method, the finite-element method could be employed, as it can represent any geometries. Research on the stability of a flexible cantilever subjected to axial flow would be the first step towards studying the characterizes of a more complex system. This problem was addressed many times over the past few years. Many studies however only considered ideal flow models for the fluid domain (Guo and Païdoussis, 2000; Howell et al., 2009). This requires an imposed Kutta condition at the trailing edge of the plate in order to accurately model the wake. Studies taking into account viscous effects were marginally developed, with promising results but were very computationally expensive

(Cisonni et al., 2017). Hybrid models combining a distinct treatment of the mean base flow and the small perturbation flow showed promising results (Gosselin, 2006). They predicted accurately the fluctuations in the wake with their viscous perturbation flow, while having a relatively simple kinematic boundary condition at the fluid-structure interface because of the free-slip of the base flow on the structure.

3.2 Goals

In this thesis, we developed two distinct flow-added damping evaluation methods, corresponding to two different objectives. One corresponding to a first objective based on a doublet-lattice panel method. The test cases were single straight hydrofoils and hydrofoil cascades. This method was later found to be limited in terms of generalization to more complex geometries. The second objective was therefore to developed a finite-element method to compute the flow-added damping and more generally the stability of a slender structure in axial flow. That method must be generalizable to more complex geometries with rotational effects, just like a hydraulic turbine runner or vane.

The objectives of the project can be summarized as follow :

- Develop a double-lattice panel method able to assess the flow-added damping via flutter analysis.
- Develop a finite-element method able to assess the flow-added damping via linear stability analysis and generalizable to complex geometries.

CHAPTER 4 FLUTTER ANALYSIS METHOD

Personal contribution

This chapter corresponds mainly to a rewriting of Lamoureux et al. (2023). This project was initially started by Danick Lamoureux and continued by myself. Danick Lamoureux developed the automation code in python, in order to extract the results for a given hydrofoil geometry and the first study of the test cases NACA0003, F0 and F1. My contribution includes modifying the meshing technique, conducting convergence analysis, replicating results for the three original test cases plus two additional ones involving the NACA0009 hydrofoils, and collaborating with Danick Lamoureux to review and refine the physical equations. I studied the cascade of hydrofoils.

4.1 Physical model

In order to develop a quick method to evaluate the flow-added damping, we consider a flutter analysis method based on a panel method. The fluid is modeled with the potential theory, it is considered irrotationnal and inviscid.

4.1.1 Governing equations

The general equation of motion $\boldsymbol{u_s}$ of a structure with a structural mass matrix $[M_s]$, structural damping matrix $[C_s]$, structural stiffness matrix $[K_s]$, subjected to the external load $\boldsymbol{F(t)}$ is

$$[M_s]\boldsymbol{\ddot{u}_s(t)} + [C_s]\boldsymbol{\dot{u}_s(t)} + [K_s]\boldsymbol{u_s(t)} = \boldsymbol{F(t)}. \tag{4.1}$$

When this structure is immersed in a dense fluid, the added effects are taken into account as follow (Gauthier et al., 2017; Paidoussis, 1998)

$$([M_s] + [M_f])\boldsymbol{\ddot{u}_s(t)} + ([C_s] + [C_f])\boldsymbol{\dot{u}_s(t)} + ([K_s] + [K_f])\boldsymbol{u_s(t)} = \boldsymbol{\tilde{F}(t)}, \tag{4.2}$$

where $[M_f]$ is the added mass matrix, $[C_f]$ the added damping matrix, $[K_f]$ the added stiffness matrix and $\boldsymbol{\tilde{F}(t)}$ the excitation force.

In order to reduce the order of this equation, we use the modal decomposition. We perform a modal analysis to extract the eigenvalues and eigenvectors of our system. The displacement field is written under the modal form with ω the complex eigenvalue as follow

$$\boldsymbol{u_s(t)} = \boldsymbol{\phi_i} e^{i\omega t}. \tag{4.3}$$

The eigenvalue problem is therefore

$$[-\omega^2([M_s] + [M_f]) + i\omega([C_s] + [C_f]) + ([K_s] + [K_f])]\boldsymbol{\phi_i} = 0. \tag{4.4}$$

The results of this eigenvalue problem will be the complex eigenvalues ω and the mutually orthogonal eigenvectors $\boldsymbol{\phi_i}$ with which we can assemble into a modal basis matrix $[\Phi]$:

$$[\Phi] = [\phi_1 \phi_2 ... \phi_3]. \tag{4.5}$$

The displacement field can be written in the modal basis as follow

$$\boldsymbol{u_s(t)} = [\Phi] \cdot \boldsymbol{u_h(t)}, \tag{4.6}$$

where $\boldsymbol{u_h}$ is the modal coordinates. Equation 4.2 is written in the modal base as follow

$$[-\omega^2[\Phi]^T([M_s] + [M_f])[\Phi] + i\omega[\Phi]^T([C_s] + [C_f])[\Phi] + [\Phi]^T([K_s] + [K_f])[\Phi]]\boldsymbol{u_h} = 0, \tag{4.7}$$

which becomes

$$-\omega^2([M_{hh,s}] + [M_{hh,f}])\boldsymbol{u_h} + i\omega([C_{hh,s}] + [C_{hh,f}])\boldsymbol{u_h} + ([K_{hh,s}] + [K_{hh,f}])\boldsymbol{u_h} = 0, \tag{4.8}$$

with $[M_{hh,s}]$ and $[M_{hh,f}]$ respectively the structural modal mass matrix and the modal added mass matrix, $[C_{hh,s}]$ and $[C_{hh,f}]$ respectively the structural modal damping matrix and the modal added damping matrix and $[K_{hh,s}]$ and $[K_{hh,f}]$ respectively the structural modal stiffness matrix and the modal added stiffness matrix.

The first advantage of using eigenvectors to create a modal basis is to reduce the order of the system to m modes compared to n degrees of freedom previously, with $m \ll n$ (Tengs et al., 2019a). The second advantage is that the reduced system will be diagonal because of the orthogonality of the eigenvectors. The system of equation is therefore much easier and faster to solve.

The complex eigenvalues can be rewritten as a function of the natural frequency f and the damping ratio ζ

$$\omega = 2\pi f(\pm 1 + i\zeta). \tag{4.9}$$

4.1.2 NASTRAN aeroelastic

In a NASTRAN aeroelastic flutter analysis, the *p-k* method solves the following equation (Siemens, 2014)

$$[-\omega^2[M_{hh,s}] + i\omega([C_{hh,s}] - \frac{1}{4k}\rho c U[Q^I_{hh}]) + ([K_{hh,s}] - \frac{1}{2}\rho U^2[Q_{hh}]^R)]\boldsymbol{u_h} = 0, \tag{4.10}$$

with ρ the density of the fluid, c the reference length, k the reduced frequency, U the velocity and $[Q_{hh}]$ is the modal aerodynamic influence matrix with $[Q_{hh}]^I$ and $[Q_{hh}]^R$ its imaginary and real parts respectively.

The *p-k* method used by NASTRAN to solve the aeroeslatic stability uses velocity dependent terms for stiffness and damping. The method allows solving equations such as Equation 4.10. This type of equation depends on two variables simultaneously, the velocity and the reduced frequency. The *p-k* algorithm is an iterative process based on both the variation of velocities and the convergence of the reduced frequencies. It enables the direct extraction of results for different velocity values (Biskri, 2007).

With $k = \dfrac{2\pi f c}{2U}$, Equation 4.10 becomes

$$[-\omega^2[M_{hh,s}] + i\omega([C_{hh,s}] - \frac{1}{4\pi f}\rho U^2[Q_{hh}]^I) + ([K_{hh,s}] - \frac{1}{2}\rho U^2[Q_{hh}]^R)]\boldsymbol{u_h} = 0. \tag{4.11}$$

Equation 4.11 can be assimilated to Equation 4.8 developed before. The only difference is the added mass matrix. Indeed, those methods were initially developed for lighter fluids study such as air where the added mass effect is usually not taken into account. In our cases the fluid is dense and the added mass effects cannot be neglected. The added mass terms are therefore recovered through the AVMI factor, as developed in the next section.

4.1.3 Recreating the added mass via the AVMI factor

In order to recover the effect the added mass, we use the AVMI factor β (Louyot et al., 2020; Kwak and Kim, 1991). It is a function of the natural angular frequency of the structure in vacuum ω_{vac} and the natural angular frequency in the resting fluid ω_f

$$\frac{\omega_f}{\omega_{vac}} = \frac{1}{\sqrt{1+\beta}}. \tag{4.12}$$

This definition is valid under the assumption of similar mode shapes in vacuum and resting fluid. This assumption will be verified in all our following test cases before using the AVMI factor. The AVMI factor can also be defined as the ratio between the reference kinetic energy of the fluid and the reference kinetic energy of the structure (Louyot et al., 2020).

The natural angular frequency in vacuum and in resting fluid can be expressed as follow

$$\omega_{vac} = \sqrt{\frac{k_s}{m_s}}, \tag{4.13}$$

and

$$\omega_f = \sqrt{\frac{k_s + k_f}{m_s + m_f}} = \sqrt{\frac{k_s}{m_s + m_f}}. \tag{4.14}$$

The effect of the added stiffness is negligible compared to the effect of the added mass, therefore k_f is neglected here. The ratio of the natural angular frequency in vacuum and in resting fluid becomes

$$\frac{\omega_{vac}}{\omega_f} = \sqrt{\frac{k_s.(m_s + m_f)}{k_s.m_s}} = \sqrt{\frac{m_s + m_f}{m_s}}. \tag{4.15}$$

For each mode i, we let $P_i = \frac{\omega_{i,vac}}{\omega_{i,f}} = \sqrt{1 + \beta_i}$ which gives

$$m_{s,i} + m_{f,i} = m_{s,i} \cdot P_i^2. \tag{4.16}$$

Considering that the structural modal mass matrix is diagonal, we have the following expression for the added mass matrix

$$[M_{hh,s}] + [M_{hh,f}] = [M_{hh,s}][P]^2, \tag{4.17}$$

with $[P]$ the diagonal matrix of the P_i.

The modified eigenvalue problem which accounts for the added mass implemented in NASTRAN becomes

$$[-\omega^2[M_{hh,s}].[P]^2 + i\omega([C_{hh,s}] - \frac{1}{4\pi f}\rho U^2[Q_{hh}]^I) + ([K_{hh,s}] - \frac{1}{2}\rho U^2[Q_{hh}]^R)]\boldsymbol{u_h} = 0. \tag{4.18}$$

4.2 Results

4.2.1 Definitions of the test cases

In order to validate the methodology presented before, we compare our results with the literature for several test cases. Our goal is to select different material properties, profile and boundary conditions, and then to compare our results with both experimental results and numerical results from the literature.

The first test case is based on the geometry used by Cupr et al. (2018), a NACA0003 with a modified trailing edge of 1 mm. This hydrofoil was studied numerically on ANSYS CFX with a two way coupling method. The second and third test cases are the F0 and F1 hydrofoil, which were studied both experimentally and numerically using one way coupling (Bergan et al., 2019a; Tengs et al., 2019b). The last two test cases are both NACA0009 profile shape but with two different trailing edges, Blunt and Donaldson. The Blunt one was studied experimentally by Roth et al. (2009) and they were both studied numerically by Zeng et al. (2019), using two way coupling. Those last two cases are clamped at one end whereas the other three are clamped at both ends. Figure 4.1 present their geometry and Table 4.1 their dimensions and material properties.

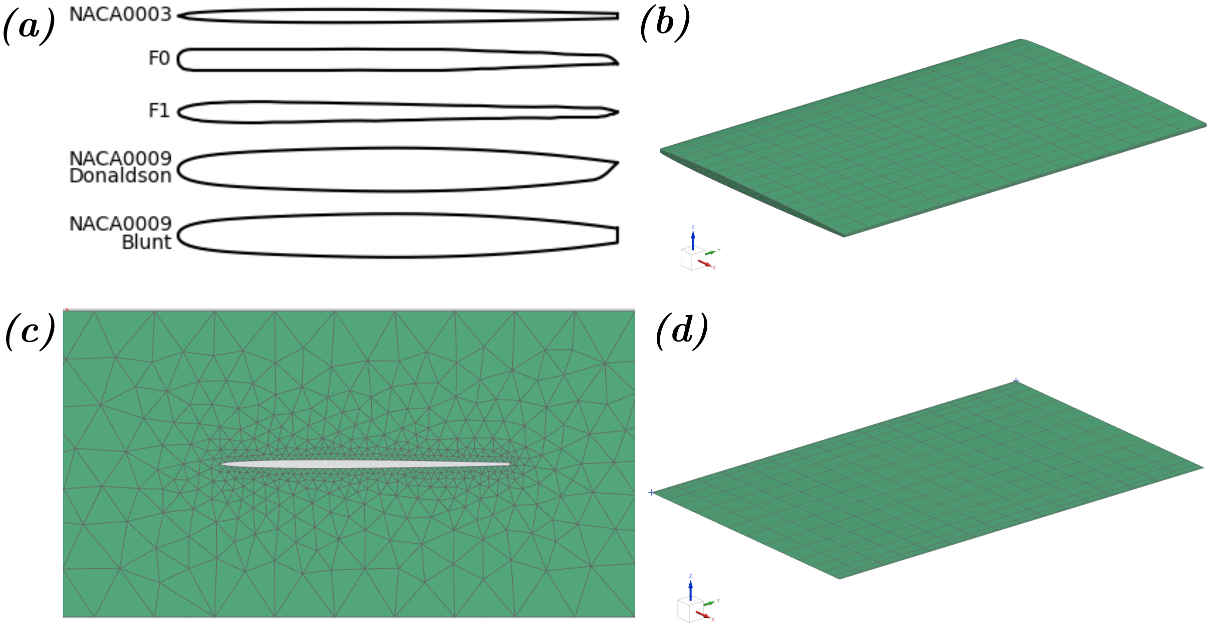

Figure 4.1 a) Profile of the hydrofoils (Cupr et al., 2018; Bergan et al., 2019a; Zeng et al., 2019); b) Structural mesh of the NACA0003 hydrofoil; c) Zoom of a transverse cut of the acoustic fluid mesh of the NACA0003 hydrofoil (the full mesh is 6-chords long); d) Aerodynamic panels mesh of the NACA0003 hydrofoil.

4.2.2 Mesh information

The different profiles were either drawn from illustrated figures or designed with their known equation of definition. Since the hydrofoils studied are standalone and straight, the mesh

Table 4.1 Hydrofoils materials and dimensions (Cupr et al., 2018; Tengs et al., 2019b; Bergan et al., 2019a; Zeng et al., 2019).

Hydrofoil	Chord [mm]	Span [mm]	Max thickness [mm]	Test section's thickness [mm]	Material	Young's modulus [GPa]	Poisson's ratio	Density [kg m^{-3}]
NACA0003	95	150	3.4	100	Bronze	115	0.33	7800
F0	250	150	12	150	Aluminum	68.89	0.33	2711
F1	250	150	12	150	Aluminum	68.89	0.33	2711
NACA0009 (Donaldson trailing edge)	100	150	10	150	Steel	215	0.3	7700
NACA0009 (Blunt trailing edge)	100	150	10	150	Steel	215	0.3	7700

was made from quadratic pentahedric elements, also called CPENTA in NASTRAN, both for structural and fluid elements, since the hydrofoil can be seen as an extruded profile. Moreover, the test sections used for the different hydrofoils can also be represented within this program by modifying the test section thickness and length, the width being constrained to the hydrofoil's span and the boundary conditions applied to the fluid around the hydrofoil being a rigid wall. The mesh size of the fluid domain is smaller close to the hydrofoil and increases when further from the structure.

4.2.3 Modal analysis

As mentioned before, the AVMI factor needs to be computed. It is the ratio of the natural frequencies in vacuum and in water. The first step is to perform a modal analysis in vacuum with SOL 103 of NASTRAN. A vibro-acoustic analysis is then performed to extract the natural frequency in water via SOL 107 of NASTRAN. The meshes of those two analysis are presented in Figure 4.1.

Convergence Analysis

In order to show the convergence of our results, we present a detailed case of convergence analysis for the F1 hydrofoil using the procedure described by Celik et al. (2008) using the Richardson extrapolation method. First, a convergence analysis was performed on the solid elements when considering a modal analysis in vacuum. We compute the extrapolated reference value, and we calculate the error as the relative difference between the natural frequency in vacuum for a given mesh and this reference value $e = |f - f_{ref}|/f_{ref}$, as shown in Figure 4.2a. The relative error is less than 1 % with a solid element size of 6 mm, knowing that the chord is 250 mm. We then perform a convergence analysis of the fluid elements, using the same definition as in the previous convergence analysis but with the natural frequency in resting fluid and maintaining the solid element size as 6 mm, such as in Figure 4.2b. We also maintain the length of the channel as $6c$ as the following convergence analysis will discuss. The relative error for the fluid elements is less than 1 % with a fluid element size of 10 mm, considering the channel length of $6c$, which is 1500 mm. Finally, Figure 4.2c presents the influence of the test section length on the natural frequency in water. The error is defined as previously, but using the longest simulated test section as the reference value. The error is plotted against the test section length ℓ over the chord c. Once the test section length is long enough (around 6 times the cord), it does not influence the natural frequency anymore, as it plateaus to an error very close to zero. The convergence analysis regarding the fluid elements and test section length was produced such that both parameters would not influence each other. This shows that our cases are well converged and that the following results can be interpreted reliably.

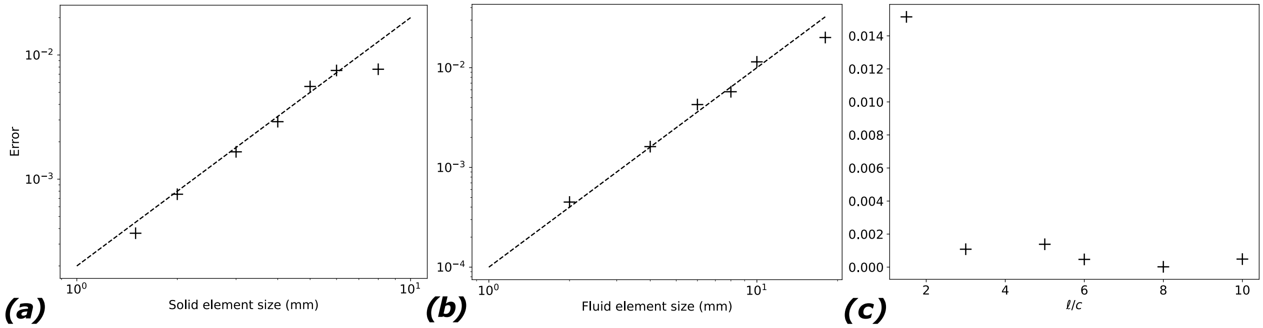

Figure 4.2 Convergence analysis of the F1 hydrofoil case: a) Convergence analysis of the solid elements through a modal analysis in vacuum. b) Convergence analysis of the fluid elements through a modal analysis in resting fluid. c) Convergence analysis of the length of the channel in modal analysis in resting fluid.

Comparison with literature and limitations

The modes shapes and modal frequencies are extracted from from those simulations. We compare our results with values in the literature for the natural frequencies in vacuum or in resting fluid or both. The focus is on the first mode called the bending mode because it is the one studied in the different articles. This comparison is shown in Table 4.2. The number of solid and fluid elements are also presented. Our meshes have fewer elements than other numerical simulations. This is because we use quadratic pentahetric elements, which uses 15 nodes per element instead of 8 nodes per element for the linear hexahedric elements.

The natural frequencies are well predicted for the F1 and the NACA0009 cases. However, some differences between our results and the literature can be pointed out. The hydrofoils have particular profiles that we had to reproduce manually from the literature's images. For example, the F0 and F1 hydrofoils are custom made and the NACA hydrofoils all have modified trailing edge. The inexact geometry of our profiles might have altered the natural frequencies of our test cases. The boundary conditions might also have introduced discrep-

Table 4.2 Hydrofoils' first modal frequencies in vacuum and resting fluid with fine meshes and from the literature (Roth et al., 2009; Cupr et al., 2018; Bergan et al., 2019a; Tengs et al., 2019b; Zeng et al., 2019).

Hydrofoil	Source	Solid elements	Fluid elements	Test section's length [$\bar{c}$]	$f_{1,vac}$ [Hz]	$f_{1,fr}$ [Hz]
NACA0003	Finer mesh	3 800 PENTA	23 300 PENTA	6.0	429.31	188.10
	Numerical reference (Cupr et al., 2018)	17 500 HEX	328 000 HEX	-	321	140
F0	Finer mesh	5 320 PENTA	12 400 PENTA	6.0	1951.38	720.79
	Experimental reference (Bergan et al., 2019a)	-	-	-	-	approx. 625
F1	Finer mesh	2 280 PENTA	9 780 PENTA	6.0	1562.22	530.89
	Numerical reference (Tengs et al., 2019b)	-	5×10^6 HEX	-	-	504.37
NACA0009	Finer mesh	2 640 PENTA	13 300 PENTA	7.5	336.27	225.96
Donaldson trailing edge	Numerical reference (Zeng et al., 2019)	-	-	7.5	290.71	183.48
NACA0009	Finer mesh	2 640 PENTA	14 860 PENTA	7.5	335.24	224.53
Blunt trailing edge	Experimental reference (Roth et al., 2009)	-	-	7.5	-	194
	Numerical reference (Zeng et al., 2019)	-	-	7.5	289.34	185.74

ancies. In our cases, we assume the hydrofoil to be perfectly clamped, which might not be the case for the experimental analysis. The flexibility in the clamps reduces the stiffness of the structure and therefore reduces the natural frequency. This would explain why we predict higher natural frequencies compared to the literature. It is also possible that the uncertainties of measurement of the experimental results explain those differences.

Despite those errors, we show in the next section that the flow-added damping can be accurately predicted, which is the goal of this method.

4.2.4 AVMI factor

Figure 4.3 represents the mode shapes in vacuum and resting fluid for the first mode. We can see that the modes shapes are very similar but with a different amplitude. In order to correctly assign the modes, we use the Modal Assurance Criterion (MAC) for the first ten modes in vacuum (Pastor et al., 2012). We associate for each vacuum mode the corresponding mode in water with the highest MAC. This allows us to correctly pair every mode. Indeed, the first ten modes in water do not necessarily correspond to the first ten modes in vacuum, because of the presence of more modes in water. The MAC is defined as follow for two vectors $\boldsymbol{\psi_i}$ and $\boldsymbol{\phi_j}$

$$MAC_{i,j} = \frac{|\boldsymbol{\psi_i^T}\boldsymbol{\phi_j}|^2}{\left(\boldsymbol{\psi_i^T}\boldsymbol{\psi_i}\right)\left(\boldsymbol{\phi_j^T}\boldsymbol{\phi_j}\right)}. \tag{4.19}$$

The MAC for the first ten modes of the different test cases are listed in Table 4.3 It can be seen that the MAC are high in most cases (>0.9) even though some resting fluid modes tends to deviate from the vacuum one, especially for the F0 and F1 hydrofoil with 0.55 and 0.65 MAC for the second mode. Another observation is that the first mode when performing the vibro-acoustic simulation is a rigid body mode with a frequency of 10^{-5} Hz, and the second mode is a fluid mode with a structural displacement 10^{-3} times smaller than the other structural modes. However, most of the modes are correctly associated between the two modal analysis. Therefore the P matrix of the ratios of eigenvalues can be accurately constructed and implemented for the aeroelastic analysis. Table 4.4 presents the different terms of this matrix.

Table 4.3 Modal assurance criterion between the i^{th} vacuum and j^{th} resting fluid mode shapes for the NACA0003, F0, F1, Donaldson and Blunt NACA0009 hydrofoils. A value near unity means good correspondence between the two mode shapes.

NACA0003	$MAC_{1,2}$	$MAC_{2,3}$	$MAC_{3,4}$	$MAC_{4,5}$	$MAC_{5,6}$	$MAC_{6,7}$	$MAC_{7,10}$	$MAC_{8,9}$	$MAC_{9,11}$	$MAC_{10,12}$
	1.000	1.000	0.997	0.990	0.990	0.980	0.987	0.965	0.986	0.972
F0	$MAC_{1,3}$	$MAC_{2,5}$	$MAC_{3,7}$	$MAC_{4,10}$	$MAC_{5,11}$	$MAC_{6,17}$	$MAC_{7,14}$	$MAC_{8,19}$	$MAC_{9,24}$	$MAC_{10,34}$
	0.919	0.557	0.876	0.993	0.919	0.941	0.880	0.889	0.993	0.843
F1	$MAC_{1,3}$	$MAC_{2,4}$	$MAC_{3,7}$	$MAC_{4,10}$	$MAC_{5,9}$	$MAC_{6,15}$	$MAC_{7,13}$	$MAC_{8,16}$	$MAC_{9,17}$	$MAC_{10,21}$
	0.929	0.666	0.946	0.934	0.985	0.953	0.891	0.788	0.743	0.901
NACA0009	$MAC_{1,2}$	$MAC_{2,3}$	$MAC_{3,5}$	$MAC_{4,7}$	$MAC_{5,8}$	$MAC_{6,10}$	$MAC_{7,18}$	$MAC_{8,19}$	$MAC_{9,28}$	$MAC_{10,1}$
Donaldson	1.000	0.999	0.988	1.000	0.999	0.887	0.988	0.985	0.980	0.9078
NACA0009	$MAC_{1,2}$	$MAC_{2,3}$	$MAC_{3,5}$	$MAC_{4,7}$	$MAC_{5,9}$	$MAC_{6,11}$	$MAC_{7,19}$	$MAC_{8,22}$	$MAC_{9,32}$	$MAC_{10,1}$
Blunt	1.000	0.999	0.988	1.000	0.999	0.893	0.988	0.994	0.986	0.905

Table 4.4 Ten first AVMI matrix diagonal components for the NACA0003, F0, F1 and NACA0009 hydrofoils.

Hydrofoil	P_1	P_2	P_3	P_4	P_5	P_6	P_7	P_8	P_9	P_{10}
NACA0003	2.2824	1.7111	1.8794	1.6289	1.5190	1.6877	1.4933	1.5532	1.5653	1.4613
F0	2.7073	2.3377	1.7434	1.8253	1.5895	1.4936	1.8709	1.6498	1.5828	1.5470
F1	2.9426	2.4534	1.8347	1.6913	1.9420	1.5901	1.8940	1.7391	1.8379	1.5961
NACA0009 Donaldson	1.4882	1.2605	1.3370	1.0042	1.2321	1.3138	1.1861	1.2053	1.1639	3.01e7
NACA0009 Blunt	1.4933	1.2631	1.3395	1.0077	1.2336	1.3116	1.1862	1.2016	1.1607	3.01e7

4.2.5 Flow-added damping

The aeroelastic analysis is the last step towards the extraction of the flow-added damping. The mesh used for this simulation is composed of CAERO1 elements in NASTRAN. Those elements are doublet-lattice panels. As mentioned before, this method is based on potential flow theory, so the viscosity is not modeled, but its influence on the fluctuating circulation is accounted for by enforcing an instantaneous Kutta condition. The simulation in NASTRAN allows us to extract the complex eigenvalues, and therefore the natural frequency and the dimensionless damping for each test case. We define the reduced velocity $U_R = \frac{U}{f_{0,1}h}$ with U the flow velocity, $f_{0,1}$ the natural frequency of the first mode of the hydrofoil considered and h its thickness. We define the dimensionless frequency $\Omega_i = \frac{f_i}{f_{0,1}}$ with f_i the frequency of mode i. Those results can be plotted against the reduced velocity and be compared with experimental or numerical results from the literature. In our model, we did not consider any

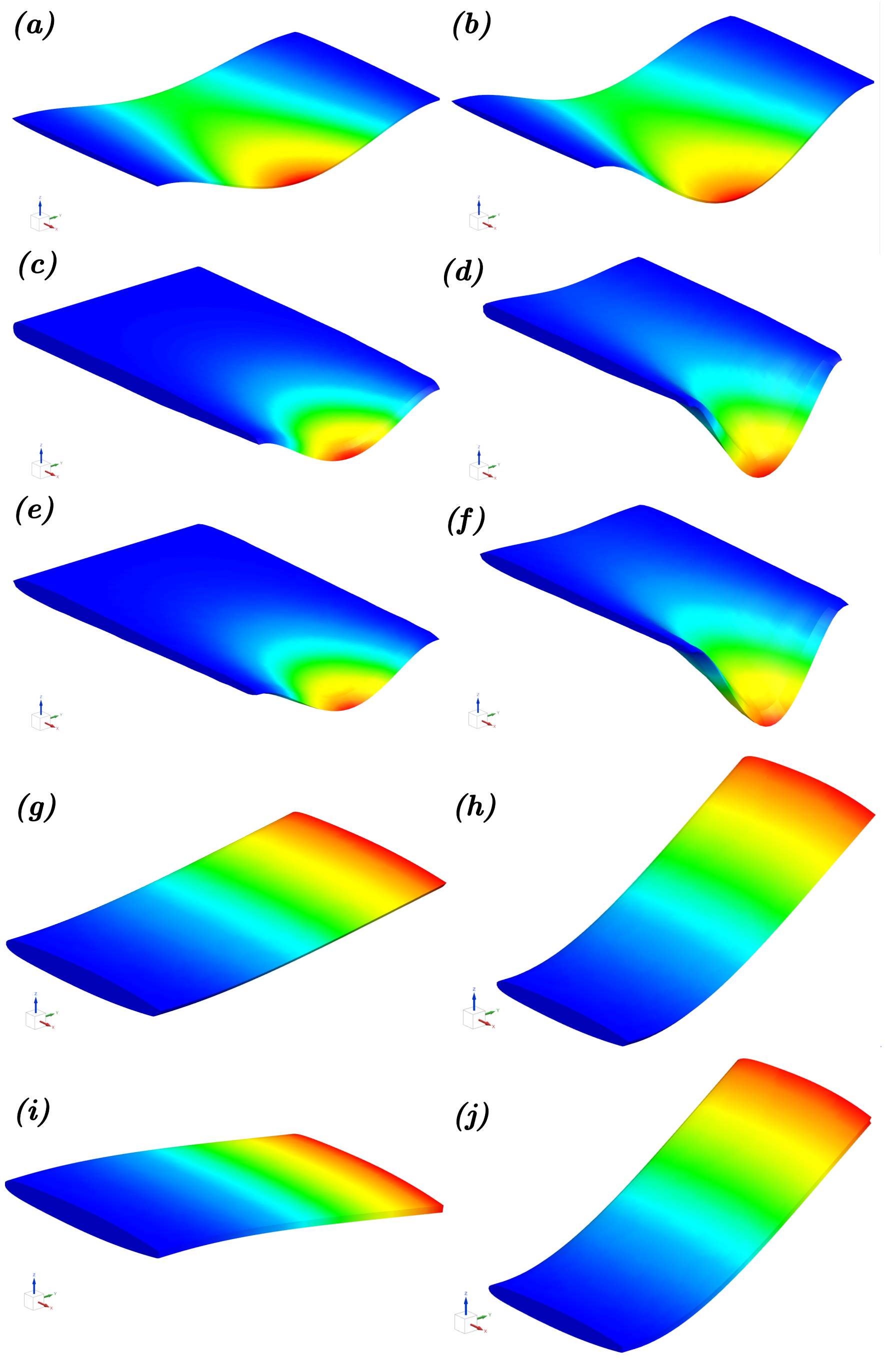

Figure 4.3 Hydrofoils first bending modes in vacuum and resting fluid: NACA0003's first bending mode in a) vacuum, b) resting fluid; F0's first bending mode in c) vacuum, d) resting fluid; F1's first bending mode in e) vacuum, f) resting fluid; NACA0009 Donaldson's first bending mode in g) vacuum, h) resting fluid and NACA0009 Blunt's first bending mode in i) vacuum, j) resting fluid.

structural damping, whereas for the literature results, structural damping could be present. In order to present a fair comparison of the flow-added damping with our results, we need to correct the damping values of the literature by subtracting the structural damping. The structural damping is the damping value when the flow velocity is null. We can now compare our results with the shifted results from the literature, Figure 4.4 represents the hydrofoil dimensionless natural frequency and flow-added damping against the reduced velocity. The continuous lines are our results, and the dotted lines represent the literature results.

From Figure 4.4, we observe that for all cases the flow-added damping increases with the reduced velocity. We also observe a good agreement between our results obtained from NASTRAN and the literature results, especially for the F0 and F1 test cases. For the NACA0009 cases, we slightly underestimate the flow-added damping, but the trend is similar. From our results, we can define two distinct regions, the first one where the flow-added damping is almost constant and negligible, and the second regions where it increases linearly with the reduced velocity. This concept was previously elaborated by Zeng et al. (2023) delineating two distinct regions of flow-added damping. The delimitation between those two regions is the lock-in phenomenon. Lock-in is observed when the vortex shedding frequency is equal to the structure natural frequency, which is represented as dashed lines for the F0 and F1 cases. During the lock-in range, the vortices shed on the trailing edge influence the dynamics of the structure, and this phenomenon cannot be captured by our model which is based on potential flow. From Figure 4.1 we can see that the NACA0009 cases present a thicker aspect ratio and thicker trailing edges. Therefore, they will experience more unsteady effects due to the shedding of larger vortices. This is one of the reason why our results underestimate the flow-added damping of those cases, while predicting similar trends.

With our method, we can also easily evaluate the natural frequencies and the flow-added damping for higher modes. Indeed, the previously presented results were only for the first mode, the bending mode, because it is the only one studied in the literature. However, our method can predicted higher modes and keep the computation time low. Figure 4.5 present the evolution of the first three modes for each test cases. As expected, the natural frequencies increases with higher modes, and the flow-added damping decreases because the first mode is the one with the most energy.

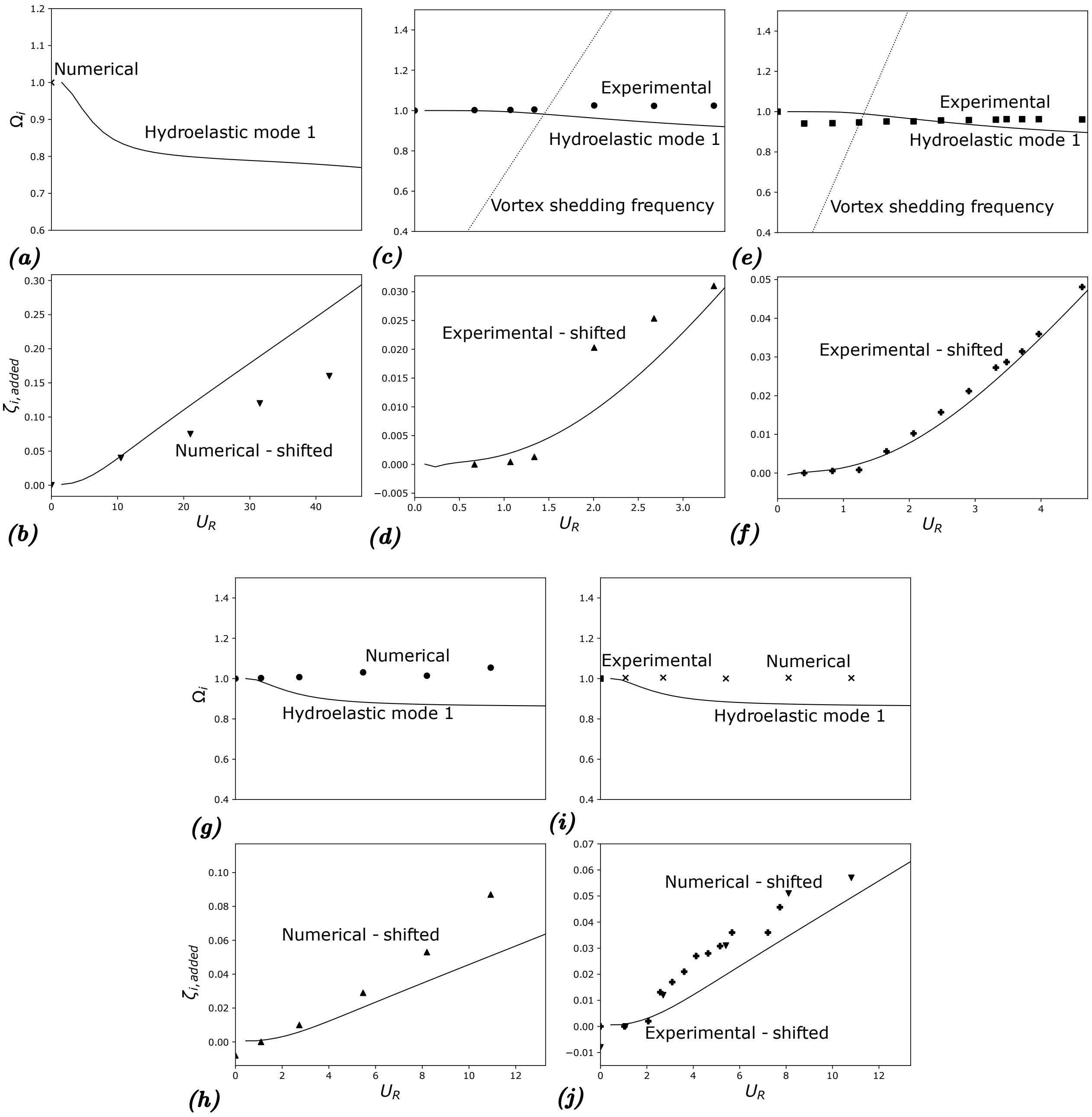

Figure 4.4 Dependence of dimensionless frequency Ω_i and flow-added damping $\zeta_{i,added}$ on the reduced velocity U_R for the first mode of the studied hydrofoils in comparison with the literature: a-b) NACA0003 (Cupr et al., 2018); c-d) F0 (Bergan et al., 2019a); e-f) F1 (Bergan et al., 2019a): g-h) NACA0009 Donaldson (Zeng et al., 2019); i-j) and NACA0009 Blunt (Roth et al., 2009; Zeng et al., 2019). The fundamental frequencies used for the dimensionless frequencies Ω_i are found in Table 4.2. Experimental and numerical results for the first bending mode, presented as data points, are compared with hydroelastic results, presented as continuous lines. The experimental and numerical added damping results are shifted to account for structural damping. For the F0 and F1 hydrofoils, an estimated vortex shedding frequency is plotted as observed from experimental results (Bergan et al., 2019a).

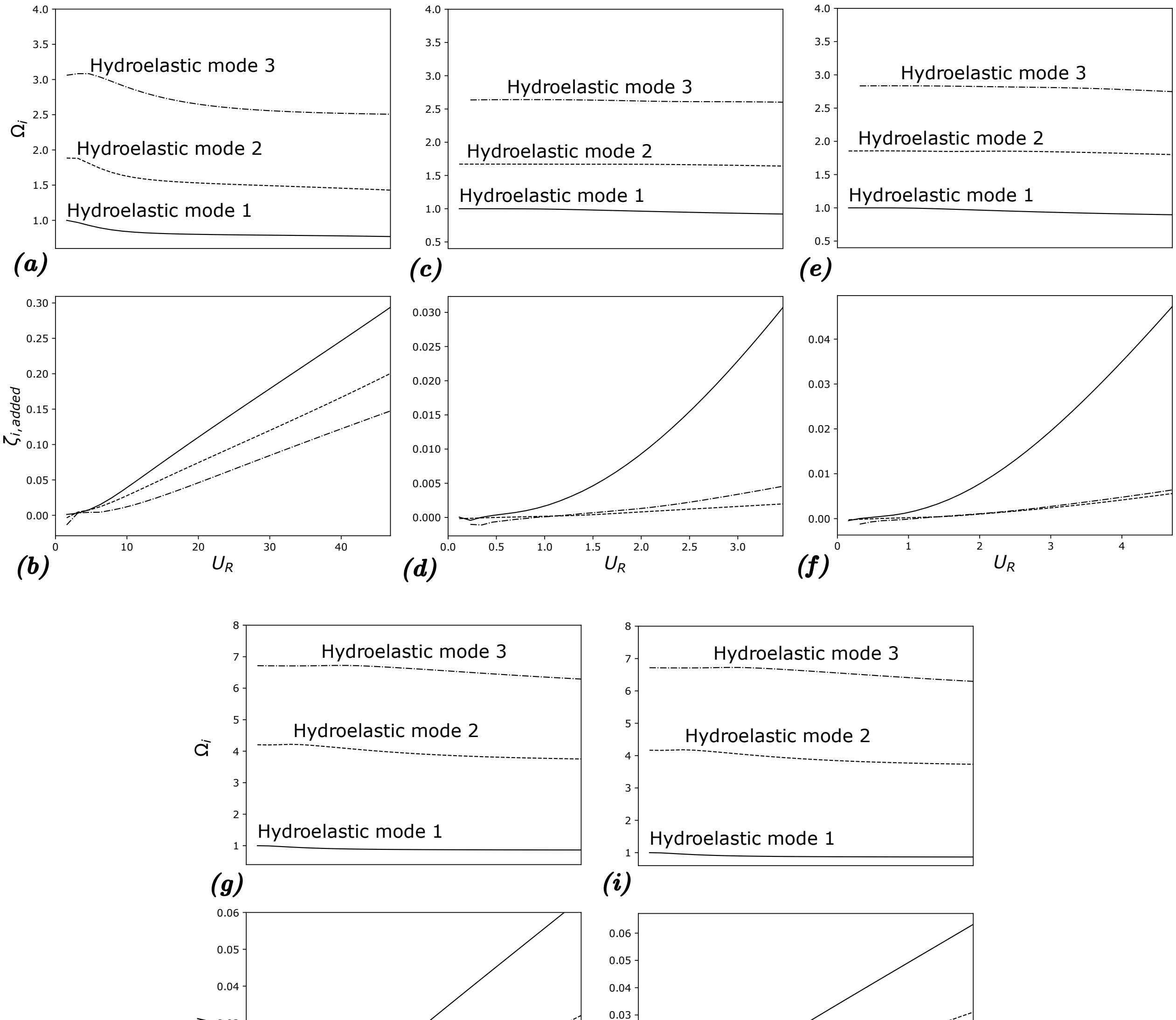

Figure 4.5 Dependence of the dimensionless frequency Ω_i and flow-added damping $\zeta_{i,added}$ with the reduced velocity U_R for the first 3 modes of the studied hydrofoils: a-b) NACA0003; c-d) F0; e-f) F1; g-h) NACA0009 Donaldson trailing edge; i-j) and NACA0009 Blunt trailing edge. The fundamental frequencies used for the dimensionless frequencies Ω_i are found in Table 4.2.

4.3 Cascade of hydrofoils

In the previous section, we demonstrated that our method presents good agreement with the literature on simple cases such as straight hydrofoils. We now want to extend the method on a more complex geometry, getting closer to a realistic hydraulic turbine. Therefore, we extend the method to a cascade of hydrofoils.

4.3.1 Physical model

All the assumptions previously made are valid in the case of a cascade except the similarity of the mode shapes in vacuum and in resting fluid. Indeed, the water acts as a coupling agent between the different hydrofoils, therefore they interact with each other, and the mode shapes are very different than in vacuum where they are decoupled. This prevents us from using the AVMI factor as defined before because the added mass matrix is not accurately defined with the previous methodology.

First, we made the assumption that each eigenvector in vacuum $\boldsymbol{\psi_i}$ could be expressed as a linear combination of the eigenvectors in water $\boldsymbol{\phi_i}$

$$\boldsymbol{\psi_i} = \sum_{j=1}^{N} a_{ij} \boldsymbol{\phi_j}, \tag{4.20}$$

which gives in the following matrix formulation

$$[\Psi] = [\Phi][A], \tag{4.21}$$

with $[\Psi]$ the matrix of the eigenvectors in vacuum, $[\Phi]$ the matrix of the eigenvectors in water and $[A]$ the matrix of the coefficient linking the two bases.

Our goal is to express the mass matrix with flow-added effect in the modal basis in vacuum, for the aeroelastic analysis. In this case, we need to distinguish in which modal basis the matrices are expressed, either the vacuum one $[M_{hh_{vac},s}]$ or the resting fluid one $[M_{hh_{fluid},s}]$ because they are not equal anymore. We know from the modal analysis in vacuum that $[M_{hh_{vac},s}] = [\Psi]^T[M_s][\Psi]$ and from the modal analysis in resting fluid that $[M_{hh_{fluid},s}] + [M_{hh_{fluid},f}] = [\Phi]^T([M_s] + [M_f])[\Phi]$. Therefore

$$[\Psi]^T([M_s] + [M_f])[\Psi] = [\Psi]^T[\Phi]^{T^{-1}}[\Phi]^{-1}[\Psi]. \tag{4.22}$$

Using Equation 4.21

$$[\Psi]^T([M_s] + [M_f])[\Psi] = [A]^T[\Phi]^T[\Phi]^{T^{-1}}[\Phi]^{-1}[\Phi][A] = [A]^T[A], \tag{4.23}$$

we have

$$[M_{hh_{vac},s}] + [M_{hh_{vac},f}] = [A]^T[A] = [M_{hh_{vac},s}][A]^T[A], \tag{4.24}$$

because $[M_{hh_{vac},s}] = I$.

In the case of a cascade of hydrofoil, the passage matrix $[P]$ previously defined as the ratio of eigenvalues in vacuum and in resting fluid is now defined as $[P] = [A]^T[A]$, with $[A]$ the linear combination matrix linking the two modal basis. However this method was tested in NASTRAN, and the results were not exploitable. This was due to the fact that the P matrix was not diagonal and that the software is not made to accept such matrices.

The second solution to overcome the problem of having different mode shapes in vacuum and in water was to couple artificially the hydrofoils in the vacuum analysis. This was done by adding elastic links with a high value of rigidity at the trailing edge of the different hydrofoils. Those links did not change the frequency of the different modes but they modified the mode shapes making them similar in vacuum and in resting fluid. The AVMI factor can therefore be used in the same manner as in the previous methodology. The elastic links were added in the first modal analysis in vacuum as well as the aeroelastic analysis.

4.3.2 Test case

The test case we use to test the accuracy of the method is the one developed experimentally by (Bergan et al., 2019b). They studied a cascade of 3 F1 hydrofoils spaced by 39 mm. Figure 4.6 represent the mesh used for the vibro-acoustic analysis of the cascade of F1 hydrofoils. Bergan et al. (2019b) studied 4 modes in his experimental works, that he refers to as M1, M2, M3 and M4. Those mode are not sorted by increasing natural frequency but rather by their mode shapes. In the following discussion, we will refer to those mode the same way Bergan et al. (2019b) did to avoid confusion, even though with our method the mode are initially sorted by increasing natural frequency.

Figure 4.7 presents the first four mode shapes in vacuum and in the fluid for the cascade of hydrofoils. We can see that the mode shapes are not similar at all. Figure 4.8 represent the mode shapes in vacuum with the elastic links. We can clearly see that the mode shapes are now closer than the ones in resting fluid but in order to evaluate the similarity correctly, we use the MAC number, similarly to the previous cases. This proves that the assumption of similar mode shapes required by the use of AVMI factor is valid here. For M1, M4 and M5,

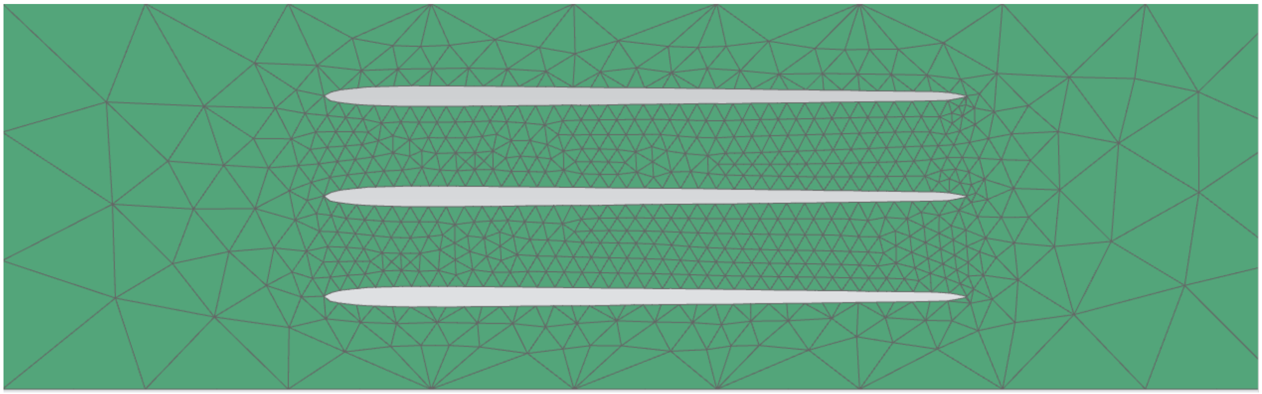

Figure 4.6 Zoom of a transverse cut of the acoustic fluid mesh of the cascade of hydrofoils

the MAC is around 90% similarly, 66 % for M3 and 46 % for M2 as shown in Table 4.5. The natural frequencies that we found in water are similar to the experimental results found by Bergan et al. (2019b) as shown in Table 4.5.

Table 4.5 Modal frequencies in vacuum and resting fluid with fine meshes and from the literature (Bergan et al., 2019b) and MAC for the first 5 modes.

Mode number	Source	$f_{1,vac}$ [Hz]	$f_{1,fr}$ [Hz]	MAC with elastic links
Mode 1	Finer mesh	1131	237.4	0.842
	Experimental reference (Bergan et al., 2019b)		252.0	
Mode 2	Finer mesh	1720	472.8	0.455
	Experimental reference (Bergan et al., 2019b)		491.0	
Mode 3	Finer mesh	1720	701.0	0.66
	Experimental reference (Bergan et al., 2019b)		708.2	
Mode 4	Finer mesh	1131	283.4	0.894
	Experimental reference (Bergan et al., 2019b)		300.1	
Mode 5	Finer mesh	1131	390.0	0.920

Now that the first two modal analysis have been made, the AVMI factor can be computed and the aeroelastic analysis can be performed. Bergan et al. (2019b) evaluated the flow-added damping for M1, M2, M3 and M4. However, we think that a mistake was made in the definition of M2 in the paper of Bergan et al. (2019b). Indeed, the flow-added damping given by our method for M2 is much smaller than the one presented by Bergan et al. (2019b), while the results of our method for M5 are in well agreement with the experimental results. Those two modes have close natural frequencies, so we think a confusion was made between those two modes. Therefore, we now referred as M2 the last mode presented in the Table 4.5.

Figure 4.9 represent the comparison between the experimental results in scatter points and our results in continuous lines. The vertical gray lines are the uncertainties of the experimen-

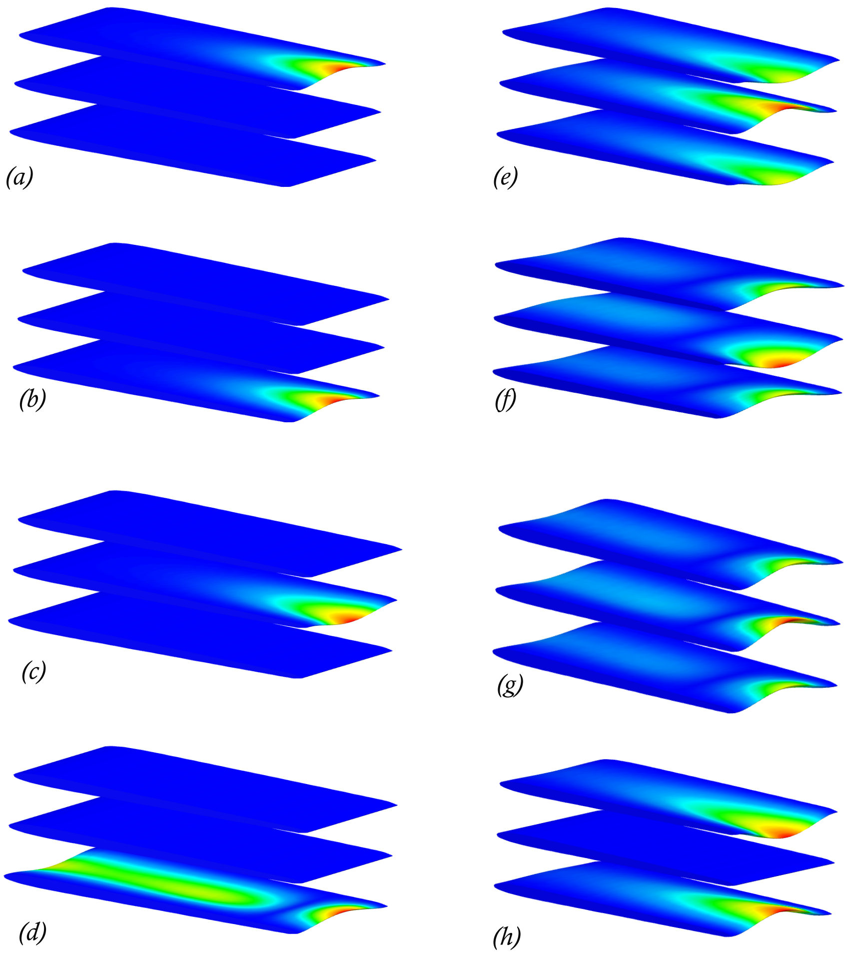

Figure 4.7 Mode shapes of the cascade of hydrofoils in vacuum and resting fluid: Mode 1 in a) vacuum, e) resting fluid; Mode 2 in b) vacuum, f) resting fluid; Mode 3 in c) vacuum, g) resting fluid; Mode 4 in d) vacuum, h) resting fluid.

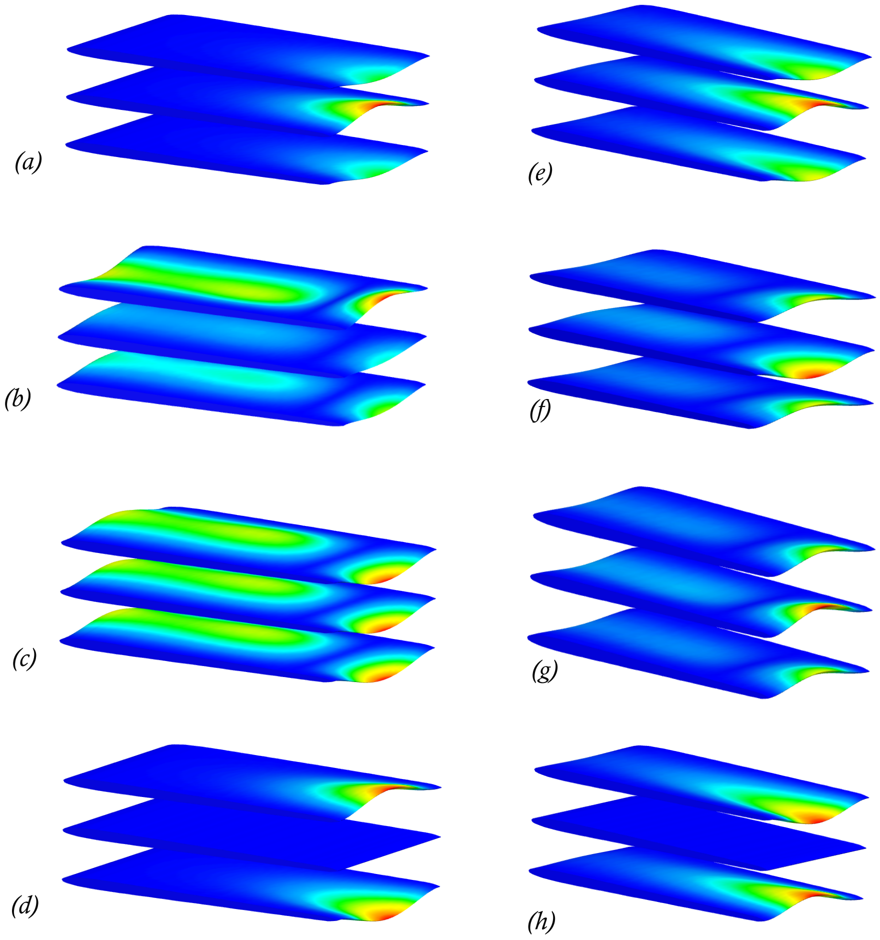

Figure 4.8 Mode shapes of the cascade of hydrofoils in vacuum with elastic links and resting fluid: Mode 1 in a) vacuum, e) resting fluid; Mode 2 in b) vacuum, f) resting fluid; Mode 3 in c) vacuum, g) resting fluid; Mode 4 in d) vacuum, h) resting fluid.

tal results. The flow-added damping is plotted against the reduced velocity. As mentioned before for the previous cases, our model does not include any structural damping, we therefore shift the experimental results with the structural damping, being the damping at zero velocity. We can see very good agreement between the experimental results and our method, especially for the M1, M2 and M4. We observe once again two regimes of the evolution of the flow-added damping: before lock-in at low reduced velocity where the damping is almost constant and null, and after lock-in where the flow-added damping increase linearly with the reduced velocity.

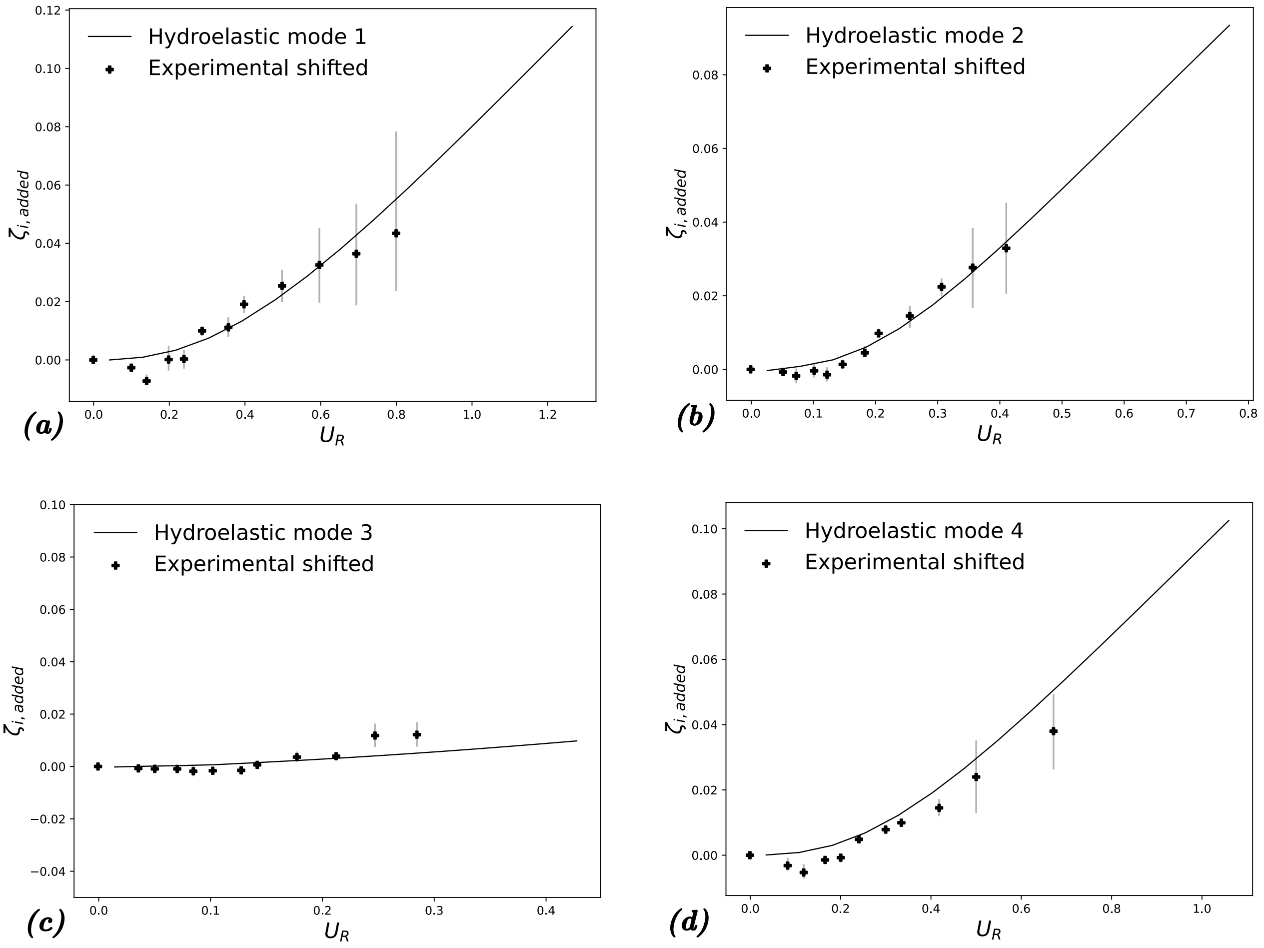

Figure 4.9 Dependence of flow-added damping $\zeta_{i,added}$ on the reduced velocity U_R for the four modes of the studied cascade of hydrofoils in comparison with the literature (Bergan et al., 2019b): a) Mode 1; b) Mode 2; c) Mode 3 and d) Mode 4. Experimental and results presented as data points, are compared with hydroelastic results, presented as continuous lines. The experimental added damping results are shifted to account for structural damping.

For the M3 case on Figure 4.9c, our results underestimate the flow-added damping. However, the values are much lower for this modes compared to the other modes both for the experimental results and ours. This is because M3 correspond to a higher mode, the 6th mode predicted by our model. This mode contains less energy compared to the first 3 modes which all have a much smaller natural frequency. The computation time for the cascade of hydrofoil was of 22 minutes on my personal laptop.

4.4 Conclusion and limitations of the method

We have shown in this chapter, that a panel method based on the potential flow theory enforcing the Kutta condition could evaluate accurately the flow-added damping in the case of several single straight hydrofoils and a cascade of straight hydrofoils. The aeroelastic flutter analysis method from NASTRAN accurately predicted flow-added damping across various hydrofoil profiles, trailing edge shapes, boundary conditions, and material properties, aligning well with other numerical and experimental results in the literature. The computation time is much lower than in traditional method where those results take around 90 hours to converge. This method is as a fast way to evaluate the flow-added damping on simple geometries.

However, the goal of this project is to be able to apply a fast method like this one to a very complex geometry such as a hydraulic turbine runner. We found that it will be difficult for the NASTRAN software to capture rotational effects because the aerodynamic panels must be straight. We also found that the confinement would be difficult to model in NASTRAN as well as complex geometries with camber hydrofoils for example. Those limitations lead us to develop another method with the same objectives, but with the confidence that the newly developed method can be extended to complex geometries. A finite-element model is therefore developed in the following chapter.

CHAPTER 5 FINITE-ELEMENT METHOD

In this chapter, we develop a numerical method to determine the flow-added damping and the stability of a flexible structure subject to a dense fluid flow. Couture (2020) developed two methods similar to ours in his work. One method with a potential flow model of the fluid and another one where the fluid is considered viscous and follows the linearized Navier-Stokes equations. The method developed here is a continuation of Couture (2020) 's work. It can be interpreted as a hybridization of Couture (2020)'s two methods. Couture (2020) shows in his work that a potential flow model cannot determine correctly the dynamics of a flexible structure because of the lack of viscosity. Indeed, fluctuating circulation in the wake cannot be modeled without viscous effects (Cisonni et al., 2017). Couture (2020) also shows that a model where the fluid is considered viscous had also limitations, like the disappearance of the destabilizing term induced by the flow on the structure. Here, we use a similar formulation of his work and develop a hybrid version of his two methods. The base flow is still considered potential in order to have a destabilizing term in the kinematic boundary condition at the fluid-structure interface. The perturbation flow is considered viscous, in order to implicitly model the wake accurately because the fluctuating circulation in the wake has a paramount effect on the stability of the structure. This hybrid method was previously considered by Gosselin (2006) on a different geometry but with a similar conceptual approach.

The method developed here is based on the small perturbation hypothesis for the solid displacement, the pressure, and the fluid velocity. We combine a linear elastic solid domain with a hybrid model for the fluid domain, the base flow being inviscid and the perturbation flow is viscous.

We study the stability of a cantilever plate in axial flow. This test case will allow us to compare the accuracy of our results with the paper from Guo and Païdoussis (2000) and Howell et al. (2009).

5.1 Physical model

5.1.1 Structural equation

The linear elastic theory with an isotropic material is used to describe the structure with $\boldsymbol{W}$ the solid displacement vector

$$\rho_s \frac{\partial^2 \boldsymbol{W}}{\partial t^2} = \nabla \cdot \boldsymbol{\sigma}(\boldsymbol{W}) + \boldsymbol{F}, \tag{5.1}$$

where ρ_s is the density, $\boldsymbol{\sigma}(\boldsymbol{W})$ the Cauchy stress tensor and $\boldsymbol{F}$ the external volumetric force. Equation 5.1 is defined on the solid domain Ω_s.

5.1.2 Navier-Stokes equations

The Navier-Stokes momentum equation with $\boldsymbol{U_f}$ the fluid velocity vector and P the pressure is

$$\rho_f \left(\frac{\partial \boldsymbol{U}_f}{\partial t} + (\boldsymbol{U_f} \cdot \boldsymbol{\nabla}) \boldsymbol{U_f} \right) = -\boldsymbol{\nabla} P + \nabla \cdot \boldsymbol{\tau_f}(\boldsymbol{U_f}), \tag{5.2}$$

where ρ_f is the fluid density and $\boldsymbol{\tau_f}(\boldsymbol{U_f})$ is the viscosity tensor defined as

$$\boldsymbol{\tau_f}(\boldsymbol{U_f}) = \eta \left(\boldsymbol{\nabla} \boldsymbol{U_f} + \boldsymbol{\nabla} \boldsymbol{U_f^T} \right), \tag{5.3}$$

where η is the viscosity.

Remark: because the flow field $\boldsymbol{U_f}$ will be defined as the sum of an inviscid base flow and a viscous base flow, the viscosity tensor $\boldsymbol{\tau_f}(\boldsymbol{U_f})$ will be null for the base flow. It will only appear in the first order equation for the viscous perturbation flow.

The continuity equation is

$$\nabla \cdot \boldsymbol{U_f} = 0. \tag{5.4}$$

Equation 5.2 and 5.4 are defined on the fluid domain Ω_f.

5.1.3 Perturbation method

In the case of the small perturbation hypothesis, we define the fluid and the solid variables around a base state. The solid displacement vector $\boldsymbol{W}$, the pressure P and the fluid velocity vector $\boldsymbol{U_f}$ are defined as follow

$$\boldsymbol{W} = \boldsymbol{w_b} + \boldsymbol{w}, \tag{5.5}$$

$$P = p_b + p, \tag{5.6}$$

$$\boldsymbol{U_f} = \boldsymbol{u_{f,b}} + \boldsymbol{u_f}, \tag{5.7}$$

with $\boldsymbol{w_b}$ the base solid displacement vector, p_b the base pressure, $\boldsymbol{u_{f,b}}$ the base fluid velocity vector, $\boldsymbol{w}$ the perturbation solid displacement vector, p the perturbation pressure and $\boldsymbol{u_f}$ the perturbation fluid velocity vector.

The perturbation variable are one order lower than the base state variables. They are by definition of order 1.

Using the decomposition of Equation 5.5, without external forces we have for the following structural equation

$$\rho_s \frac{\partial^2(\boldsymbol{w_b}+\boldsymbol{w})}{\partial t^2} = \nabla \cdot \boldsymbol{\sigma}(\boldsymbol{w_b}+\boldsymbol{w}). \tag{5.8}$$

We then have the 0th-order and 1st-order equations

$$\nabla \cdot \boldsymbol{\sigma}(\boldsymbol{w_b}) = 0, \tag{5.9}$$

$$\rho_s \frac{\partial^2 \boldsymbol{w}}{\partial t^2} = \nabla \cdot \boldsymbol{\sigma}(\boldsymbol{w}). \tag{5.10}$$

We now assume that the base displacement vector $\boldsymbol{w_b} = 0$, the 0th-order equation is therefore null. The small perturbation solid displacement $\boldsymbol{w}$ is defined with a Lagrangian field specification.

Hooke's law allows us to write the Cauchy stress tensor as

$$\boldsymbol{\sigma}(\boldsymbol{w}) = 2\mu\boldsymbol{\epsilon}(\boldsymbol{w}) + \lambda tr[\boldsymbol{\epsilon}(\boldsymbol{w})]\boldsymbol{I}, \tag{5.11}$$

with $\boldsymbol{\epsilon}(\boldsymbol{w})$ the infinitesimal strain tensor, λ and μ being the first and second Lamé coefficients defined as

$$\lambda = \frac{E\nu_s}{(1+\nu_s)(1-2\nu_s)}, \ \mu = \frac{E}{2(1+\nu_s)}, \tag{5.12}$$

with E the Young's modulus and ν_s the Poisson coefficient. The infinitesimal strain tensor is

$$\boldsymbol{\epsilon}(\boldsymbol{w}) = \frac{1}{2}(\boldsymbol{\nabla}\boldsymbol{w} + \boldsymbol{\nabla}\boldsymbol{w}^T). \tag{5.13}$$

Using the decomposition of Equation 5.7 and Equation 5.6 in Equation 5.2 gives the 1st-order following equation for the fluid equation

$$\rho_f \left(\frac{\partial \boldsymbol{u_f}}{\partial t} + (\boldsymbol{u_{f,b}} \cdot \boldsymbol{\nabla})\boldsymbol{u_f} + (\boldsymbol{u_f} \cdot \boldsymbol{\nabla})\boldsymbol{u_{f,b}} \right) = -\boldsymbol{\nabla} p + \nabla \cdot \boldsymbol{\tau_f}(\boldsymbol{u_f}). \tag{5.14}$$

The 1st-order continuity equation is

$$\nabla \cdot \boldsymbol{u_f} = 0. \tag{5.15}$$

5.1.4 Base flow solutions

Equation 5.14 is the 1st-order equation for the fluid perturbation variables. This equation corresponds to the linearized Navier-Stokes equations with viscosity. The inviscid model was shown to accurately predict the stability of the flexible cantilever with clamped-clamped boundary conditions (Couture, 2020). In order to make the model more complete, we add viscosity in the model, but only in the small perturbation flow. It makes the model non-consistant, the base flow and the perturbation flow have different models and boundary conditions, but it includes more physics than the purely inviscid model, i.e., it includes the perturbation circulation. Therefore, we choose to introduce viscous effects in our perturbation flow in order to model accurately the fluctuating circulation in the wake which has an important effect on the stability of the structure. However, similarly to Gosselin (2006), we use an inviscid flow for the base flow of our formulation. This is because having a free-slip boundary condition at the interface allows the destabilizing effect of the flow to be seen in the kinematic boundary condition at the interface. This effect will not be taken into account with a no-slip boundary condition in our formulation. A more complex treatment of the boundary condition will be needed, with the determination of the instantaneous deformed position of the structure (Gosselin, 2006).

We therefore make the strong assumption that our flow field is hybrid and derive the relevant equations based on this assumption. Initial verification presented in this thesis shows promising results, but further validation is needed to fully substantiate the model.

We tested two different inviscid solutions for the base flow: a potential base flow respecting the no-penetration at the fluid-structure interface and a simple plug flow. Both solutions are presented here but only the plug flow formulation will be used for the rest of the equations for simplicity.

Plug flow

We assume that the base flow here is a simple plug flow such that

$$\boldsymbol{u_{f,b}} = U\boldsymbol{e_x}, \tag{5.16}$$

with U the base flow velocity value. Using this decomposition in Equation 5.14 gives the 1st-order following equation

$$\rho_f\left(\frac{\partial \boldsymbol{u_f}}{\partial t} + U\frac{\partial \boldsymbol{u_f}}{\partial x}\right) = -\boldsymbol{\nabla} p + \nabla \cdot \boldsymbol{\tau_f}(\boldsymbol{u_f}). \tag{5.17}$$

Potential base flow

In order to be more consistent with a realistic flow field, we introduce the no-penetration condition in the base flow. The base flow can be written as

$$\boldsymbol{u_{f,b}} = U_x(x,y)\boldsymbol{e_x} + U_y(x,y)\boldsymbol{e_y}. \tag{5.18}$$

This adds a term in the Navier-Stokes momentum equation such that Equation 5.14 is rewritten as

$$\rho_f \left(\frac{\partial \boldsymbol{u_f}}{\partial t} + U_x \frac{\partial \boldsymbol{u_f}}{\partial x} + U_y \frac{\partial \boldsymbol{u_f}}{\partial y} + \boldsymbol{u_f} \cdot \boldsymbol{\nabla} \boldsymbol{u_{f,b}} \right) = -\boldsymbol{\nabla} p + \nabla \cdot \boldsymbol{\tau_f}(\boldsymbol{u_f}). \tag{5.19}$$

In order to determine $U_x(x,y)$ and $U_y(x,y)$, we solve the potential theory for the base flow. From the potential flow theory, we seek a velocity potential ϕ_b such that

$$\boldsymbol{u_{f,b}} = \boldsymbol{\nabla} \phi_b. \tag{5.20}$$

Introducing this decomposition into the continuity equation of the base flow Equation 5.4, we have

$$\Delta \phi_b = 0. \tag{5.21}$$

The boundary conditions of the base flow are the no-penetration condition on the walls and at the interface with the structure. On the inlet, the base flow is a plug flow of velocity U and a null velocity potential is imposed on the outlet, similarly to what Couture (2020) did.

Because our method is a finite-element method, the weak formulation is developed. We define a Sobolev space for the velocity potential ϕ_b and a test function ψ_b as follow

$$\phi_b,\, \psi_b \in \mathcal{V}_f = \{\boldsymbol{\phi} : \Omega_f \to \mathbb{R} \;|\boldsymbol{\phi} \in \mathcal{H}^1(\Omega_f), \boldsymbol{\phi} = 0 \text{ on } \Gamma_f^D\}. \tag{5.22}$$

We multiply Equation 5.21 by ψ_b and integrate over the fluid domain

$$\int_{\Omega_f} \Delta \phi_b \psi_b \, dV = 0. \tag{5.23}$$

The first Green identity for two scalar fields ϕ and ψ is

$$\int_\Omega \Delta\phi\psi \, dV = \oint_{\Gamma_f} \boldsymbol{\nabla}\phi \cdot \boldsymbol{n} \, \psi \, dS - \int_\Omega \boldsymbol{\nabla}\phi \cdot \boldsymbol{\nabla}\psi \, dV. \tag{5.24}$$

Using this identity, Equation 5.23 becomes

$$\int_{\Omega_f} \boldsymbol{\nabla}\phi_b \cdot \boldsymbol{\nabla}\psi_b \, dV + \int_{\Gamma_i} U\psi dS = 0. \tag{5.25}$$

The base flow is then obtained solving this equation with our finite-element method.

5.1.5 Fluid-structure boundary conditions

The solid equation being expressed in a Lagrangian framework compared to the Eulerian framework for the Navier-Stokes equations, the coupling equations are important to ensure consistency. Coupling both frameworks usually requires an ALE formulation, but the small perturbation hypothesis allows us to keep both definitions here (Couture, 2020).

The no-penetration at the fluid-structure interface is defined via a kinematic boundary condition, and the continuity of the stress tensors is defined with a dynamic boundary condition.

Kinematic boundary condition

We equalize the fluid velocity and the time-derivative of the displacement vector at the interface. Because of the two frameworks of the solid and fluid domains, we use a material derivative for the solid displacement

$$\boldsymbol{u_f} = \frac{D\boldsymbol{w}}{Dt} = \frac{\partial \boldsymbol{w}}{\partial t} + \boldsymbol{u_{f,b}} \cdot \boldsymbol{\nabla w} + \boldsymbol{u_f} \cdot \boldsymbol{\nabla w}. \tag{5.26}$$

The perturbation variables are of order 1, there they can be defined using a small factor ϵ as follow

$$\boldsymbol{w} = \epsilon \boldsymbol{w}^*, \tag{5.27}$$

$$p = \epsilon p^*, \tag{5.28}$$

$$\boldsymbol{u_f} = \epsilon \boldsymbol{u_f}^*. \tag{5.29}$$

Using this decomposition Equation 5.30 becomes

$$\epsilon \boldsymbol{u_f^*} = \epsilon \frac{\partial \boldsymbol{w}^*}{\partial t} + \epsilon \boldsymbol{u_{f,b}} \cdot \boldsymbol{\nabla} \boldsymbol{w}^* + \epsilon^2 \boldsymbol{u_f^*} \cdot \boldsymbol{\nabla} \boldsymbol{w}^*. \tag{5.30}$$

Using the definition of the base flow in Equation 5.16, it becomes

$$\epsilon \boldsymbol{u_f^*} = \epsilon \frac{\partial \boldsymbol{w}^*}{\partial t} + \epsilon U \frac{\partial \boldsymbol{w}^*}{\partial x} + \epsilon^2 \boldsymbol{u_f^*} \cdot \boldsymbol{\nabla} \boldsymbol{w}^*. \tag{5.31}$$

The 1st-order equation at the fluid structure interface is

$$\boldsymbol{u_f} = \frac{\partial \boldsymbol{w}}{\partial t} + U \frac{\partial \boldsymbol{w}}{\partial x}. \tag{5.32}$$

The term $\boldsymbol{u_f} \cdot \boldsymbol{\nabla} \boldsymbol{w} = \epsilon^2 \boldsymbol{u_f^*} \cdot \boldsymbol{\nabla} \boldsymbol{w}^*$ is neglected because it is of order 2.

In Equation 5.32, the first term $\partial \boldsymbol{w}/\partial t$ corresponds to the velocity of the structure and the second term $U\partial \boldsymbol{w}/\partial x$ corresponds to the slope of the structure. The second one is the destabilizing term induced by the flow on the structure and would be null if the base flow had a no-slip boundary condition at the interface ($\boldsymbol{u_{f,b}} = 0$ at the interface in that case).

Remark:

In the trivial case where the solid displacement is zero, meaning $\boldsymbol{w} = 0$, the perturbation flow variable at the interface would also be zero: $\boldsymbol{u_f} = 0$, due to the no-slip boundary condition. Consequently, at the interface, we would have $\boldsymbol{U_f} = U\boldsymbol{e_x}$. This is the sum of the base flow $\boldsymbol{u_{f,b}} = U\boldsymbol{e_x}$ and the perturbation $\boldsymbol{u_f} = 0$.

In this hybrid model, the base flow at the interface has a free-slip boundary condition, while the perturbation flow adheres to a no-slip boundary condition. However, the boundary condition for the total flow field $\boldsymbol{U_f}$ remains undefined. This ambiguity represents a limitation of the hybrid domain, reducing its physical realism.

Dynamic boundary condition

The dynamic boundary condition is obtained by equalizing the fluid stress tensor $\boldsymbol{\sigma_f}$ and the solid stress tensors $\boldsymbol{\sigma}$ at the fluid-structure interface

$$\boldsymbol{\sigma_f}(\boldsymbol{U_f}, P) = \boldsymbol{\sigma}(\boldsymbol{W}). \tag{5.33}$$

The 1st-order equation is therefore

$$\boldsymbol{\sigma_f}(\boldsymbol{u_f}, p) = \boldsymbol{\sigma}(\boldsymbol{w}), \tag{5.34}$$

with

$$\boldsymbol{\sigma_f}(\boldsymbol{u_f}, p) = -p\boldsymbol{I} + \boldsymbol{\tau_f}(\boldsymbol{u_f}). \tag{5.35}$$

Equation 5.32 and 5.34 are defined on the fluid-structure interface Γ_{fs}.

Combining Equations 5.10, 5.17, 5.15, 5.32 and 5.34 gives the following problem

$$\begin{cases} \rho_f \left(\dfrac{\partial \boldsymbol{u_f}}{\partial t} + U \dfrac{\partial \boldsymbol{u_f}}{\partial x} \right) = -\boldsymbol{\nabla} p + \nabla \boldsymbol{\tau_f}(\boldsymbol{u_f}) \ \text{ on } \ \Omega_f \\ \\ \nabla \cdot \boldsymbol{u_f} = 0 \ \text{ on } \ \Omega_f \\ \\ \rho_s \dfrac{\partial^2 \boldsymbol{w}}{\partial t^2} = \nabla \boldsymbol{\sigma} \ \text{ on } \ \Omega_s \\ \\ \boldsymbol{\sigma_f}(\boldsymbol{u_f}, p) = \boldsymbol{\sigma}(\boldsymbol{w}) \ \text{ on } \ \Gamma_{fs} \\ \\ \boldsymbol{u_f} = \dfrac{\partial \boldsymbol{w}}{\partial t} + U \dfrac{\partial \boldsymbol{w}}{\partial x} \ \text{ on } \ \Gamma_{fs} \end{cases} \tag{5.36}$$

Rather than solving these equations in the time domain, which would be very computationally expensive, we solve them in the frequency domain using harmonic forms for the small perturbation variables. We then obtain an eigenvalue problem which will allow us to extract the eigenvectors, their frequency and their damping. The modal decomposition of the small perturbation variables is as follow

$$\boldsymbol{w} = \hat{\boldsymbol{w}} e^{i\omega t}, \tag{5.37}$$

$$p = \hat{p} e^{i\omega t}, \tag{5.38}$$

$$\boldsymbol{u_f} = \hat{\boldsymbol{u_f}} e^{i\omega t}, \tag{5.39}$$

with $\hat{\boldsymbol{w}}$, $\hat{p}$ and $\hat{\boldsymbol{u_f}}$ the waveform of the modes and ω the complex eigenvalue. For readability the hat symbol is abandoned in the following equations. With the modal decomposition, Problem 5.36 becomes

$$\begin{cases} \rho_f \left(i\omega\, \boldsymbol{u_f} + U \dfrac{\partial \boldsymbol{u_f}}{\partial x} \right) = -\boldsymbol{\nabla} p + \nabla \boldsymbol{\tau_f}(\boldsymbol{u_f}) \;\; \text{on} \;\; \Omega_f \\[2ex] \nabla \cdot \boldsymbol{u_f} = 0 \;\; \text{on} \;\; \Omega_f \\[2ex] -\omega^2 \rho_s\, \boldsymbol{w} = \nabla \boldsymbol{\sigma} \;\; \text{on} \;\; \Omega_s \\[2ex] \boldsymbol{\sigma_f}(\boldsymbol{u_f}, p) = \boldsymbol{\sigma}\boldsymbol{(}\boldsymbol{w}\boldsymbol{)} \;\; \text{on} \;\; \Gamma_{fs} \\[2ex] \boldsymbol{u_f} = i\omega\, \boldsymbol{w} + U \dfrac{\partial \boldsymbol{w}}{\partial x} \;\; \text{on} \;\; \Gamma_{fs} \end{cases} \tag{5.40}$$

.

This eigenvalue problem is quadratic because of the second-order time derivative of the solid displacement in the structure's equation. Solving a quadratic eigenvalue problem can be challenging. We therefore define a small perturbation displacement velocity $\boldsymbol{u_s}$ like Couture (2020).

$$\boldsymbol{u}_s = \frac{\partial \boldsymbol{w}}{\partial t}. \tag{5.41}$$

Problem 5.40 can be rewritten as

$$\begin{cases} \rho_f \left(i\omega\, \boldsymbol{u_f} + U \dfrac{\partial \boldsymbol{u_f}}{\partial x} \right) = -\boldsymbol{\nabla} p + \nabla \boldsymbol{\tau_f}(\boldsymbol{u_f}) \;\; \text{on} \;\; \Omega_f \\[2ex] \nabla \cdot \boldsymbol{u_f} = 0 \;\; \text{on} \;\; \Omega_f \\[2ex] i\omega \rho_s\, \boldsymbol{u_s} = \nabla \boldsymbol{\sigma} \;\; \text{on} \;\; \Omega_s \\[2ex] i\omega\, \boldsymbol{w} = \boldsymbol{u_s} \;\; \text{on} \;\; \Omega_s \\[2ex] \boldsymbol{\sigma_f}(\boldsymbol{u_f}, p) = \boldsymbol{\sigma}(\boldsymbol{w}) \;\; \text{on} \;\; \Gamma_{fs} \\[2ex] \boldsymbol{u_f} = i\omega\, \boldsymbol{w} + U \dfrac{\partial \boldsymbol{w}}{\partial x} \;\; \text{on} \;\; \Gamma_{fs} \end{cases} \tag{5.42}$$

Problem 5.42 is then solved using a finite-element formulation with a weak formulation defined in the next section.

5.1.6 Weak formulation

Sobolev Space

In order to implement the method with finite elements we need to define different Sobolev Spaces. The solid displacement $\boldsymbol{w}$ and velocity $\boldsymbol{u_s}$ are defined on the same one

$$\boldsymbol{w}, \boldsymbol{u_s} \in \mathcal{U}_s = \{\boldsymbol{w} : \Omega_s \rightarrow \mathbb{R}^2 \ |\boldsymbol{w} \in \mathcal{H}^1(\Omega_s), \boldsymbol{w} = 0 \text{ on } \Gamma_s^D\} \tag{5.43}$$

The fluid velocity $\boldsymbol{u_f}$ and pressure field p are defined on similar Sobolev spaces

$$\boldsymbol{u_f} \in \mathcal{U}_f = \{\boldsymbol{u_f} : \Omega_f \rightarrow \mathbb{R}^2 \ |\boldsymbol{u_f} \in \mathcal{H}^1(\Omega_f), \boldsymbol{u_f} = 0 \text{ on } \Gamma_f^D\} \tag{5.44}$$

$$p \in \mathcal{P}_f = \{\boldsymbol{p} : \Omega_f \rightarrow \mathbb{R} \ |\boldsymbol{p} \in \mathcal{H}^1(\Omega_f), \boldsymbol{p} = 0 \text{ on } \Gamma_f^D\} \tag{5.45}$$

Lagrangian Multiplier

Besides the typical fluid fields, we introduce a Lagrangian multiplier to express the weak formulation of the kinematic boundary condition. This multiplier also helps to weakly impose the dynamic boundary condition at the interface between the fluid and the structure (Couture, 2020). We have

$$\boldsymbol{\lambda_f} = \boldsymbol{\sigma_f}(\boldsymbol{u_f}, p) \cdot \boldsymbol{n_f}, \tag{5.46}$$

with $\boldsymbol{n_f}$ the normal vector at the interface defined from the fluid domain to the solid domain. The corresponding Sobolev space is defined on the interface as follow

$$\boldsymbol{\lambda_f} \in \mathcal{L}_f = \{\boldsymbol{\lambda_f} : \Gamma_{fs} \rightarrow \mathbb{R}^2 \ |\boldsymbol{\lambda_f} \in \mathcal{H}^1(\Gamma_{fs})\}. \tag{5.47}$$

The weak formulation of Problem 5.42 is obtained by multiplying each equation by its associate test function and integrate over the corresponding domain.

Navier-Stokes momentum equation

We define the test function $\boldsymbol{v_f} \in \mathcal{U}_f$. We multiply the Navier-Stokes momentum equation by $\boldsymbol{v_f}$ and integrate over the fluid domain

$$\int_{\Omega_f} \rho_f (i\omega\, \boldsymbol{u_f} \cdot \boldsymbol{v_f} + U \frac{\partial \boldsymbol{u_f}}{\partial x} \cdot \boldsymbol{v_f}) + \boldsymbol{\nabla} p \cdot \boldsymbol{v_f} - \nabla \boldsymbol{\tau_f}(\boldsymbol{u_f}) \cdot \boldsymbol{v_f} dV = 0, \tag{5.48}$$

$$i\omega\rho_f \int_{\Omega_f} \boldsymbol{u_f}\cdot\boldsymbol{v_f} dV + \rho_f \int_{\Omega_f} U\frac{\partial \boldsymbol{u_f}}{\partial x}\cdot\boldsymbol{v_f} dV + \int_{\Omega_f} \boldsymbol{\nabla} p\cdot\boldsymbol{v_f} dV - \int_{\Omega_f} \nabla\boldsymbol{\tau_f}(\boldsymbol{u_f})\cdot\boldsymbol{v_f} dV = 0. \tag{5.49}$$

The first Green identity for a vector field $\boldsymbol{F}$ and a scalar ϕ is

$$\int_{\Omega} \boldsymbol{\nabla}\phi\cdot\boldsymbol{F}\, dV = \oint_{\Gamma_{fs}} \boldsymbol{F}\cdot\boldsymbol{n}\,\phi\, dS - \int_{\Omega} \nabla\cdot\boldsymbol{F}\,\phi\, dV. \tag{5.50}$$

The first Green identity applied to a tensor field $\boldsymbol{T}$ and a vector $\boldsymbol{v}$ is

$$\int_{\Omega} \nabla\cdot\boldsymbol{T}\ \cdot\boldsymbol{v}\, dV = \oint_{\Gamma_{fs}} \boldsymbol{T}\cdot\boldsymbol{n}\ \cdot\boldsymbol{v}\, dS - \int_{\Omega} \boldsymbol{T} : \boldsymbol{\nabla v}\, dV. \tag{5.51}$$

Applying Equation 5.50 with the vector field $\boldsymbol{v_f}$ and the scalar p we have

$$\int_{\Omega_f} \boldsymbol{\nabla} p\cdot\boldsymbol{v_f} dV = -\int_{\Omega_f} p\nabla\cdot\boldsymbol{v_f} dV + \int_{\Gamma_{fs}} p\,\boldsymbol{n_f}\cdot\boldsymbol{v_f} dS. \tag{5.52}$$

Applying Equation 5.51 with the tensor field $\boldsymbol{\tau_f}(\boldsymbol{u_f})$ and the vector field $\boldsymbol{v_f}$ we have

$$\int_{\Omega_f} \nabla\cdot\boldsymbol{\tau_f}(\boldsymbol{u_f})\cdot\boldsymbol{v_f} dV = -\int_{\Omega_f} \boldsymbol{\tau_f}(\boldsymbol{u_f}) : \boldsymbol{\nabla v_f} dV + \int_{\Gamma_{fs}} \boldsymbol{\tau_f}(\boldsymbol{u_f})\cdot\boldsymbol{n_f}\cdot\boldsymbol{v_f} dS. \tag{5.53}$$

Substituting Equation 5.52 and 5.53 into Equation 5.49, we obtain

$$\begin{aligned} &i\omega\rho_f \int_{\Omega_f} \boldsymbol{u_f}\cdot\boldsymbol{v_f} dV + \rho_f \int_{\Omega_f} U\frac{\partial \boldsymbol{u_f}}{\partial x}\cdot\boldsymbol{v_f} dV - \int_{\Omega_f} p\nabla\cdot\boldsymbol{v_f} dV + \int_{\Omega_f} \boldsymbol{\tau_f}(\boldsymbol{u_f}) : \boldsymbol{\nabla v_f} dV \\ &+ \int_{\Gamma_{fs}} (p\,\boldsymbol{n_f} - \boldsymbol{\tau_f}(\boldsymbol{u_f})\cdot\boldsymbol{n_f})\cdot\boldsymbol{v_f} dS = 0, \end{aligned} \tag{5.54}$$

But

$$p\,\boldsymbol{n_f} - \boldsymbol{\tau_f}(\boldsymbol{u_f})\cdot\boldsymbol{n_f} = -(-p\boldsymbol{I} + \boldsymbol{\tau_f}(\boldsymbol{u_f}))\cdot\boldsymbol{n_f} = -\boldsymbol{\sigma_f}.\boldsymbol{n_f} = -\boldsymbol{\lambda_f}. \tag{5.55}$$

To be able to express the problem in a matrix form, we define the following bi-linear operators

$$A_{f_1}(\boldsymbol{u_f}, \boldsymbol{v_f}) = \rho_f \int_{\Omega_f} \boldsymbol{u_f}\cdot\boldsymbol{v_f} dV, \tag{5.56}$$

$$A_{f_2}(\boldsymbol{u_f}, \boldsymbol{v_f}) = \rho_f \int_{\Omega_f} U\frac{\partial \boldsymbol{u_f}}{\partial x}\cdot\boldsymbol{v_f} dV + \int_{\Omega_f} \boldsymbol{\tau_f}(\boldsymbol{u_f}) : \boldsymbol{\nabla v_f} dV, \tag{5.57}$$

$$A_{f_3}(p, \boldsymbol{v_f}) = \int_{\Omega_f} p\nabla\cdot\boldsymbol{v_f} dV, \tag{5.58}$$

$$A_{f_4}(\boldsymbol{\lambda_f}, \boldsymbol{v_f}) = \int_{\Gamma_{fs}} \boldsymbol{\lambda_f} \cdot \boldsymbol{v_f} dS. \tag{5.59}$$

Equation 5.54 is now simplified as

$$i\omega\, A_{f_1}(\boldsymbol{u_f}, \boldsymbol{v_f}) + A_{f_2}(\boldsymbol{u_f}, \boldsymbol{v_f}) - A_{f_3}(p, \boldsymbol{v_f}) - A_{f_4}(\boldsymbol{\lambda_f}, \boldsymbol{v_f}) = 0. \tag{5.60}$$

Continuity equation

We define $q \in \mathcal{P}_f$. We multiply the Navier-Stokes continuity equation by q and integrate over the fluid domain

$$\int_{\Omega_f} q\, \nabla \cdot \boldsymbol{u_f}\, dV = 0. \tag{5.61}$$

We define the following bi-linear operator

$$A_{f_c}(\boldsymbol{u_f}, q) = \int_{\Omega_f} q\, \nabla \cdot \boldsymbol{u_f}\, dV = 0. \tag{5.62}$$

Structural equation

We define $\boldsymbol{e_s} \in \mathcal{U}_s$. We multiply the solid equation by $\boldsymbol{e_s}$ and integrate over the solid domain

$$i\omega\rho_s \int_{\Omega_s} \boldsymbol{u_s} \cdot \boldsymbol{e_s} dV - \int_{\Omega_s} \nabla\boldsymbol{\sigma} \cdot \boldsymbol{e_s} dV = 0. \tag{5.63}$$

Using the first Green identity of Equation 5.51, Equation 5.63 can be written as

$$\int_{\Omega_s} \nabla\boldsymbol{\sigma} \cdot \boldsymbol{e_s} dV = -\int_{\Omega_s} \boldsymbol{\sigma} : \nabla\boldsymbol{e_s} dV + \int_{\Gamma_{fs}} \boldsymbol{\sigma} \cdot \boldsymbol{n_s} \cdot \boldsymbol{e_s} dS, \tag{5.64}$$

where $\boldsymbol{n_s}$ is the normal vector at the interface defined from the solid domain to the fluid domain. On the fluid-structure interface, the dynamic boundary condition of Equation 5.34 imposes the equality of the fluid stress tensor and solid stress tensor, therefore, on the interface

$$\boldsymbol{\sigma} \cdot \boldsymbol{n_s} = \boldsymbol{\sigma_f} \cdot \boldsymbol{n_s} = -\boldsymbol{\sigma_f} \cdot \boldsymbol{n_f} = -\boldsymbol{\lambda_f}. \tag{5.65}$$

We define the following bi-linear operators

$$A_{s_1}(\boldsymbol{u_s}, \boldsymbol{e_s}) = \rho_s \int_{\Omega_s} \boldsymbol{u_s} \cdot \boldsymbol{e_s} dV, \tag{5.66}$$

$$A_{s_2}(\boldsymbol{w}, \boldsymbol{e_s}) = \int_{\Omega_s} \boldsymbol{\sigma} : \nabla\boldsymbol{e_s} dV, \tag{5.67}$$

$$A_{s_f}(\boldsymbol{\lambda_f}, \boldsymbol{e_s}) = \int_{\Gamma_{fs}} \boldsymbol{\lambda_f} \cdot \boldsymbol{e_s} dS. \tag{5.68}$$

Equation 5.64 is now simplified to

$$i\omega\, A_{s_1}(\boldsymbol{u_s}, \boldsymbol{e_s}) + A_{s_2}(\boldsymbol{w}, \boldsymbol{e_s}) + A_{s_f}(\boldsymbol{\lambda_f}, \boldsymbol{e_s}) = 0. \tag{5.69}$$

Equation defining the solid displacement velocity

We define $\boldsymbol{v_s} \in \mathcal{U}_s$. We multiply the equation defining the solid displacement velocity by $\boldsymbol{v_s}$ and integrate over the solid domain

$$i\omega \int_{\Omega_s} \boldsymbol{w} \cdot \boldsymbol{v_s} dV - \int_{\Omega_s} \boldsymbol{u_s} \cdot \boldsymbol{v_s} dV = 0. \tag{5.70}$$

We define the following bi-linear operators

$$B_{s_1}(\boldsymbol{w}, \boldsymbol{v_s}) = \int_{\Omega_s} \boldsymbol{w} \cdot \boldsymbol{v_s} dV, \tag{5.71}$$

$$B_{s_2}(\boldsymbol{u_s}, \boldsymbol{v_s}) = \int_{\Omega_s} \boldsymbol{u_s} \cdot \boldsymbol{v_s} dV. \tag{5.72}$$

Equation 5.70 is now simplified as

$$i\omega\, B_{s_1}(\boldsymbol{w}, \boldsymbol{v_s}) - B_{s_2}(\boldsymbol{u_s}, \boldsymbol{v_s}) = 0. \tag{5.73}$$

Kinematic boundary condition equation

We define $\boldsymbol{\gamma_f} \in \mathcal{L}_f$. We multiply the kinematic boundary equation by $\boldsymbol{\gamma_f}$ and integrate over the fluid-structure interface

$$\int_{\Gamma_{fs}} \boldsymbol{u_f} \cdot \boldsymbol{\gamma_f} dS = \int_{\Gamma_{fs}} i\omega\, \boldsymbol{w} \cdot \boldsymbol{\gamma_f} + U \frac{\partial \boldsymbol{w}}{\partial x} \cdot \boldsymbol{\gamma_f} dS, \tag{5.74}$$

$$i\omega \int_{\Gamma_{fs}} \boldsymbol{w} \cdot \boldsymbol{\gamma_f} dS + \int_{\Gamma_{fs}} U \frac{\partial \boldsymbol{w}}{\partial x} \cdot \boldsymbol{\gamma_f} dS - \int_{\Gamma_{fs}} \boldsymbol{u_f} \cdot \boldsymbol{\gamma_f} dS = 0. \tag{5.75}$$

We define the following bi-linear operators

$$K_{fs_1}(\boldsymbol{w}, \boldsymbol{\gamma_f}) = \int_{\Gamma_{fs}} \boldsymbol{w} \cdot \boldsymbol{\gamma_f} dS, \tag{5.76}$$

$$K_{fs_2}(\boldsymbol{w}, \boldsymbol{\gamma_f}) = \int_{\Gamma_{fs}} U \frac{\partial \boldsymbol{w}}{\partial x} \cdot \boldsymbol{\gamma_f} dS, \tag{5.77}$$

$$K_{fs_3}(\boldsymbol{u_f}, \boldsymbol{\gamma_f}) = \int_{\Gamma_{fs}} \boldsymbol{u_f} \cdot \boldsymbol{\gamma_f} dS. \tag{5.78}$$

Equation 5.74 is now simplified as

$$i\omega\, K_{fs_1}(\boldsymbol{w}, \boldsymbol{\gamma_f}) + K_{fs_2}(\boldsymbol{w}, \boldsymbol{\gamma_f}) - K_{fs_3}(\boldsymbol{u_f}, \boldsymbol{\gamma_f}) = 0. \tag{5.79}$$

The weak formulation of Problem 5.42 is

$$\begin{cases} i\omega\, A_{f_1}(\boldsymbol{u_f}, \boldsymbol{v_f}) + A_{f_2}(\boldsymbol{u_f}, \boldsymbol{v_f}) - A_{f_3}(p, \boldsymbol{v_f}) - A_{f_4}(\boldsymbol{\lambda_f}, \boldsymbol{v_f}) = 0 \\ \\ A_{fc}(\boldsymbol{u_f}, q) = 0 \\ \\ i\omega\, A_{s_1}(\boldsymbol{u_s}, \boldsymbol{e_s}) + A_{s_2}(\boldsymbol{w}, \boldsymbol{e_s}) + A_{s_f}(\boldsymbol{\lambda_f}, \boldsymbol{e_s}) = 0 \\ \\ i\omega\, B_{s_1}(\boldsymbol{w}, \boldsymbol{v_s}) - B_{s_2}(\boldsymbol{u_s}, \boldsymbol{v_s}) = 0. \\ \\ i\omega\, K_{fs_1}(\boldsymbol{w}, \boldsymbol{\gamma_f}) + K_{fs_2}(\boldsymbol{w}, \boldsymbol{\gamma_f}) - K_{fs_3}(\boldsymbol{u_f}, \boldsymbol{\gamma_f}) = 0 \end{cases}, \tag{5.80}$$

5.1.7 Matrix formulation

Our method being a finite-element method, the discretization of the solid and fluid variables must be done. The bi-linear operators can then be expressed with their associated matrices. $\tilde{\boldsymbol{v_f}}$ is the discretized equivalent vector of the continuous variable $\boldsymbol{v_f}$ and $\tilde{\boldsymbol{u_f}}$ is the discretized equivalent vector of the continuous variable $\boldsymbol{u_f}$. The first bi-linear operator can be written as follows

$$A_{f_1}(\boldsymbol{u_f}, \boldsymbol{v_f}) = \tilde{\boldsymbol{v_f}}^T \mathcal{A}_{f_1} \tilde{\boldsymbol{u_f}}, \tag{5.81}$$

where $\mathcal{A}_{f_1}$ is the matrix of the bi-linear form A_{f_1}. The matrix formulation of Problem 5.80 is

$$\begin{bmatrix} \mathcal{A}_{f_2} & -\mathcal{A}_{f_3} & -\mathcal{A}_{f_4} & 0 & 0 \\ \mathcal{A}_{f_c} & 0 & 0 & 0 & 0 \\ -\mathcal{K}_{fs_3} & 0 & 0 & 0 & \mathcal{K}_{fs_2} \\ 0 & 0 & \mathcal{A}_{s_f} & 0 & \mathcal{A}_{s_2} \\ 0 & 0 & 0 & -\mathcal{B}_{s_2} & 0 \end{bmatrix} \begin{pmatrix} \tilde{\boldsymbol{u_f}} \\ \tilde{p} \\ \tilde{\boldsymbol{\lambda_f}} \\ \tilde{\boldsymbol{u_s}} \\ \tilde{\boldsymbol{w}} \end{pmatrix} + i\omega \begin{bmatrix} \mathcal{A}_{f_1} & 0 & 0 & 0 & 0 \\ 0 & 0 & 0 & 0 & 0 \\ 0 & 0 & 0 & 0 & \mathcal{K}_{fs_1} \\ 0 & 0 & 0 & \mathcal{A}_{s_1} & 0 \\ 0 & 0 & 0 & 0 & \mathcal{B}_{s_1} \end{bmatrix} \begin{pmatrix} \tilde{\boldsymbol{u_f}} \\ \tilde{p} \\ \tilde{\boldsymbol{\lambda_f}} \\ \tilde{\boldsymbol{u_s}} \\ \tilde{\boldsymbol{w}} \end{pmatrix} = 0 \tag{5.82}$$

The Problem obtained is an eigenvalue problem under the form

$$AX = \omega BX \tag{5.83}$$

The resolution of this eigenvalue problem will allow us to extract both the complex eigenvalue ω, which real part correspond to the natural angular frequency and which imaginary part correspond to the flow-added damping, and the eigenvector X.

5.2 Implementation details

5.2.1 Test case description

To verify our method, we aim to replicate Guo and Païdoussis (2000)'s study on the stability of a plate in two-dimensional channel flow. Our test case extends this study by incorporating a plate of finite thickness and using a two-dimensional domain for greater generalizability. Using a one-dimensional domain could be possible here because the system is similar to a beam, but it will not be applicable to more complex geometries such as hydrofoils or hydraulic turbine. This is one important difference with Guo and Païdoussis (2000) who use the beam equation for the solid domain.

We consider a beam of length L, finite thickness h_p, Young modulus E and Poisson ratio ν_s and density ρ_s. The fluid channel is of height $2h$, the fluid density is ρ_f, the base flow velocity is U and the fluid viscosity is η. Figure 5.1 shows the geometry of the test case with Ω_f the fluid domain, Ω_s the solid domain, $\Gamma_{fs} = \Gamma_1 + \Gamma_2 + \Gamma_3$ the fluid-structure interface, Γ_i the inlet, Γ_o the outlet and Γ_w the channel walls.

The bending stiffness D is defined as

$$D = \frac{Eh_p^3}{12(1-\nu_s^2)}. \tag{5.84}$$

To ease result interpretation and comparisons with Guo and Païdoussis (2000), we define the following non-dimensional numbers : the Reynolds number Re, the reduced velocity U_R, the mass ratio μ and the height-to-length ratio c defined as

$$Re = \frac{\rho_f U L}{\eta}, \quad U_R = L\sqrt{\frac{\rho_s h_p}{D}}U, \quad \mu = \frac{\rho_f L}{\rho_s h_p}, \quad c = \frac{h}{L}. \tag{5.85}$$

The results of the method are the complex dimensional eigenvalues ω that can be compared

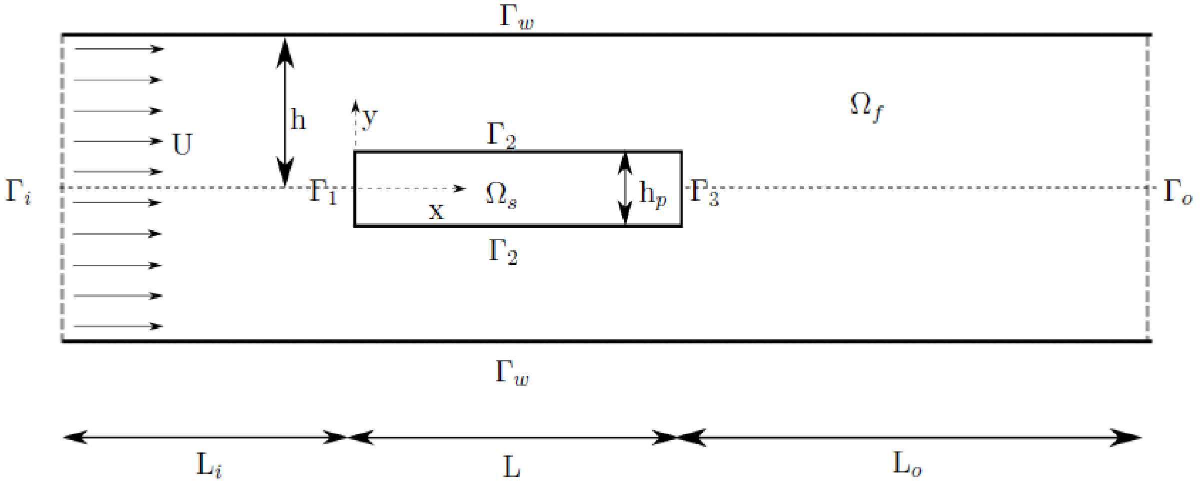

Figure 5.1 Schematic representation of the plate in axial flow defining the fluid and solid domains and geometrical parameters of the problem, from Couture (2020).

with the dimensionless eigenvalues $\bar{\omega}$ defined as

$$\bar{\omega} = L^2\sqrt{\frac{\rho_s h_p}{D}}\omega. \tag{5.86}$$

We consider two types of boundary conditions, the clamped-clamped case and the clamped-free case. We can vary the reduced velocity either by varying the Young's modulus E or the mean flow velocity U, to keep the other two dimensionless numbers constant. We chose to vary only E, to keep the Reynolds number constant.

As mentioned in Chapter 2, a major advantage of a viscous method compared to an insviscid or potential method, is that it can capture vorticity in the flow field, and especially in the wake. It is expected to find vortices in the wake of such system. Those vortices can be visualize by either plotting the streamlines of the flow or by plotting directly the vorticity. The vorticity V_z against the third dimension is interesting in our 2D case. It is defined as

$$V_z = \frac{\partial u_{fy}}{\partial x} - \frac{\partial u_{fx}}{\partial y}. \tag{5.87}$$

The boundary conditions for the fluid-structure interface have already been detailed in the previous section. A no-slip boundary condition is applied on the upper and lower walls. Similarly to Couture (2020), we apply a a stress-free boundary condition on outlet and a Dirichlet condition at the inlet (null perturbation).

5.2.2 Numerical tools used

In order to solve our problem, we use a similar procedure and code to those used by Couture (2020). The matrices are obtained using the finite-element solver FreeFEM++ (Hecht, 2012), and the eigenvalue problem is then solved using Matlab and its *eigs* function. FreeFEM++ is a 2D and 3D partial differential equations solver which is compatible with open-source mesh generator like Gmsh (Geuzaine and Remacle, 2009).

We use quadratic elements of FreeFem++ for the solid displacement, solid velocity and fluid velocity. We use the linear elements for the pressure and the boundary fluid stress.

5.2.3 Mesh information and convergence analysis

For this test case, we wanted to be able to control the density of the mesh around the plate and in the wake. This can easily be done with Gmsh. We create a structured mesh for the fluid and the solid domain. A convergence analysis is then performed to determine which mesh density is high enough to ensure converged results. To perform the convergence analysis, we chose a reduced velocity $U_R = 1$, a mass ratio $\mu = 1$ and a length-to-height ratio $c = 1$. Those values are typical values that we will use for the reproduction of the Guo and Païdoussis (2000) 's results. We use the highest value of Reynolds number $Re = 10^4$ to be used later. Indeed, a mesh that is converged for a high Reynolds number will also remain converged for a lower Reynolds number.

In order to show the convergence of our results, we follow the procedure described by Celik et al. (2008) using the Richardson extrapolation method. First, a convergence analysis was performed on the solid elements, by computing the second natural frequency without taking into consideration the surrounding fluid. We compute the extrapolated reference value, and we calculate the error as the relative difference between the natural frequency of the second mode for a given mesh and this reference value $e = |f - f_{ref}|/f_{ref}$, as shown in Figure 5.2 a.

The relative error is less than 0.1 % with a solid element size of 6 mm, knowing that the length of the plate is 1 m.

We then perform the same procedure while taking into consideration the fluid influence. In that case, the real and imaginary part of the obtained eigenvalue for the second mode are of interest. Therefore, the error is now defined as follow

$$e = \frac{\sqrt{(Re(\omega) - Re(\omega_{ref}))^2 + (Im(\omega) - Im(\omega_{ref}))^2}}{\sqrt{Re(\omega_{ref})^2 + Im(\omega_{ref})^2}},$$

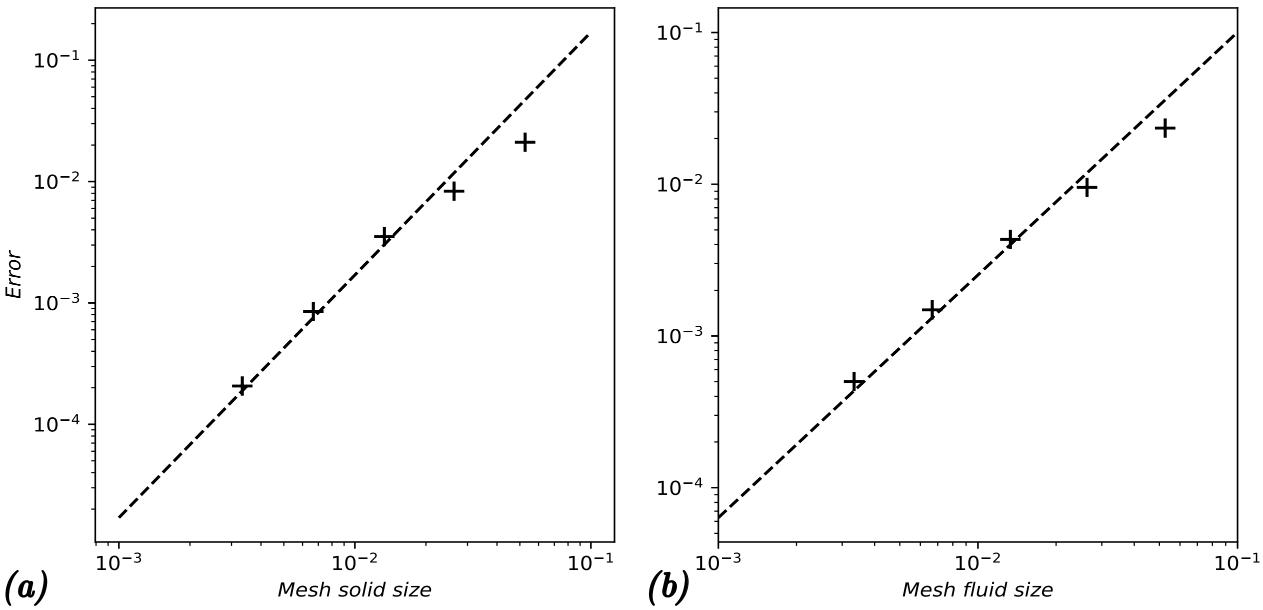

Figure 5.2 Convergence analysis: a) convergence analysis of the second natural frequency for the solid elements; b) convergence analysis of the second natural frequency the fluid elements.

with ω_{ref} the extrapolated reference value.

Figure 5.2 b shows the error as a function of the typical size of the mesh. The relative error is about 0.2 % for a mesh fluid size of 6 mm. We choose the mesh corresponding to this fluid element size for the following analyses.

5.3 Results

In this section, the method developed in this chapter will now be referred as the "hybrid model" for readability.

5.3.1 Argand diagram

Once the matrices are extracted from FreeFEM++, the eigenvalue problem is solved using the function *eigs* from Matlab. This allows us to extract a certain number of eigenvalues and eigenvectors. We can choose how many eigenvalues we want to extract as well as around which value we want the function to find the eigenvalues. This functionality is very useful to track an eigenvalue when slightly modifying a parameter.

For example, for $U_R = 1$, $\mu = 1$, $c = 1$ and $\eta = 1$, Figure 5.3 represent the Argand diagram of the obtained eigenvalues. The horizontal axis is the real part of the eigenvalue and the vertical axis is the imaginary part. Therefore, if the dot representing an eigenvalue is below the horizontal axis in the gray dashed line, its imaginary part is negative: this mode is unstable. Whereas all the modes above the horizontal axis are stable. Modes on the vertical axis, in the gray dashed line, have a null frequency.

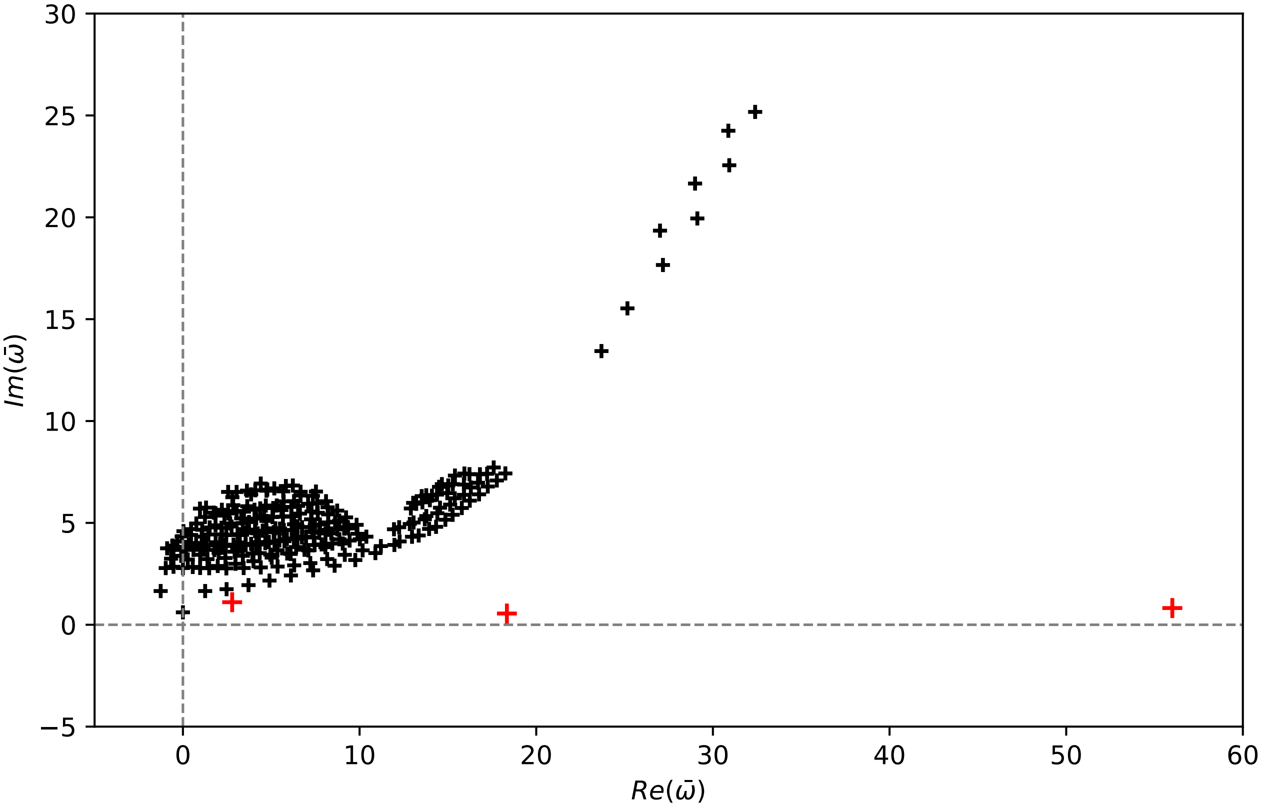

Figure 5.3 Argand diagram for $U_R = 1$, $\mu = 1$, $c = 1$ and $\eta = 1$. The spurious modes are represented in black while the coupled modes are in red.

On Figure 5.3, we can see that identifying the coupled modes is not trivial. Contrarily to other methods, the results show many spurious modes, that can correspond to hydrodynamic modes. In those cases, the fluid components are not taking into account the structure's motion, like described by Couture (2020). We can see that for this case, the coupled mode in red are separated from the spurious ones in black, having a much lower imaginary part. The hydrodynamic modes are in general very damped and stable. Nevertheless, it was observed that the smaller the viscosity, the closer the coupled modes are from the spurious modes, making the distinction more difficult. In order, to select accurately which eigenvalue correspond to a coupled mode, we can either use a tracking algorithm or visualize the mode shapes. In most cases, we only had to use the tracking algorithm. This technique consists in extracting the results for a small fluid density. Those eigenvalues are then very close to the theoretical natural frequency of a plate in vacuum. Then, we increase incrementally the density of the fluid to reach the desired mass number. From then, we know which eigenvalue corresponds to a fluid-structure coupled mode and which one corresponds to a spurious mode for a given reduced velocity. Afterwards, the evolution of the eigenvalues as a function of the reduced velocity can be evaluated by using this tracking algorithm while modifying step by step the reduced velocity. This procedure could also be done for any other parameter that we want to vary.

5.3.2 Evolution of the eigenvalues and eigenvectors with the reduced velocity

Clamped-free case

We want to see what happen to modes as U_R is increased. We analyze the behavior of the structure for different reduced velocities. At $U_R = 1$, the shape of the structure over one oscillation period for the second and third coupled mode is plotted on Figure 5.4. Because the reduced velocity is low, the shape of the modes are close to the mode shapes in vacuum. We observe one and two nodes respectively for these two coupled modes. We then plot the mode shapes of the structure for the second and third coupled mode at $U_R = 6$ and $U_R = 14$ on Figure 5.4. As we increase the reduced velocity (or decrease the rigidity of the structure), the mode shapes start to resemble those in vacuum less and less. The influence of the fluid becomes more important. At a certain point, the two mode shapes no longer have any nodes. The similarity between the mode shapes of the second and third mode begins to increase, to the point where it is difficult to determine which one corresponds to the second or third mode, without tracking them. Figure 5.4 also presents the evolution of the real part and imaginary part of the dimensionless eigenvalues of the second and third mode, for a viscosity $\eta = 0.01$, a mass ratio $\mu = 1$ and a length-to-height ratio $c = 1$.

For the second mode, the real part initially decreases with increasing reduced velocity, but then exhibits an upward trend. The imaginary part first increases and then becomes negative around $U_R = 5$, indicating a shift towards negative damping and a loss of stability. This signifies a single mode flutter instability, where the frequency is non-null. As for the third mode, its frequency decreases with rising reduced velocity, to reach the real part of the second mode, without coalescing. The imaginary part is initially close to zero but positive and increases slowly with the reduced velocity. However, around $U_R = 13$, it undergoes a significant increase. The designation of the second and third modes is arbitrary. Indeed, beyond $U_R = 14$, the frequency of the third mode falls below the one of the second, but we maintain continuity in their naming convention.

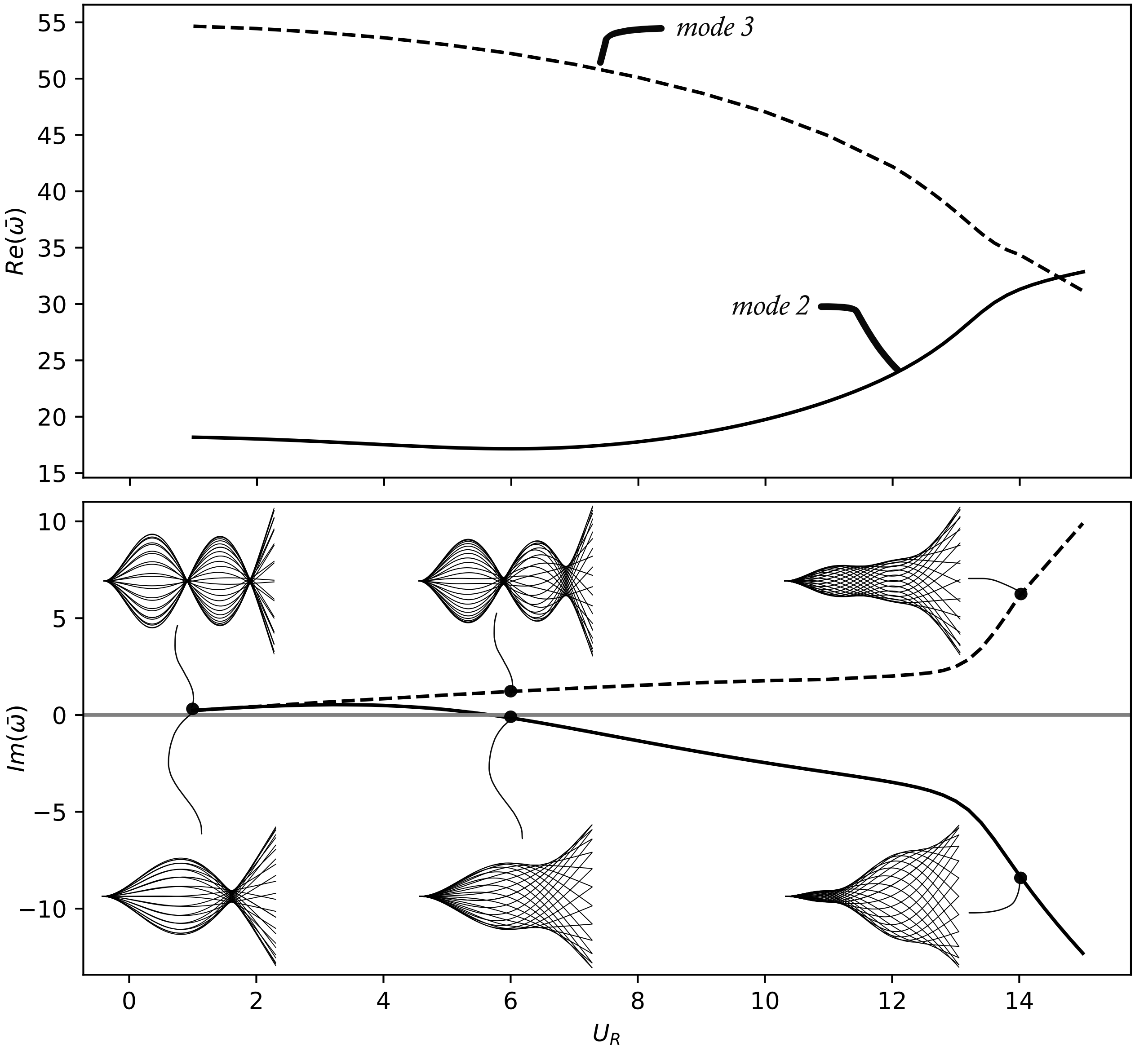

Figure 5.4 Evolution of the real part and imaginary part of the dimensionless eigenvalue of the second and third mode, for a viscosity $\eta = 0.01$, a mass ratio $\mu = 1$ and a length-to-height ratio $c = 1$, for the clamped-free case. The mode shapes of the structure are also shown for $U_R = 1$, $U_R = 6$ and $U_R = 14$. The results are compared with those of Guo and Païdoussis (2000).

When we compare those results with the results of Howell et al. (2009) in red lines on Figure 5.5, we can see a good agreement. Both models predict that the plate becomes unstable via a single mode flutter, with a critical reduced velocity of $U_R = 5$. The evolution of the frequency for the second mode with respect to the reduced velocity is similar.

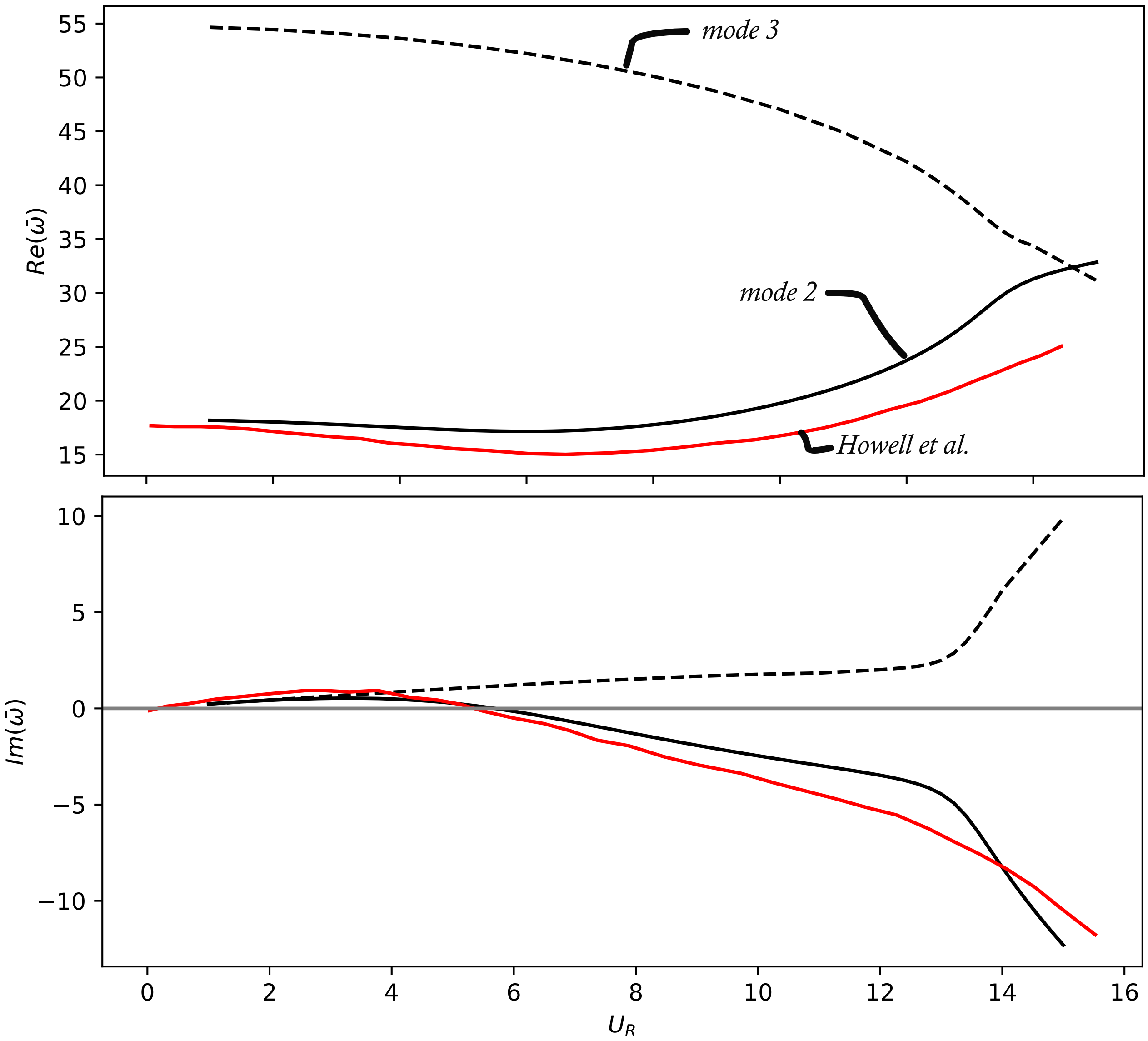

Figure 5.5 Evolution of the real part and imaginary part of the dimensionless eigenvalue of the second and third mode, for a viscosity $\eta = 0.01$, a mass ratio $\mu = 1$ and a length-to-height ratio $c = 1$, for the clamped-free case. The results are compared with those of Howell et al. (2009).

We also compare those results with the results of Guo and Païdoussis (2000) in red lines on Figure 5.6. Both models predict that the plate becomes unstable via a single mode flutter, with a critical reduced velocity of $U_R = 5$. The evolution of the frequency for the second mode with respect to the reduced velocity is similar. The only difference is that for high reduced velocity, the imaginary part of the second mode of Guo and Païdoussis (2000) is predicted by our third mode. This can be explained by the fact that for the values of reduced velocity corresponding to this part of the graph, the frequency of our third mode is actually getting smaller than the second mode. The difference in the way we define the mode number explains that difference. Furthermore, as seen in the previous section, the mode shapes of those two modes are similar around those reduced frequency. It can also be due to the fact that their model is inviscid.

We can also analyze the eigenvectors corresponding to the coupled mode obtained. Those eigenvectors will allow us to plot the fluid velocity displacement, the pressure field and the solid displacement, directly from the results. In this case, we consider plotting the vorticity around the structure and in the wake.

On Figure 5.7, we plot the vorticity distribution for three cases: a stable case at $U_R = 1$, one in the limit of stability at $U_R = 8$ and an unstable case at $U_R = 14$, for a viscosity $\eta = 1$. The vorticity is plotted positive in blue and negative in red. The horizontal axis is the x-direction and the vertical axis is the y-direction with the deformed plate in black. We plot both the real part and the imaginary part of the eigenvector. From Figure 5.7 a and b, we observe that there are several vortices of alternating sign in the wake predicted by the hybrid model for $U_R = 1$. At $U_R = 8$ and $U_R = 14$; on Figure 5.7 c, d, e and f, we observe vorticity at the trailing edge but also at the leading edge and around the plate. This is not observed for the most stable case. Those vortices are expected, and show that a viscous model is relevant to implicitly model the wake. In the case of inviscid flows like the potential flow theory, those vortices cannot be captured by the model and therefore the stability of the plate cannot be accurately predicted, except for methods which artificially apply a Kutta condition at the trailing edge of the plate. The eigenvectors plotted in Figure 5.7 oscillate with a certain frequency. They can be constructed for each time step of the period. The hybrid model extracts a complex eigenvector $\phi = \phi_R + i\phi_I$ and a complex eigenvalue $\omega = \omega_R + i\omega_I$. The mode is built for each time step t of the period with the real part of $\phi e^{i\omega t}$. We have without considering the damping term

$$Re(\phi e^{i\omega t}) = \phi_R cos(\omega_R t) - \phi_I sin(\omega_R t). \tag{5.88}$$

We can animate those eigenvectors over a period. These animations show that at $U_R = 1$ there is a stationary wave in the structure, as the mode shape is almost a beam mode with a standing wave. For the other two cases, we observe a traveling wave in the structure.

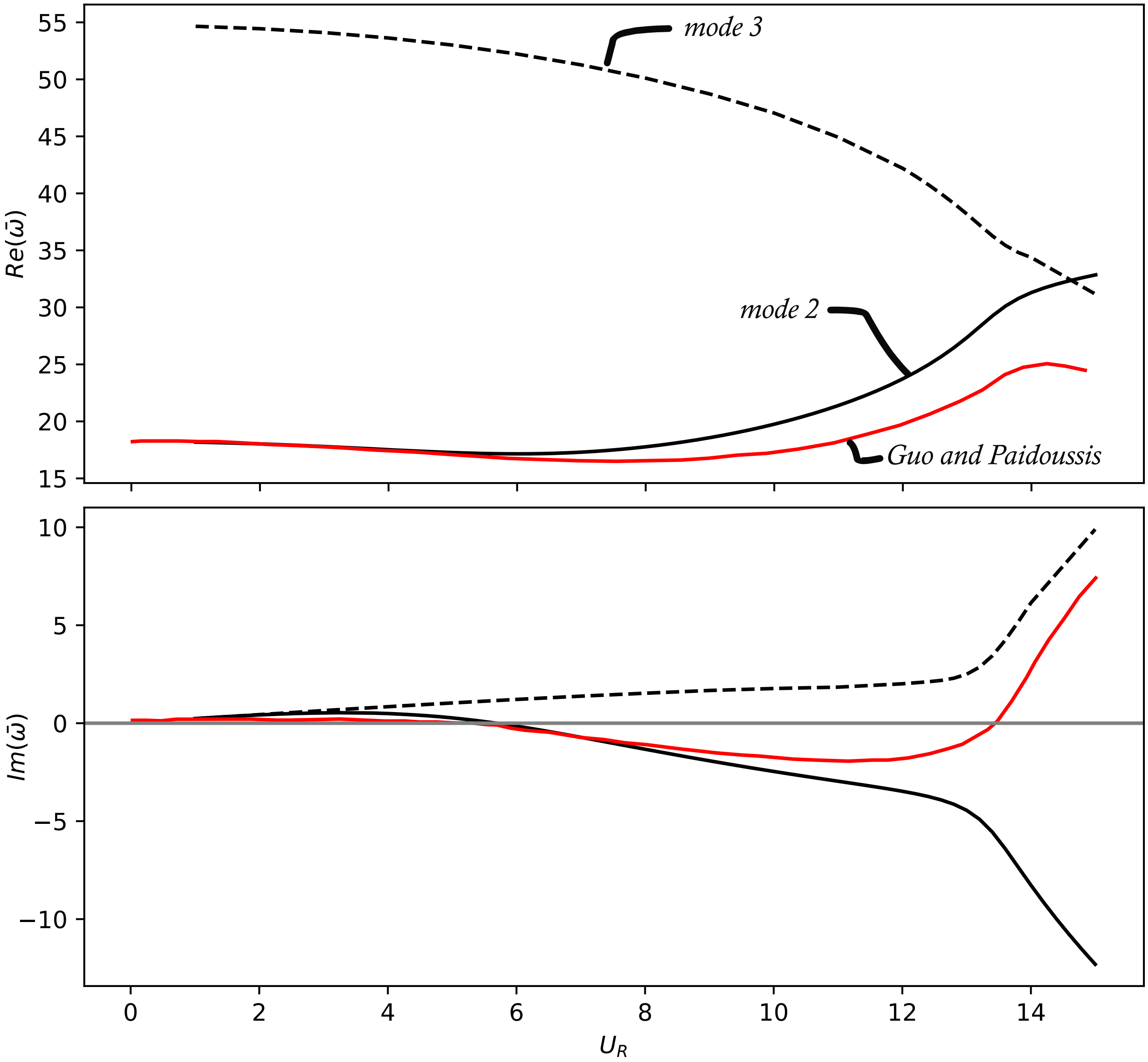

Figure 5.6 Evolution of the real part and imaginary part of the dimensionless eigenvalue of the second and third mode, for a viscosity $\eta = 0.01$, a mass ratio $\mu = 1$ and a length-to-height ratio $c = 1$, for the clamped-free case. The results are compared with those of Guo and Païdoussis (2000).

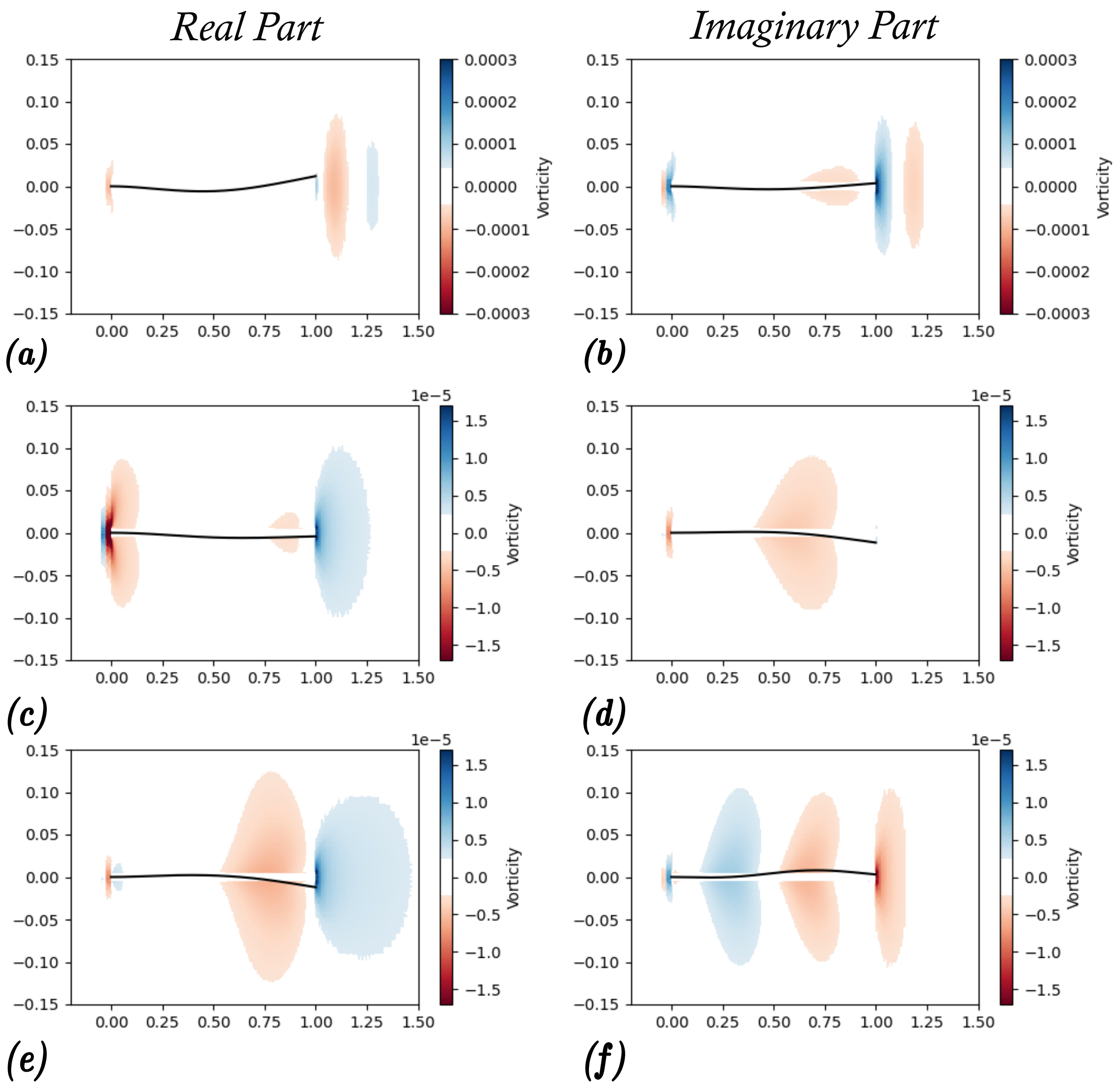

Figure 5.7 Real part and imaginary part of the vorticity distribution in the wake and around the plate of the second coupled mode for different values of reduced velocity with $\mu = 1$, $c = 1$ and $\eta = 1$: a) $U_R = 1$ real part, b) $U_R = 1$ imaginary part, c) $U_R = 8$ real part, d) $U_R = 8$ imaginary part, e) $U_R = 14$ real part, and f) $U_R = 14$ imaginary part.

The first coupled mode is less interesting to study because it remains stable for all conditions. We also had issues in tracking the right eigenvalues because the coupled modes and the spurious modes interacted together for a viscosity $\eta = 0.01$. We did not investigate it more because that mode is of less interest. Nevertheless, we predicted a good agreement for the imaginary part between Guo and Païdoussis (2000) and our results for the $\eta = 0.1$ case as shown in Figure 5.8. The main discrepancy concerns the real part. In our case, the frequency first increases with the reduced frequency before decreasing to become close to zero at $U_R = 14$. After $U_R = 14$, the frequency increases strongly with the reduced velocity. Guo and Païdoussis (2000) 's method predicted that the frequency of the first mode decreases to become null around $U_R = 7$. The damping is increasing linearly with the reduced velocity, suggesting that this mode becomes more and more stable as the reduced velocity increases. The damping trend predicted by our method is similar to the one obtained by Guo and Païdoussis (2000). However, we do not have the mode split, corresponding to the frequency becoming null that Guo and Païdoussis (2000) observed. The mode shapes of the structure are shown as well on Figure 5.8 for $U_R = 1$, $U_R = 6$ and $U_R = 14$. It is observed that the mode shape for the first mode is modified by the flow field only for high reduced frequencies, as it is very close to the mode shape in vacuum for $U_R = 1$ and $U_R = 6$.

Clamped-clamped case

For the clamped-clamped case, Figure 5.9 shows the evolution of the eigenvalues as a function of the reduced velocity and the comparison with the results of Guo and Païdoussis (2000) (in red). The mode shapes are also plotted for several reduced velocities.

The first mode is plotted with continuous and dashed lines and the second mode with dotted lines. For the first mode we plot two branches, one is valid for the small values of U_R with a non zero frequency, it is the oscillating branch. The second one has a zero frequency until $U_R = 17.5$, it is the divergence branch. For the oscillating branch, the real part is around 18 for small U_R and decreases progressively with the increase of U_R. The corresponding imaginary part is positive, therefore the mode corresponding to this branch is stable. The mode shapes are plotted for $U_R = 1$ and $U_R = 7.5$. For $U_R = 1$, the mode shape is very close to the one in vacuum. For $U_R = 7.5$, the mode shape is affected by the flow but it stays similar to the vacuum mode shape.

For the divergence branch, the real part remains zero until very high reduced velocity, indicating a static mode. The imaginary part initially increases with the reduced velocity, then splits into two sub-branches. One sub-branch continues to increase with the reduced velocity, while the other reaches a negative imaginary part around $U_R = 8$, suggesting a

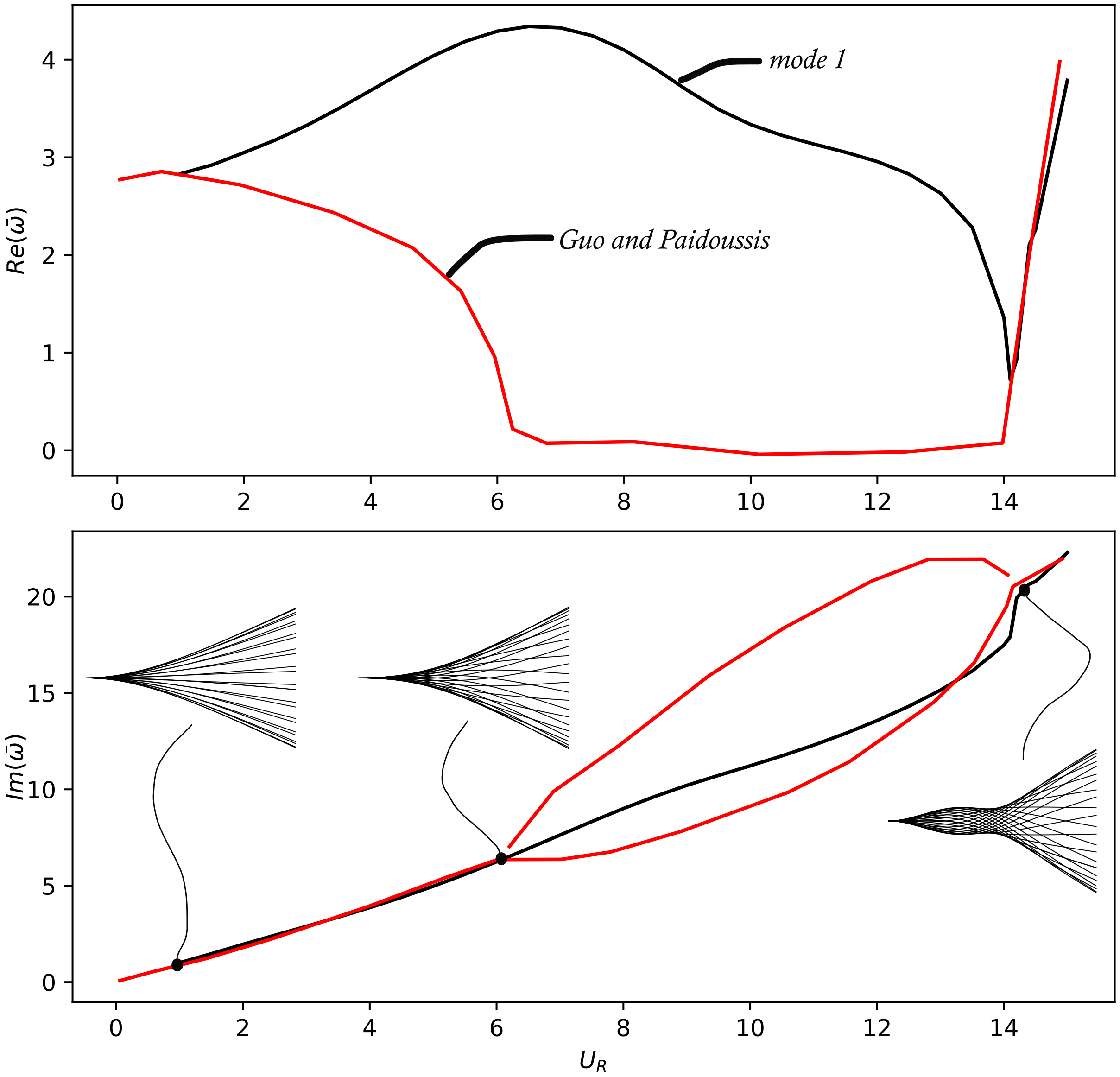

Figure 5.8 Evolution of the real part and imaginary part of the dimensionless eigenvalue of the first mode, for a viscosity $\eta = 0.1$, a mass ratio $\mu = 1$ and a length-to-height ratio $c = 1$, for the clamped-free case. The mode shapes of the structure are also shown for $U_R = 1$, $U_R = 6$ and $U_R = 14$. The results are compared with those of Guo and Païdoussis (2000).

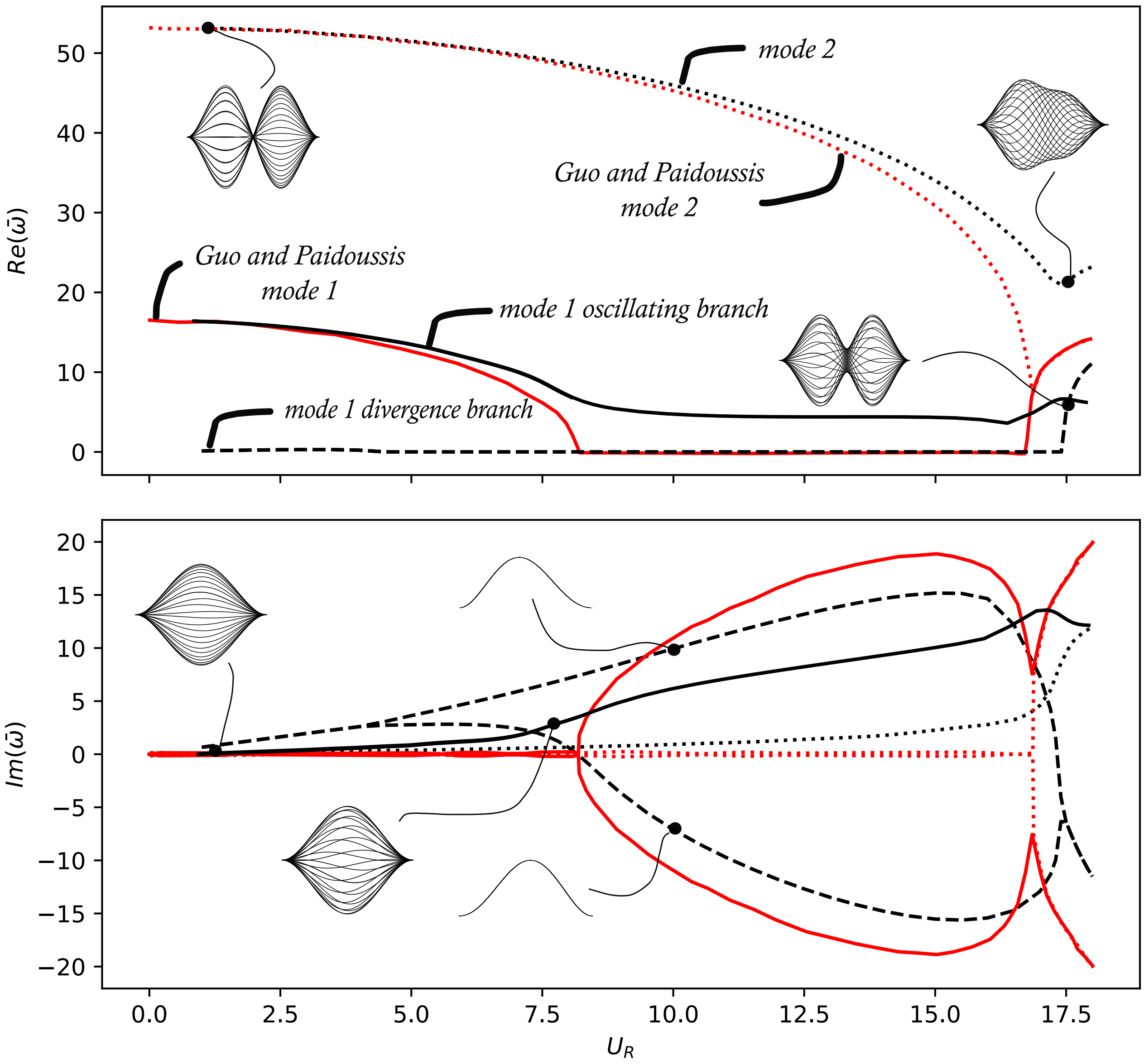

Figure 5.9 Evolution of the real part and imaginary part of the dimensionless eigenvalue of the first and second mode, for a viscosity $\eta = 0.01$, a mass ratio $\mu = 1$ and a length-to-height ratio $c = 1$, for the clamped-clamped case. The mode shapes of the structure are also shown for $U_R = 1$, $U_R = 7.5$, $U_R = 10$ and $U_R = 17.5$. The results are compared with those of Guo and Païdoussis (2000) in red.

loss of stability. This loss of stability occurs through static divergence, as evidenced by the zero frequency. Guo and Païdoussis (2000) also observed static divergence in this test case at the same critical reduced velocity. However, their ideal flow model exhibited only one continuous branch corresponding to the first mode. In contrast, the hybrid model, which incorporates viscous effects, introduces a discontinuity, resulting in two distinct branches. Therefore, we plot two separate branches to align with Guo and Païdoussis (2000)'s findings. Another notable difference is that in their model, the mode split occurs at zero damping for $U_R = 8$, whereas in the hybrid model, the split happens at non-zero damping due to viscosity. The mode shapes of the two sub-branches of the divergence branch at $U_R = 10$ are static, indicated by the zero frequency.

For the second mode, the frequency initially decreases with the reduced velocity until $U_R = 17.5$. Beyond this point, it increases as the reduced velocity continues to rise. The damping remains nearly constant and positive, close to zero, up to $U_R = 17.5$. The mode shape of the second mode at $U_R = 1$ resembles that of a second mode in a clamped-clamped vacuum scenario.

The system undergoes a coupled-mode flutter instability around $U_R = 17.5$ of the first and second mode. The imaginary part of the first mode is negative and decreases with the reduced velocity, while the frequency is not null anymore. This behavior was also observed by Guo and Païdoussis (2000) as shown in Figure 5.9. Nevertheless, their critical reduced velocity for the couple-mode flutter is slightly smaller with $U_R = 16.8$. The mode shape of the unstable and stable branch are shown for $U_R = 17.5$. We see that they look like a second mode which is altered by the flow field, as expected.

5.3.3 Effect of viscosity

We consider the influence of viscosity on the behavior of the system. Figure 5.10 presents the evolution of the dimensionless eigenvalues with the reduced velocity for different values of viscosity for the clamped-free case. For all tested values, the dimensionless frequencies of modes 2 and 3 start around 15 and 55 respectively for $U_R = 1$, and slowly converge together for increasing reduced velocity, without coalescing. The imaginary part of the second mode starts at 0 for $U_R \ll 1$ and increases linearly with U_R before becoming negative for a certain critical reduced velocity. Here, viscosity plays a direct role in the behavior of the system. The most viscous case ($\eta = 1$) has the highest damping and the highest critical reduced velocity of $U_R = 8$, it is the most stable mode. We also observe the existence of a threshold value of viscosity. Indeed, for the $\eta = 0.1$ case and the $\eta = 0.01$ case, the eigenvalues are similar for all the reduced velocity tested. The critical reduced velocity is around $U_R = 5$ for both cases.

For the third mode, the imaginary part increases linearly with the reduced velocity until $U_R = 13$ where the slope becomes much larger. We also observe a higher damping for the most viscous case. We have very close results for the $\eta = 0.1$ and $\eta = 0.01$ case, suggesting again the existence of a threshold value of viscosity.

In order to quantify the role of viscosity on damping, Table 5.1 shows the damping slope $\partial Im(\bar{\omega})/\partial U_R$ for low values of U_R, of the second and third mode, for different values of viscosity. The slope for the most viscous case is found to be the largest for both the second and third mode. The slope for the two other cases is similar.

Table 5.1 Slope $\partial Im(\bar{\omega})/\partial U_R$ for the second and third mode for different values of viscosity η.

Viscosity value	Mode 2	Mode 3
$\eta = 0.01$	0.15	0.16
$\eta = 0.1$	0.17	0.20
$\eta = 1$	0.35	0.43

For the clamped-clamped case, Couture (2020) predicted that the introduction of a viscous perturbation flow was not necessary, because the potential flow theory formulation could well predict the behavior of the structure. This is due to the fact that for the clamped-clamped case, the effect of circulation in the wake is not important. However, we saw that the hybrid model was also able to predict accurately the physics for this case. The value of the viscosity has a small influence on the evolution of the eigenvalues with the reduced velocity for the clamped-clamped case as shown in Figure 5.11, except for the small values of U_R.

Discussion

Viscosity acts as a damping term. We therefore expect the system to be more stable when the viscosity is increased, as observed on Figure 5.10. We also found that the slope of the damping with respect to the reduced velocity is much larger for the most viscous case, for the second and third mode. We expect to have more damping with a viscous method rather than an inviscid model. This was already observed in the previous section, where our results presented a higher damping than the results of Guo and Païdoussis (2000). Indeed, viscosity increase the dissipation of energy of the structure in the fluid. We show the existence of a threshold viscosity value, below which altering viscosity does not affect the system's behavior. At this threshold value, the Reynolds number is sufficiently high to emulate the inviscid scenario, while accurately integrating the circulation effect in the wake through our hybrid viscous implementation. The objective of the viscosity is to enhance the model's fidelity to physical

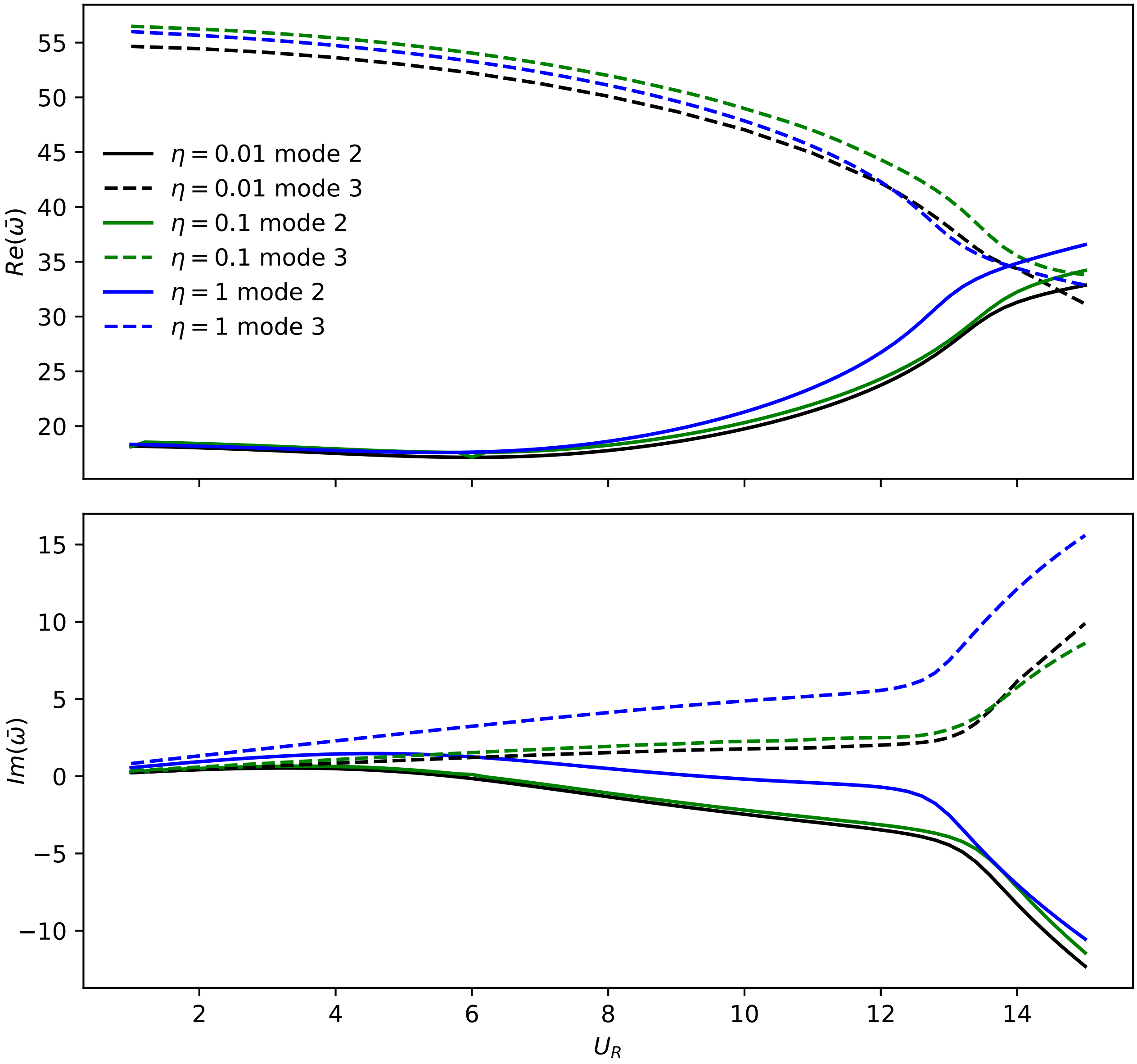

Figure 5.10 Evolution of the real part and imaginary part of the dimensionless eigenvalue of the first and second mode, for different values of viscosity, a mass ratio $\mu = 1$ and a length-to-height ratio $c = 1$, for the clamped-free case.

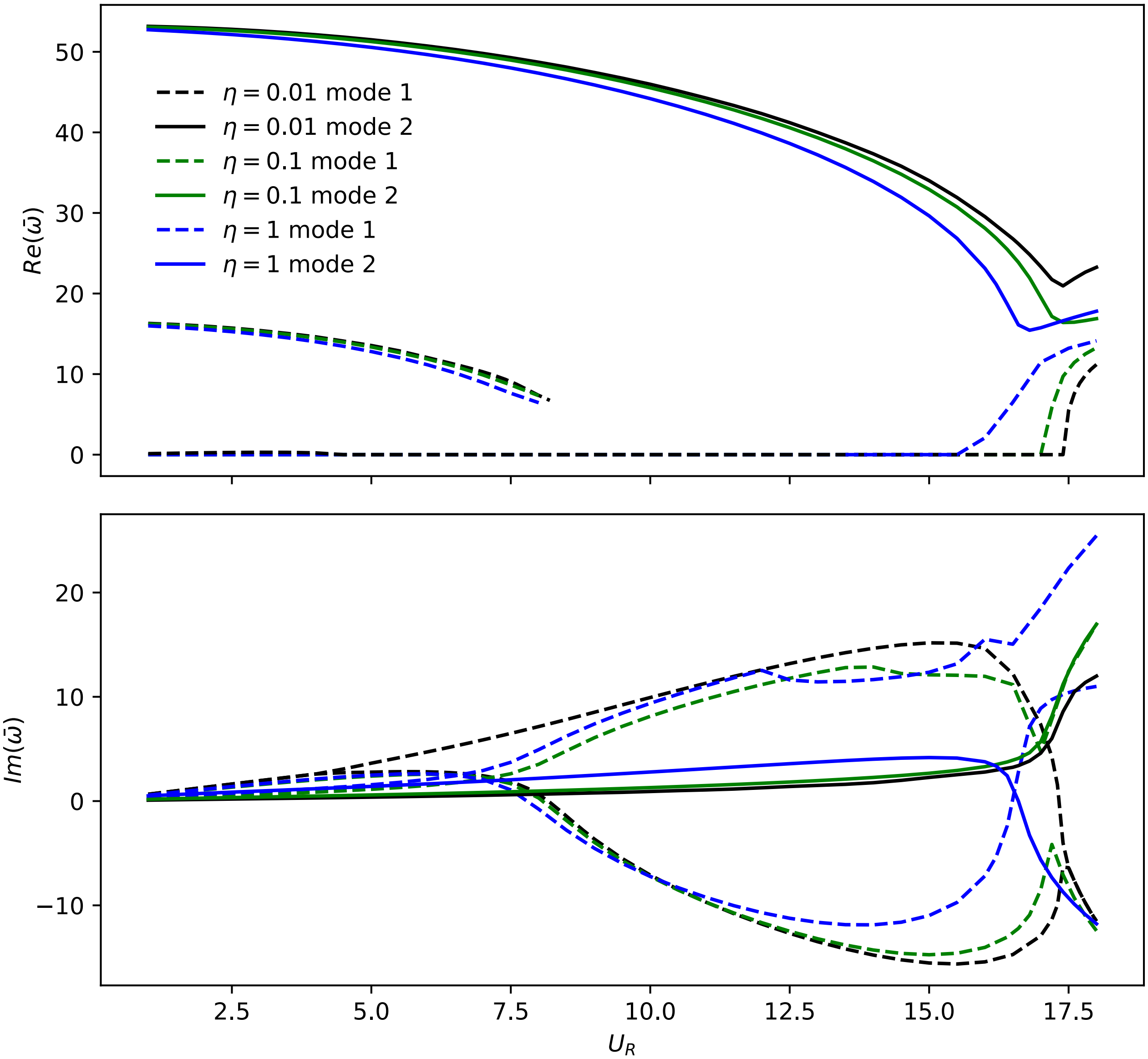

Figure 5.11 Evolution of the real part and imaginary part of the dimensionless eigenvalue of the first and second mode, for different values of viscosity, a mass ratio $\mu = 1$ and a length-to-height ratio $c = 1$, for the clamped-clamped case.

reality by implicitly capturing the circulation in the wake.

5.3.4 Stability maps

For both boundary condition cases, it is possible to plot stability maps. For the clamped-free case, the critical velocity of the single-mode flutter is determined as a function of the mass ratio μ. The stability is lost by single-mode flutter of the second mode for small mass ratio number, then by single-mode flutter of the third mode when μ increases and by single-mode flutter of the fourth mode for the highest mass ratios.

To compare our results with those of Guo and Païdoussis (2000), we plot $U_{cr}.\sqrt{\mu}$ as a function of $\mu/1+\mu$ on Figure 5.12 to create a stability map. We can see that $U_{cr}.\sqrt{\mu}$ increases with $\mu/1+\mu$. The curve presents several lobes due to the mode switch of the instability, starting with the second mode, to the third mode and finally the fourth one.

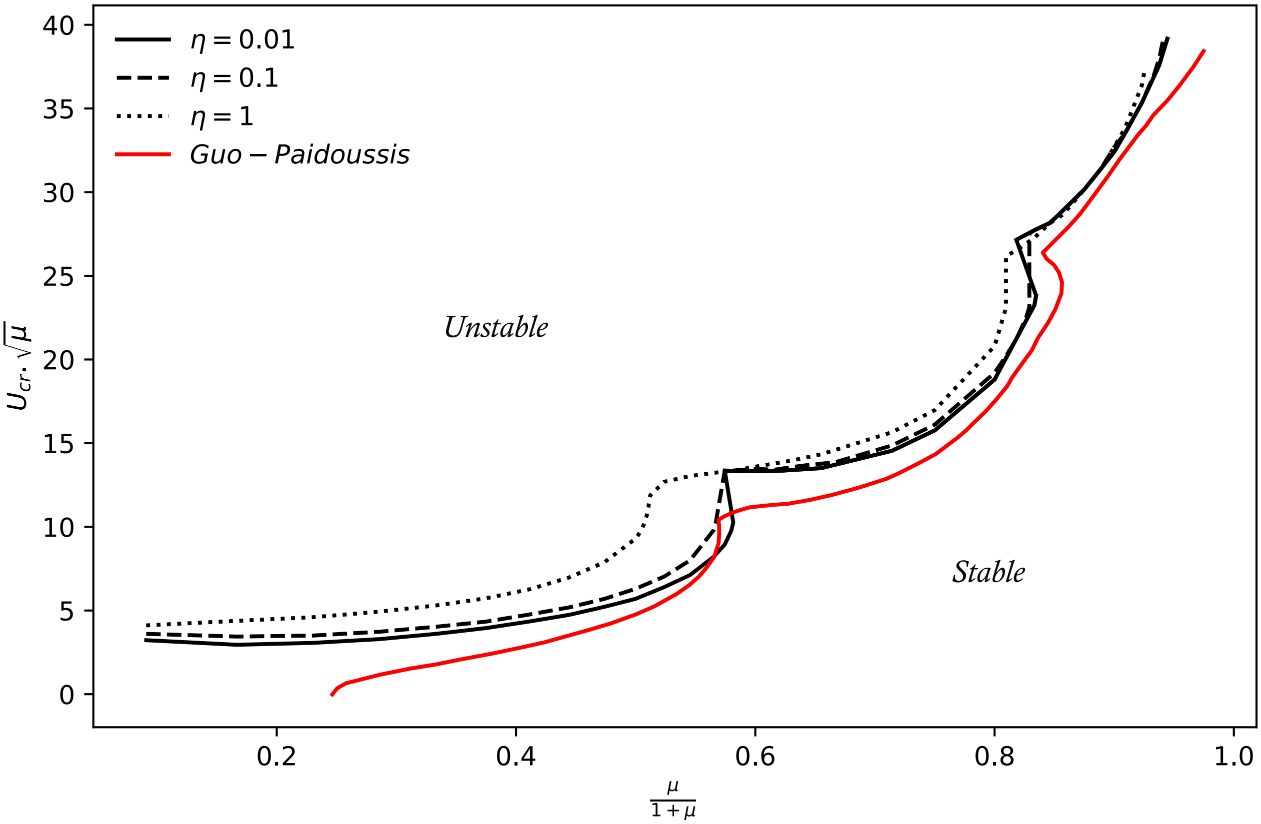

Figure 5.12 Stability map of the clamped-free case as a function of the mass ratio, for different values of viscosity, with a length-to-height ratio $c = 1$.

We observe a good match between the stability curves of Guo and Païdoussis (2000) and the $\eta = 0.01$ case, verifying our method. The major difference is for small mass ratio number where the critical velocity becomes null for Guo and Païdoussis (2000)'s model. They explained that this behavior is a limit of their inviscid flow model. To overcome that limitation, they suggest to artificially add a damping factor in the model, which is the case when viscosity is taken into account like in our model.

This stability curve can also be plotted for other values of viscosity. As predicted, if the viscosity is more important, the system is more stable and the critical velocities are higher, like shown on Figure 5.12, for the cases $\eta = 0.1$ and $\eta = 1$.

For the clamped-clamped case, we compute the critical velocity of the divergence for different mass numbers. We then plot the critical velocity as a function of $\sqrt{\mu}$ on Figure 5.13. We can see that there is a linear dependence between $U_c r$ and $\sqrt{\mu}$. This was also the observation of Guo and Païdoussis (2000).

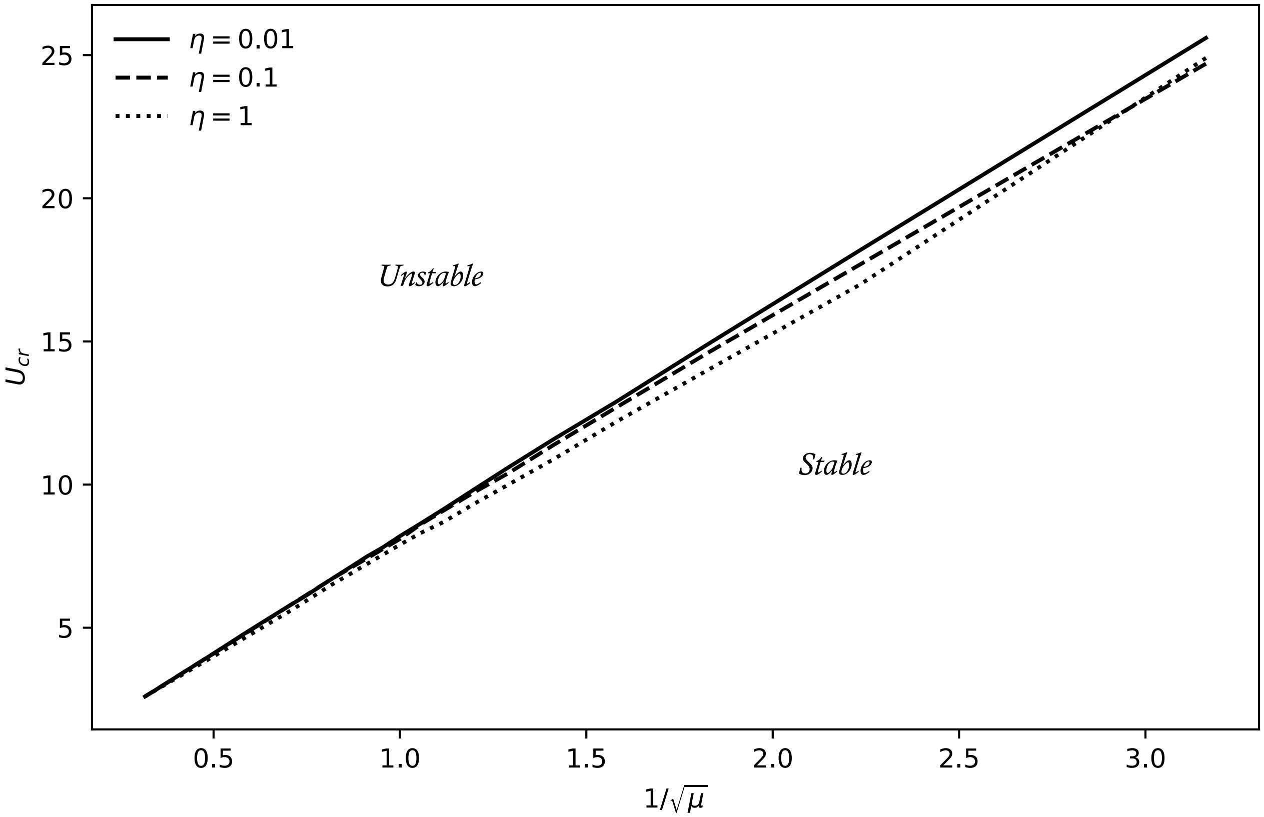

Figure 5.13 Stability map of the clamped-clamped case as a function of the mass ratio, for different values of viscosity, with a length-to-height ratio $c = 1$.

We also plot the critical velocity as a function of the length-to-height ratio c on Figure 5.14. We see that U_{cr} increases with c and then asymptotically converge towards to a constant. This is also what Guo and Païdoussis (2000) observed, as shown on Figure 5.13. This suggests that after a certain value of c, the effect of the walls are not significant of the dynamics of the plate. Whereas, when c is small, the confinement effect is predominant.

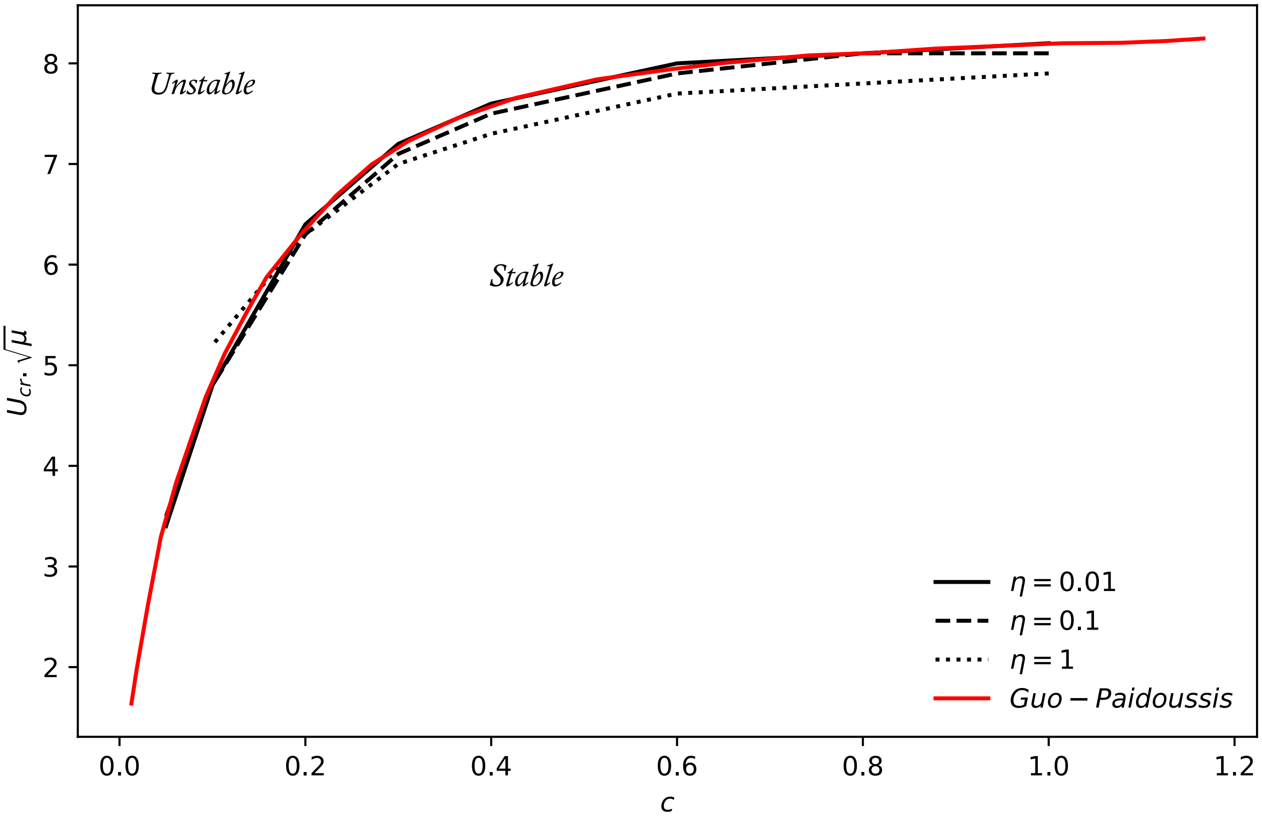

Figure 5.14 Stability map of the clamped-clamped case as a function of the length-to-height ratio, for different values of viscosity.

5.4 Extension of the method

We showed in the last section, that our hybrid method could predict accurately the frequency and the damping of a relatively simple geometry like a plate in a channel of axial flow. The critical velocity is also well predicted for different boundary conditions. Keeping in mind the ultimate objective of extending this method to a complex geometry, we can try out several improvements of the method.

Here, we will detail two improvements that we tried to implement in this thesis.

5.4.1 Potential base flow

We compare the results for the two different base flow presented in the methodology: the plug flow and the potential base flow respecting the no-penetration boundary condition at the fluid-structure interface. They happen to be very similar with less than 1% relative difference for the real part and imaginary parts of the obtained eigenvalues. Figure 5.15 shows a comparison for the second coupled mode with a clamped-free boundary condition. The black lines represent the results for the plug flow method and the purple lines the modified base flow respecting the no-penetration boundary conditions. The method developed here is therefore still valid with a realistic base flow, taking into account no-penetration around the structure.

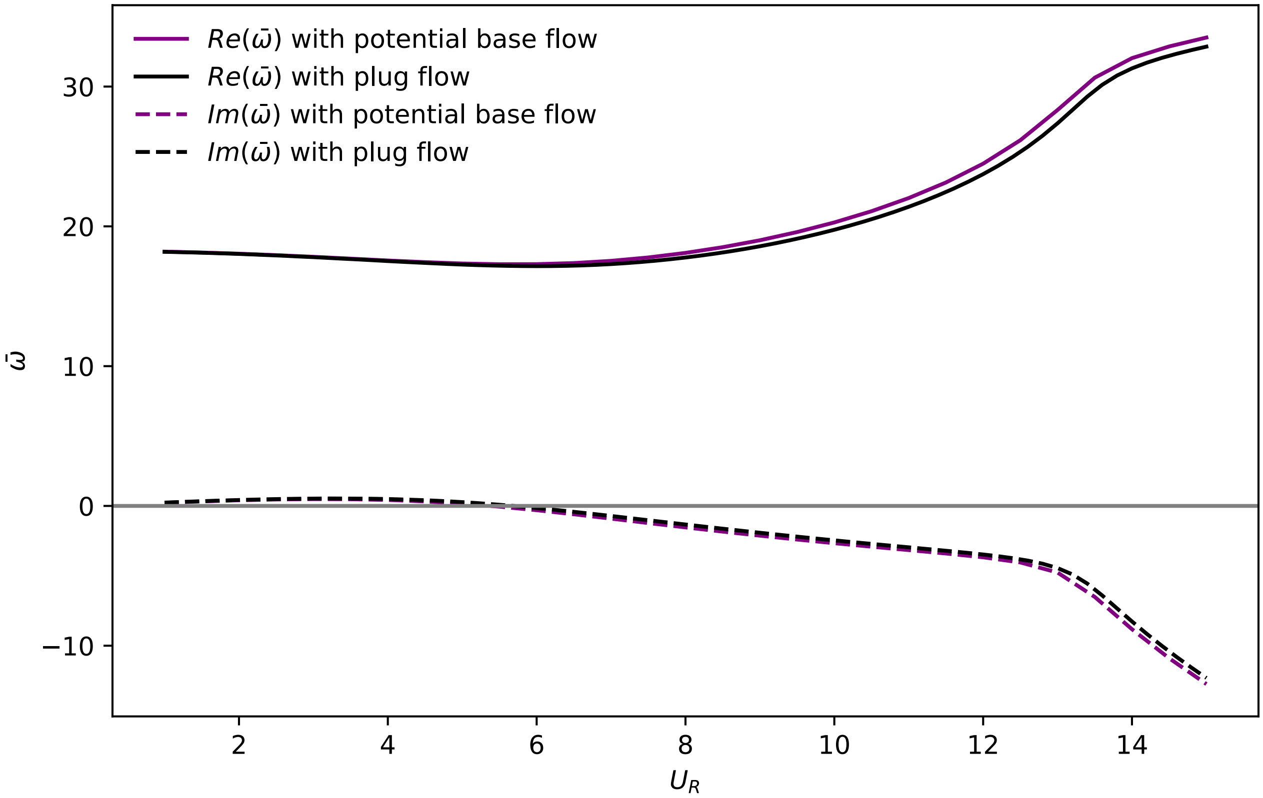

Figure 5.15 Comparison of the evolution of the real part and imaginary part of the eigenvalue for the second mode between the plug base flow method and the potential base flow method, with a mass ratio $\mu = 1$, a length-to-height ratio $c = 1$ and a viscosity $\eta = 0.01$.

5.4.2 3D test case

Another way to extend the method developed here is to apply it to a 3D case. Indeed, the equations are still valid in the 3D case while being slightly more difficult to implement. The goal is to study a 3D case previously studied with the first method of this chapter. We chose to study the F1 hydrofoil, and compare the results of the two methods. However, technical issues concerning the mesh definition in 3D prevented us from obtaining results yet. Therefore, this 3D test case is still under investigation.

CHAPTER 6 CONCLUSION

6.1 Summary of Works

We have shown in Chapter 4, that a panel method based on the potential flow theory could evaluate accurately the flow-added damping in the case of several single straight hydrofoils and a cascade of straight hydrofoils. Indeed, the aeroelastic flutter analysis method from NASTRAN was in agreement with other numerical and experimental results from the literature, the flow-added damping for different hydrofoil profiles, trailing edge shapes, boundary conditions and material properties. This method is a fast way to evaluate the flow-added damping on simple geometries. Turbine designers can use this approach when developing new vane designs that fall within the method's range of validity.

In Chapter 5, a finite element formulation is introduced as an alternative method for evaluating flow-added damping, applicable to more complex geometries. This approach solves the solid and fluid domains using the general equations of continuum mechanics. We consider the evolution of a small perturbation around a static base state. The particularity of the hybrid model is its flow field: the base flow is inviscid, while the perturbation flow is viscous. This strong assumption was verified for a cantilever plate subjected to axial flow. The hybrid model has been shown to accurately predict the stability of that system under various boundary conditions, with a computation time of several minutes. However, the verification was conducted using only one test case. To further substantiate the model, additional validation cases should be performed. Thanks to the viscous perturbation flow, we can study the vorticity in the wake and around the structure. This allows a deeper understanding of the influence of the fluid on the stability of the structure. The vortices shed in the wake cannot be modeled using inviscid flow methods, showing the importance of the hybrid model.

6.2 Limitations

However, the goal of this project is to be able to apply a fast method like this one to a very complex geometry such as a hydraulic turbine. For the first method, NASTRAN cannot capture confinement effects and non-uniform flows. We also found that complex geometries with cambered hydrofoils for example would not be modeled accurately by NASTRAN. Therefore, the panel method is only valid for simple geometries.

Concerning the finite-element method, although we developed the method to be able to use it on more complex geometries, it was only tested on a cantilever plate for now. Further studies will be needed in order to determine the validity on a wider range of designs. For the case of a clamped-free cantilever plate, the results were in good agreement in comparison with Howell et al. (2009)'s results, while it was verified only for small values of reduced velocity when comparing with the results of Guo and Païdoussis (2000). This discrepancy could be further explained in a future work.

6.3 Future Research

In this thesis, we presented methods that were verified only on relatively simple geometries. This work could then be further improved by validating them on more complex geometries, especially the hybrid model. It could be on a cascade of hydrofoils, a guide vane or a runner blade. The idea would be to take an existing CFD RANS result to account for the static base flow. Even though those CFD results will increase the computation time of the method, they are usually already performed by the turbine designers for other purposes than the flow-added damping determination. Therefore, they do not contribute fully to the computation time of the determination of the flow-added damping but rather the performance study of the design. Once the base flow is determined, the linear stability analysis as described in this thesis could be performed, and the flow-added damping could be extracted from the resulting complex eigenvalues.

It is important to determine whether the base flow can be considered inviscid. If so, the free-slip boundary condition at the fluid-structure interface will remain applicable, allowing the method to be used as developed here. However, if the base flow is viscous, the method will require adaptation. As discussed by Gosselin (2006), with a viscous base flow the kinematic boundary condition at the interface could be applied at a certain distance δ from the structure. This will result in a non-zero transverse velocity of the fluid. By doing so, we artificially recover the destabilizing term in the boundary condition at the interface. Indeed with a no-slip boundary condition, the kinematic boundary condition must be applied to the deformed position of the structure which would necessitate the use of moving meshes and nonlinear models and would considerably increase the computation time of the method. Therefore, applying the boundary condition at a chosen distance δ from the structure will ensure the method to stay computationally cheap. This would represent a new way for turbine designers to determine the flow-added damping of their devices and open the door for more innovation in the field of hydraulic turbine.

REFERENCES

Bergan, C. W. (2019). Dynamic loads on francis turbines: An experimental study.

Bergan, C. W., Tengs, E. O., Solemslie, B., and Dahlhaug, O. G. (2019a). An experimental investigation of the hydrodynamic damping of vibrating hydrofoils. *IOP Conference Series: Earth and Environmental Science*, 240.

Bergan, C. W., Tengs, E. O., Solemslie, B. W., Østby, P., and Dahlhaug, O. G. (2019b). Damping measurements on a multi-blade cascade with multiple degrees of freedom: A francis-99 test case. In *Journal of Physics: Conference Series*, volume 1296, page 012003. IOP Publishing.

Biskri, D. E. (2007). *Méthodes de calcul des forces aérodynamiques pour les études des interactions aéroservoélastiques.* PhD thesis, École de technologie supérieure, Montréal, Canada.

Celik, I. B., Ghia, U., Roache, P. J., and Freitas, C. J. (2008). Procedure for estimation and reporting of uncertainty due to discretization in cfd applications. *Journal of fluids Engineering-Transactions of the ASME*, 130(7).

Cisonni, J., Lucey, A. D., Elliott, N. S., and Heil, M. (2017). The stability of a flexible cantilever in viscous channel flow. *Journal of Sound and Vibration*, 396:186–202.

Coutu, A., Seeley, C., Monette, C., Nennemann, B., and Marmont, H. (2012). Damping measurements in flowing water. In *IOP Conference Series: Earth and Environmental Science*, volume 15, page 062060. IOP Publishing.

Couture, A. (2020). *Linear Stability Analysis of Fluid-Structure Problems Using Time-Linearized Coupled Formulations.* PhD thesis, Ecole Polytechnique, Montréal (Canada).

Cupr, P., Rudolf, P., and Habán, V., editors (2018). *Numerical Investigation of Added Mass and Damping Effects on a Hydrofoil in Cavitation Tunnel.*

Dehkharqani, A. S., Aidanpää, J.-O., Engström, F., and Cervantes, M. J. (2018). A review of available methods for the assessment of fluid added mass, damping, and stiffness with an emphasis on hydraulic turbines. *Applied Mechanics Reviews*, 70(5):050801.

Dowell, E. H. (1971). Generalized aerodynamic forces on a flexible plate undergoing transient motion in a shear flow with an application to panel flutter. *AIAA Journal*, 9(5):834–841.

Dowell, E. H. (1995). A modern course in aeroelasticity. *Netherlands, Springer.*

El Chebair, A., Misra, A., and Païdoussis, M. (1990). Theoretical study of the effect of unsteady viscous forces on inner-and annular-flow-induced instabilities of cylindrical shells. *Journal of Sound and Vibration*, 138(3):457–478.

Fernández, M. Á. and Le Tallec, P. (2003). Linear stability analysis in fluid–structure interaction with transpiration. part i: Formulation and mathematical analysis. *Computer Methods in Applied Mechanics and Engineering*, 192(43):4805–4835.

Fung, Y.-c. (1955). *An Introduction to the Theory of Aeroelasticity.* Wiley.

Gabbai, R. D. and Benaroya, H. (2005). An overview of modeling and experiments of vortex-induced vibration of circular cylinders. *Journal of Sound and Vibration*, 282(3-5):575–616.

Gauthier, J., Giroux, A., Etienne, S., and Gosselin, F. (2017). A numerical method for the determination of flow-induced damping in hydroelectric turbines. *Journal of Fluids and Structures*, 69:341–354.

Geuzaine, C. and Remacle, J.-F. (2009). Gmsh: A 3-d finite element mesh generator with built-in pre-and post-processing facilities. *International Journal for Numerical Methods in Engineering*, 79(11):1309–1331.

Gosselin, F. (2006). Stability of a rotating cylindrical shell containing axial viscous flow. *Masters thesis, McGill University, Montréal, Canada.*

Government of Canada, C. E. R. (2023). Cer - provincial and territorial energy profiles - quebec.

Guo, C. Q. and Païdoussis, M. P. (2000). Stability of rectangular plates with free side-edges in two-dimensional inviscid channel flow. *Journal of Applied Mechanics*, 67(1):171–176.

Hassig, H. J. (1971). An approximate true damping solution of the flutter equation by determinant iteration. *Journal of Aircraft*, 8(11):885–889.

Hecht, F. (2012). New development in freefem++. *Journal of Numerical Mathematics*, 20(3-4):251–265.

Howell, R., Lucey, A., Carpenter, P., and Pitman, M. (2009). Interaction between a cantilevered-free flexible plate and ideal flow. *Journal of Fluids and Structures*, 25(3):544–566.

Kammerer, A. and Abhari, R. S. (2009). Experimental study on impeller blade vibration during resonance—part ii: Blade damping.

Karlsson, M., Nilsson, H., Aidanpää, J.-O., et al. (2009). Numerical estimation of torsional dynamic coefficients of a hydraulic turbine. *International Journal of Rotating Machinery*, 2009.

Kumar, K. and Saini, R. (2022). Economic analysis of operation and maintenance costs of hydropower plants. *Sustainable Energy Technologies and Assessments*, 53:102704.

Kwak, M. and Kim, K. (1991). Axisymmetric vibration of circular plates in contact with fluid. *Journal of Sound and Vibration*, 146(3):381–389.

Lamoureux, D., Audefroy, C., Tazi Labzour, O., Houde, S., and Gosselin, F. P. (2023). Evaluating flow-added damping on a hydrofoil by combining vibro-acoustics and doublet-lattice panel analyses. *UNDER REVIEW.*

Liaghat, T., Guibault, F., Allenbach, L., and Nennemann, B. (2014). Two-way fluid-structure coupling in vibration and damping analysis of an oscillating hydrofoil. In *ASME International Mechanical Engineering Congress and Exposition*, volume 46476, page V04AT04A073. American Society of Mechanical Engineers.

Liang, Q., Rodriguez, C. G., Egusquiza, E., Escaler, X., Farhat, M., and Avellan, F. (2007). Numerical simulation of fluid added mass effect on a francis turbine runner. *Computers & Fluids*, 36(6):1106–1118.

Lighthill, M. (1958). On displacement thickness. *Journal of Fluid Mechanics*, 4(4):383–392.

Louyot, M., Nennemann, B., Monette, C., and Gosselin, F. P. (2020). Modal analysis of a spinning disk in a dense fluid as a model for high head hydraulic turbines. *Journal of Fluids and Structures*, 94:102965.

Monette, C., Nennemann, B., Seeley, C., Coutu, A., and Marmont, H. (2014). Hydro-dynamic damping theory in flowing water. In *IOP Conference Series: Earth and Environmental Science*, volume 22, page 032044. IOP Publishing.

Nicolle, J., Morissette, J.-F., and Giroux, A.-M. (2023). Towards a structural digital twin for a hydraulic runner using modal analysis.

Paidoussis, M. P. (1998). *Fluid-Structure Interactions: Slender Structures and Axial Flow*, volume 1. Academic Press.

Pastor, M., Binda, M., and Harþarik, T. (2012). Modal assurance criterion. *Procedia Engineering*, 48.

Pfister, J.-L., Marquet, O., and Carini, M. (2019). Linear stability analysis of strongly coupled fluid–structure problems with the arbitrary-lagrangian–eulerian method. *Computer Methods in Applied Mechanics and Engineering*, 355:663–689.

Pitra, G. M. and Musti, K. S. (2021). Duck curve with renewable energies and storage technologies. In *2021 13th International conference on computational intelligence and communication networks (CICN)*, pages 66–71. IEEE.

Roth, S., Calmon, M., Farhat, M., Münch, C., Bjoern, H., and Avellan, F. (2009). Hydrodynamic damping identification from an impulse response of a vibrating blade. In *Proceedings of the 3rd IAHR International Meeting of the Workgroup on Cavitation and Dynamic Problems in Hydraulic Machinery and Systems*, volume 1, pages 253–260. Brno University of Technology.

Seeley, C., Coutu, A., Monette, C., Nennemann, B., and Marmont, H. (2012). Characterization of hydrofoil damping due to fluid–structure interaction using piezocomposite actuators. *Smart Materials and Structures*, 21(3):035027.

Siemens (2014). Aeroelastic analysis user's guide.

Tazi Labzour, O. (2023). *Combination of PINNs and Reduced-Order Modeling to Predict Vortex-Induced Vibrations*. PhD thesis, Polytechnique Montréal, Montréal, Canada.

Tengs, E., Einzinger, J., and Storli, P.-T. (2019a). Two-way coupled simulation of the francis-99 hydrofoil using model order reduction. In *Journal of Physics: Conference Series*, volume 1296, page 012001. IOP Publishing.

Tengs, E. O., Bergan, C. W., Jakobsen, K.-R., and Storli, P. T. (2019b). Numerical simulation of the hydrodynamic damping of a vibrating hydrofoil. *IOP Conference Series: Earth and Environmental Science*, 240.

Theodorsen, T. (1949). General theory of aerodynamic instability and the mechanism of flutter. Technical report.

Trivedi, C. (2017). A review on fluid structure interaction in hydraulic turbines: A focus on hydrodynamic damping. *Engineering Failure Analysis*, 77:1–22.

Università degli Studi di Napoli Federico II, a. (2020). Example on airfoil flutter speed computation.

Zeng, Y., Wang, C., Huang, B., Wang, F., Xiao, R., and Yao, Z. (2023). A comprehensive empirical equation for the hydrodynamic damping of vibrating blade-like structures. *Ocean Engineering*, 270:113721.

Zeng, Y., Yao, Z., Yang, Z., Wang, F., and Hong, Y. (2018). The prediction of hydrodynamic damping characteristics of a hydrofoil with blunt trailing edge. In *IOP Conference Series: Earth and Environmental Science*, volume 163, page 012041. IOP Publishing.

Zeng, Y., Yao, Z., Zhou, P., Wang, F., and Hong, Y. (2019). Numerical investigation into the effect of the trailing edge shape on added mass and hydrodynamic damping for a hydrofoil. *Journal of Fluids and Structures*, 88:167–184.